ELECTRONIC STRUCTURE CALCULATIONS ON EXTENDED METAL ATOM CHAINS. INSIGHTS ON STRUCTURAL, MAGNETIC AND TRANSPORT PROPERTIES

Mariano Alejo Spivak

UNIVERSITAT ROVIRA i VIRGILI

Electronic structure calculations on Extended Metal Atom Chains. Insights on structural, magnetic and transport properties

MARIANO A. SPIVAK

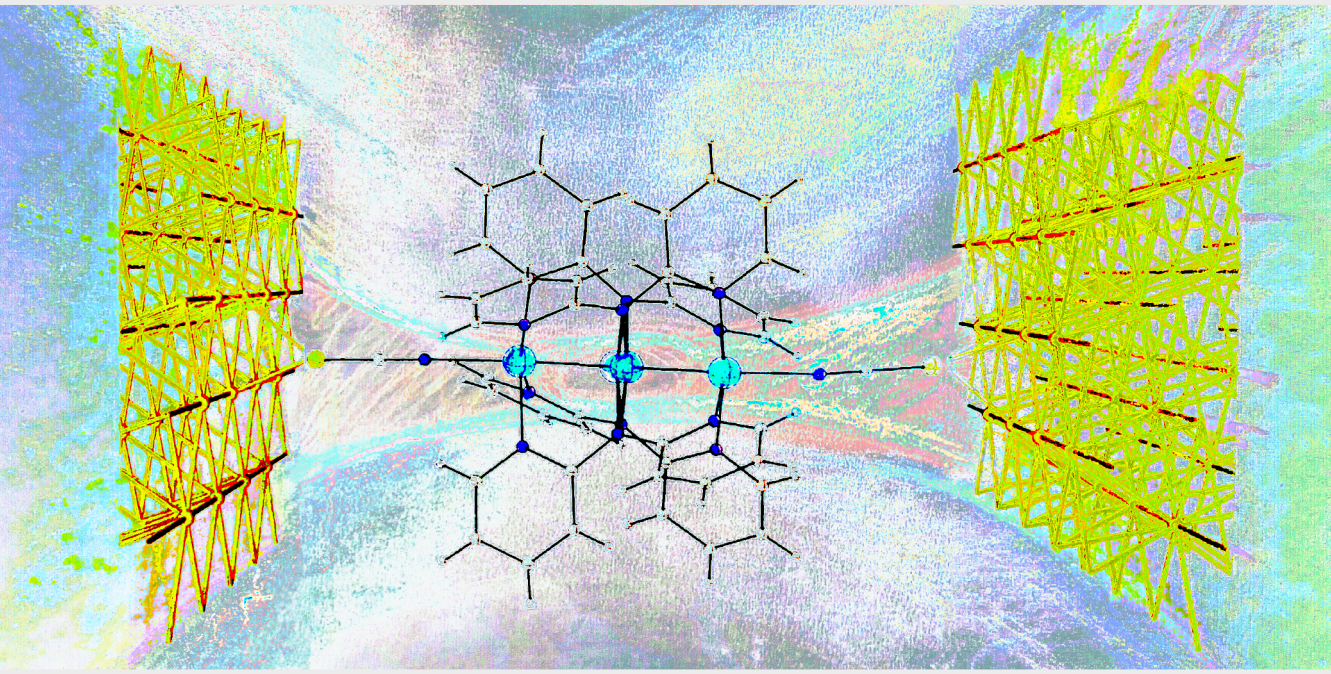

DOCTORAL THESIS

2017

DOCTORAL THESIS
MARIANO A. SPIVAK

Electronic structure calculations on Extended Metal Atom Chains. Insights on structural, magnetic and transport properties

2017

UNIVERSITAT ROVIRA I VIRGILI
ELECTRONIC STRUCTURE CALCULATIONS ON EXTENDED METAL ATOM CHAINS. INSIGHTS ON STRUCTURAL, MAGNETIC AND TRANSPORT PROPERTIES
Mariano Alejo Spivak

UNIVERSITAT
ROVIRA i VIRGILI

Mariano A. Spivak

Electronic structure calculations on Extended Metal Atom Chains. Insights on structural, magnetic and transport properties.

Doctoral Thesis

Supervised by Dr. Coen de Graaf and Dr. Xavier López

Department of Physical and Inorganic Chemistry
Quantum Chemistry Group

Universitat Rovira i Virgili

Tarragona
2017

UNIVERSITAT ROVIRA i VIRGILI
Departament de Química
Física i Inorgànica

Campus Sescelades, Edifici N4
Marcel.lí Domingo, 1
43007 Tarragona
Tel. +34 977 55 97 69
Fax. +34 977 55 84 46
www.urv.cat/dqfi

Coen de Graaf, ICREA researcher, and Xavier Lòpez, Professor of the Departament de Química Física i Inorgànica of the Universitat Rovira i Virgili, state that the present study, entitled

Electronic structure calculation on Extended Metal Atom Chains. Insights on structural, magnetic and transport properties.

presented by Mariano A. Spivak for the award of the degree of Doctor, has been carried out under our supervision at this Department.

Tarragona, 30th November, 2016.

Thesis Director

Dr. Coen de Graaf

Thesis Co-Director

Dr. Xavier Lòpez

Acknowledgments

First and foremost, I want to thank my supervisors Dr. Coen de Graaf and Dr. Xavier López for giving me the opportunity to explore the world of theoretical and computational chemistry. I value greatly the fruitful discussions, their contributions and the patience, trust and freedom they gave me to pursue and learn different methodologies, which resulted in the collection of experiences that are now part of this doctoral thesis.

Secondly, I want to thank Prof. Rosa Caballol for accepting me into the group, teaching me electronic structure theory and working with me during my time as a Master student. I would also like to thank the past and present members of the Quantum Chemistry group for their advice and collaboration (especially Josep, Gerard, Sergi, Pedro, Jhon and Pablo J.). Moreover, I would like to acknowledge Elisenda, Moises and Jose for all the technical support they provided me.

I would like to thank Prof. John McGrady and the Computational Inorganic Chemistry group at Oxford (Vaida, Karrar, Daniel) where I learned electron transport calculations. The group has been a source of friendships as well as good advice and collaborations.

I am especially grateful to Prof. Laura Gagliardi and the members of the Gagliardi Research group in Minneapolis for introducing me into new methods of electronic structure theory. The work on magnetism in EMACs would not had been possible without their advice and collaboration. I acknowledge Varinia and Kostas for the friendly environment and their insights into multiconfigurational theory.

I would like to thank Prof. Daniel Laría and Darío Estrin from University of Buenos Aires, to whom I owe my love for physical and theoretical chemistry.

I gratefully acknowledge the funding from the Ministry of Economy of Spain (MINECO) under the FPI program, which made this thesis and the external collaborations possible.

My time in Tarragona was made enjoyable thanks to my closest friends, Victor, Daniela and Javier, who gave me support and share with me the arduous path of a doctoral student.

Lastly, I would like to thank my family for their love and confidence. I am extremely thankful to my beloved life partner Anahid, who supported me during this journey and encouraged me to strive towards my goals.

Abstract

The Extended Metal Atom Chains (EMACs) form a family of compounds with interesting redox and magnetic properties. Formed by transition metal atoms arranged in a linear fashion supported by organic equatorial ligands, EMACs can be thought of as the nano-scale equivalent of traditional wires, not only structurally, but also functionally. Electron transport has been observed for Cr and Ru EMACs, which have been labeled as nanowires, making these compounds candidate materials in the field of electronics. In addition, the structural flexibility of the metal chain can be regulated by axial inorganic ligands, varying the metal-metal interactions from covalent multiple bonds to (antiferro) magnetic coupling.

The case of chromium EMACs has attracted attention since they combine both electron transport and structural flexibility, potentially opening the possibility to control the conductivity by externally changing the structure of the EMAC. However, the characterization of the relevant structures has been difficult because the X-Ray experiments have to deal with the intrinsic disorder of the moving central atom and are necessarily done in a crystal, which may not give exactly the same structure as in a device configuration. In addition, theoretical calculations based on Density Functional Theory (DFT) have been unable to describe correctly the asymmetric structures formed by weak sigma-donor ligands (i.e. nitrate). Furthermore, the simulation of the conductance of chromium EMACs has shown that the asymmetric structures are better conductors than the symmetric ones, against rational thinking. As such, the correct determination of the chromium EMAC structures is of paramount importance, in order to avoid any mismatch between the target properties and the outcomes of a real-world technological application.

In this work, we study the electronic structure of different chromium EMACs using multiconfigurational methods, CASSCF/CASPT2. We simulate the Potential Energy Surface (PES) spanned by the Cr-Cr distances to characterize the energetically most favored structures and the overall shape of the energy landscape to establish which low-lying states are accessible at room temperature. The structural characterization of the cyano (CN) and nitrate (NO_3) derivatives by CASSCF/CASPT2 leads to symmetric and asymmetric structures, respectively, in agreement with experiment. The isothiocyanate (NCS) is described as symmetric, with the possibility of accessing asymmetric isomers at low relative energy. In all cases, the energy landscape is surprisingly flat to the movement of the central atom, which indicates that the access of thermal energy in the device configuration (technological application) can result in a collection of structures which will average the electron transport properties. To probe these, we perform ab initio molecular dynamic simulation at room temperature to study the movement of the metal chain and the favored arrangements. The results confirm the difference between fundamentally asymmetric (NO_3) and symmetric (CN, NCS) structures. The thermal energy is a factor to consider, since it can tip the scale in favor of the asymmetric cases in CN and NCS. In addition, we study the crystalline phase of the aforementioned compounds to analyze the effects of the neighboring interactions and solid packing. The calculations suggest that the asymmetric structures are favored in the crystalline phase due to these effects.

The various metals and interactions present in the EMACs family form a perfect case to investigate metal-metal bonding. In general, the bonding analysis is done for bimetallic structures but the EMACs offer the possibility to study structures with 3-center bonds present in larger metallic arrays. In this thesis, we analyze the Effective Bond Order (EBO) based on CASSCF natural occupation numbers for different chromium dimers and EMACs Cr_2M (M = Cr, Mn, Fe, Ni, Zn). The results indicate that the σ and π manifolds are responsible for the most relevant contributions to the bond formation, and confirm that the heterometallic chains are composed by a Cr_2^{4+} dimer with a M^{2+} ion at non interacting distance. For the trichromium chains, we propose a strategy to localize and quantify the contributions of each Cr-Cr pair to the bond, for the cases of delocalized 3-center bonding. The results proved to differentiate between fully delocalized symmetric and partially/highly asymmetric chains.

Regarding the magnetism of EMACs, we propose the use of a recently developed method to treat efficiently the dynamic correlation in transition metal compounds. MCPDFT is a theory that combines the multiconfigurational treatment of the wave function of MCSCF methods with the dynamical correlation correction in a DFT-based formalism. We apply MCPDFT to calculate the magnetic coupling constant (J) of Nickel based EMACs. Compared to the standard CASPT2 calculations, MCPDFT correction is inexpensive and can be used to treat larger and more complicated systems, like five-nickel EMACs. These are the first results of the MCPDFT method applied to magnetic interactions for such a large compound.

Finally, we performed calculations based on Non-Equilibrium Green's Functions at the DFT level to simulate two ruthenium based EMACs in a device configuration, i. e. a molecule in between two gold electrodes. We investigate the asymmetry of the npa ligand and how this affects the rectifier character of the compound. In addition, we propose two strategies to obtain information on ionic species in the semi-periodic environment. First we use a metallic gate electrode that can modulate continuously the molecular levels of the EMACs and create positive or negatively charged molecules with different transmission properties. We also suggest a more chemical intuitive approach that consists of adding an extra atom to the cell with the purpose of creating an ionic pair. Both methods give roughly the same results but the gate electrode provides a seamless and reproducible alternative.

Contents

Contents

Contents

Chapter 1

Introduction

Material Science is a multidisciplinary field that aims for the discovery and design of new materials that can be used to improve existent devices or develop new applications of technological interest. Such development towards new materials requires the understanding of the relationship between structure, processing and properties of matter, and for such purpose, it includes the fields of chemistry, physics and engineering among others.

In the area of electronics, one of the technological goals has been increasing the number of electronic components in a circuit, and at the same time improving the performance, while reducing its size [1]. However, traditional silicon based components have reached a limit in terms of miniaturization. It is becoming increasingly difficult to make them smaller and still obtain efficient operation. Reducing their size creates heat dissipation and interference/tunneling problems, and also manufacturing/production difficulties.

One of the alternatives is to switch to molecular scale materials that can work as components in a nano-circuit. At this scale, quantum mechanical effects become important making matter behave differently than in the macroscopic materials. Therefore, the study of nano-scale materials involves methods that describe the electronic structure of matter. The ability to transport electronic charge is fundamental and π-conjugated organic systems (graphene, nanotubes) have been the focus of many

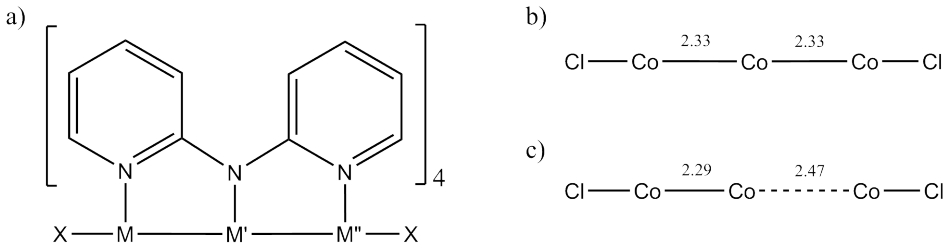

Figure 1.1. General structure of MM'M"$(dpa)_4(X)_2$ (a). Extracts of the metal chain of symmetric (b) and asymmetric (c) $Co_3(dpa)_4Cl_2$.

studies [2]. In addition, molecular switches require species with reversible access to magnetic or oxidation states of different character. In this sense, transition metal atom arrays supported by organic ligands, could offer paramagnetic states and spin polarized currents [3].

1.1 Extended Metal Atom Chains

Among the candidates that could be used in nanoelectronics are the Extended Metal Atom Chains (EMACs). Identified as nanowires, EMACs present interesting redox, magnetic and structural properties, gathering focus as new materials for electronics.

The EMACs compounds consist of three or more transition metal ions arranged in a (nearly) linear fashion, held together by multidentate organic ligands. The general formula for the three metal case is MM'M"$(L)_4(X)_2$, and the family includes homo- (M = M' = M") and heterometallic (usually M = M' $\neq$ M") chains with up to eleven metals from all three transition series (Figure 1.1(a)). The most common chelating ligand (L) is the anion of di-2,2'-pyridylamine (dpa) and different terminal ligands (X) can be used to tune the electronic properties of the chain and, in some cases, attach the complexes to metallic electrodes and use the EMACs as nanowires.

Experimental measurements of the electrical conductivity through the EMACs show strong dependence with the nature of the metal atom and theoretical investigations revealed that both electronic and geometrical factors play an important role in this property [4–6]. An essential parameter in this aspect is the asymmetry of the bond

lengths along the metal chain. Whereas heterometallic complexes present different metal–metal distances by definition, homometallic species can appear both in symmetric (equal distances) and asymmetric forms. This is nicely illustrated in the $Co_3(dpa)_4Cl_2$ complex [7] which presents both structures depending on the experimental conditions of the synthesis (Figure 1.1 (b) and (c)). Several studies tried to identify the spin character of the ground state of the two isomers, but the results are still open to discussion [8, 9].

Chromium containing EMACs have been perhaps the more extensively studied systems due to their structural versatility and complexity. After the $Cr_3(dpa)_4Cl_2$ structure was reported by Cotton's group in 1997 [10], many Cr_2M (M = Cr, Mn, Fe, Co, Ni, Zn) compounds have been synthesized. The heterometallic chains have been defined as a Cr_2^{4+} dimer with a pseudo-octahedral M^{2+} ion at non bonding distance. The Cr_3 compounds present a wider range of structures depending on the axial ligand (X = Br, I, NO_3, BF_4, CN, NCS). It has been observed that strong sigma-donor ligands (for example CN^-) favor symmetric structures, whereas weak sigma-donor ones (NO_3^-) tend to produce asymmetric geometries. Both forms have an $S = 2$ electronic ground state but the exact details of magnetic structure are not fully unraveled. Unfortunately, theoretical calculations (DFT) have been unable to obtain the experimentally assigned asymmetric structures and invariably predict structures with two equal Cr–Cr distances. The unequivocal determination of the structure of EMACs is of great importance because electron transport properties are affected by distortions of the Cr_3 chain [5].

1.2 Theoretical challenges and Objectives

The EMACs family extends to systems with different metal-metal interactions, from multiple bonds in the Cr_2M series to weak magnetic coupling in Ni_3. The description of the electronic structure of multiple bonds between transition metals has proven to be a complicated task for theoreticians. The nd electrons create many quasi-degenerate electronic states that require a multiconfigurational (MC) approach to the wave function. The chromium dimer (Cr_2) is perhaps the most revised and confronted case of multiconfiguration every time a new MC method is developed.

Chromium EMACs appear as the natural extension to the chromium dimer problem, and present both a challenge and an opportunity to explore the chemistry of metal-metal bonding. These systems, with typically 90 or more atoms, are usually theoretically treated with Density Functional Theory (DFT), but the pronounced MC character of the electronic structure may be taken as an indication that DFT is not giving the definite answer in all cases. Previous studies on the magnetism of nickel EMACs have shown the CASSCF/CASPT2 method to be a good alternative. Our goal is to extend its use to the aforementioned problem and in doing so, lay the fundament for a general applicable alternative to DFT in these medium-sized systems. Different aspects relevant to electron transport are studied.

The first objective is to establish a relation between the nature of the axial ligand and the structure of the trichromium backbone. A potential energy surface is calculated as function of the distortions in the chain and subsequently the results are mapped on a simple model Hamiltonian. Using this model, we analyze the interactions that are at the origin of the symmetric versus unsymmetric structures of the different EMACs. This study is described in chapter 3.

These static gas phase studies of chapter 3 only tell part of the story. Thermal motion and crystal packing can have an important impact on the structure. Therefore, we complete the study of the relation between structure and axial ligands in chapter 4 by performing molecular dynamics simulations on different EMACs either in gas phase or in a crystalline environment.

After studying the trichromium chains, we extend the study to the heterometallic chains Cr_2M. Here we will focus on the nature of the bonds in the chain. We determine the effective bond order and how this varies with distance. Furthermore, we propose a new strategy to get insight in the individual bonds via a localization procedure of the molecular orbitals. In this way, the different contributions to the bond can be identified. The results are described in chapter 5.

While multiconfigurational studies on EMACs are already rather scarce, there is no literature concerning the application of this kind of calculations on larger EMACs. In chapter 6 we will lay the foundations for extending the applicability of wave function based methods beyond the trimetallic limit. For this purpose, we study the magnetic interactions in Ni_5 systems by means of a hybrid method that takes

into account the static electron correlation through a multiconfigurational approach and then corrects the energies due to the lack of dynamic correlation by a density functional based formalism.

The last, but certainly not least important objective of the thesis is to establish how the application of a gate voltage affects the conductivity of an EMAC. This is done through a DFT-based calculation of the transport properties of two triruthenium EMACs. We design a device configuration with a gate electrode that can modulate the molecular energy levels and explore almost continuously all the possible redox states. Secondly, we explore an alternative that consist of adding to the scattering region a counter ion which can form an ionic pair with the molecule and obtain transmission spectra for the charged species.

Chapter 2

Methods

A physical system at the quantum level is described by the interactions between its subatomic particles (electrons and nuclei). In principle, these interactions create a complex mathematical problem which has found no exact solutions up until this date. However, exactly solving a complex equation does not necessarily lead to a full understanding of the physics of a system. In many cases, a description in terms of simple concepts is more compelling when it comes to communicating results to other scientists and this becomes of vital importance to cross the border of our research area. The impossibility to obtain an exact quantum mechanical description of any N-electron system forced quantum chemists and physicists to create methods that can extract detailed information through a series of clever approximations, and hence, increase the level of understanding of the relevant properties of matter.

Most of the methods that try to solve the N-electron problem from first principles (ab initio or without any empirical information) are based on the Schrödinger equation, which presents the wave function as the entity that contains all the quantum information of the system. In the general case, the variables in the wave function are all the relative positions of the charged particles (electrons and nuclei) and time. In practice, the problem is simplified by separation of variables: in stationary systems the wave function does not change with time and the time-independent Schrödinger equation can be used.

A second separation of variables is introduced by applying the Born-Oppenheimer (BO) approximation: based on the difference of mass between electrons and nuclei, the motion of electrons follows instantly the motion of nuclei and thus the wave function is decoupled into a product of a nuclear and an electronic part.

The hamiltonian ($\hat{H}$) is the energy operator and contains kinetic and potential terms. In the context of the BO approximation, the terms that depend on the coordinates of the nuclei are constant and the electronic hamiltonian ($\hat{H}_{el}$) can be defined as:

$$\hat{H}_{el} = -\sum_{i} \frac{1}{2}\nabla_i^2 - \sum_{\mu,i} \frac{Z_\mu}{|r_\mu - r_i|} + \sum_{i<j} \frac{1}{|r_i - r_j|} + \sum_{\mu<\nu} \frac{Z_\mu Z_\nu}{|r_\mu - r_\nu|} \tag{2.1}$$

where i and j denote the electrons and μ and ν the nuclei. The electronic structure methods focus on solving the time-independent Schrödinger equation within the BO approximation:

$$\hat{H}_{el}(r, R)\psi_{el}(r, R) = E_{el}(R)\psi_{el}(r, R) \tag{2.2}$$

where r and R refer to electronic and nuclear coordinates respectively, and the electronic energy (E_{el}) depends parametrically on R.

2.1 Hartree-Fock

The Hartree-Fock (HF) method provides a mean-field solution to many-electron systems and it has been the starting point for the more accurate electronic structure methods that are being used nowadays.

The method uses Slater determinants for the mathematical expression of the wave function in terms of the coordinates of the electrons (x_n).

$$\psi(x_1, x_2, ..., x_n) = |\phi_i(x_1)\phi_j(x_2)...\phi_k(x_n)\rangle = |\phi_i\phi_j...\phi_k\rangle \tag{2.3}$$

where ϕ_i is a one-electron function, better known as orbital. This formulation of the N-electron wave function fulfills the requirement of the wave function to be antisymmetric with respect to the exchange of the coordinates of two electrons (Pauli Exclusion Principle).

$$\psi(x_1, x_2, ..., x_n) = -\psi(x_2, x_1, ..., x_n) = -|\phi_j \phi_i ... \phi_k\rangle \tag{2.4}$$

In addition, it defines reasonably well the expectation values of the two-electron operators, when the Coulomb ($\hat{J}$) and exchange ($\hat{K}$) operators are introduced, $\hat{P}_{12}$ is the permutation operator.

$$\hat{J}_i = \sum_{j \neq i}^{N} \langle \phi_j | \frac{1}{r} | \phi_j \rangle \tag{2.5}$$

$$\hat{K}_i = \sum_{j \neq i}^{N} \langle \phi_j | \frac{\hat{P}_{12}}{r} | \phi_j \rangle \tag{2.6}$$

The Coulomb term can be interpreted as the classical electrostatic repulsion between electrons in ϕ_i and ϕ_j. The exchange term appears as a consequence of the antisymmetry of the wave function and has no classical correspondence.

The approximation of the N-electron wave function by a single Slater determinant allows us to rewrite the Schrödinger equation as a set of N effective one-electron equations

$$\hat{f}_i \phi_i = \epsilon_i \phi_i \tag{2.7}$$

where $\hat{f}_i$ is the Fock operator, sum of the one-electron terms (kinetic energy and electron-nuclei interaction) and the Coulomb and exchange operators defined above.

Using an iterative procedure, called Self Consistent Field (SCF), HF obtains the one-electron orbitals that minimize the energy for the single determinant wave function. As expected, the method fails when the wave function cannot be described correctly with a single determinant, as in the case of closely degenerate states (for example bond dissociation or partially filled d-shell metals).

2.2 Correlation energy and Post-HF methods

An improved wave function can be obtained by considering a linear combination of Slater determinants. Starting from the HF result $|\psi_0\rangle = |\phi_1 ... \phi_i \phi_j ...\rangle$, excited determinants $|\psi_i^r\rangle$ can be created by promoting electrons from the occupied orbitals (i, j) to the unoccupied (virtual) orbitals (r, s). When all possible excited determinants are taken into account, the Full Configuration Interaction (FCI) wave function is obtained:

$$|\Psi_{FCI}\rangle = |\psi_0\rangle + \sum_{i,r} c_i^r \, |\psi_i^r\rangle + \sum_{i,j,r,s} c_{ij}^{rs} \, |\psi_{ij}^{rs}\rangle + ... \tag{2.8}$$

The FCI method obtains variationally the coefficients (c) that minimize the energy, and it is exact for a given basis set. The method is computationally very demanding and it is only applicable to small systems and basis sets. The difference between the FCI and HF energies is known as the correlation energy. Post-HF methods try to accurately estimate the correlation energy for cases where FCI is computationally unfeasible.

2.3 Multiconfigurational SCF methods

The multiconfigurational self-consistent field (MC-SCF) methods approximate the N-electron wave function as a linear combination of Slater determinants and minimize the energy with respect to the configuration interaction (CI) expansion coefficients and the orbitals. MC-SCF methods differ from each other by the determinants (or configurations) included in the wave function.

The Complete Active Space SCF method (CASSCF) [11] is one of the most widely used methods because it offers a chemical intuitive approach to the selection of the configurations. It defines three orbital spaces differing in the occupation numbers (η) (Figure 2.1). The inactive space contains orbitals with $\eta = 2$, typically core or semi-core orbitals that are chemically inert. The active space orbitals are allowed to have occupations from zero to two $(0 \leq \eta \leq 2)$ and they are usually the valence orbitals. Finally, the remaining orbitals go to the virtual space, with $\eta = 0$.

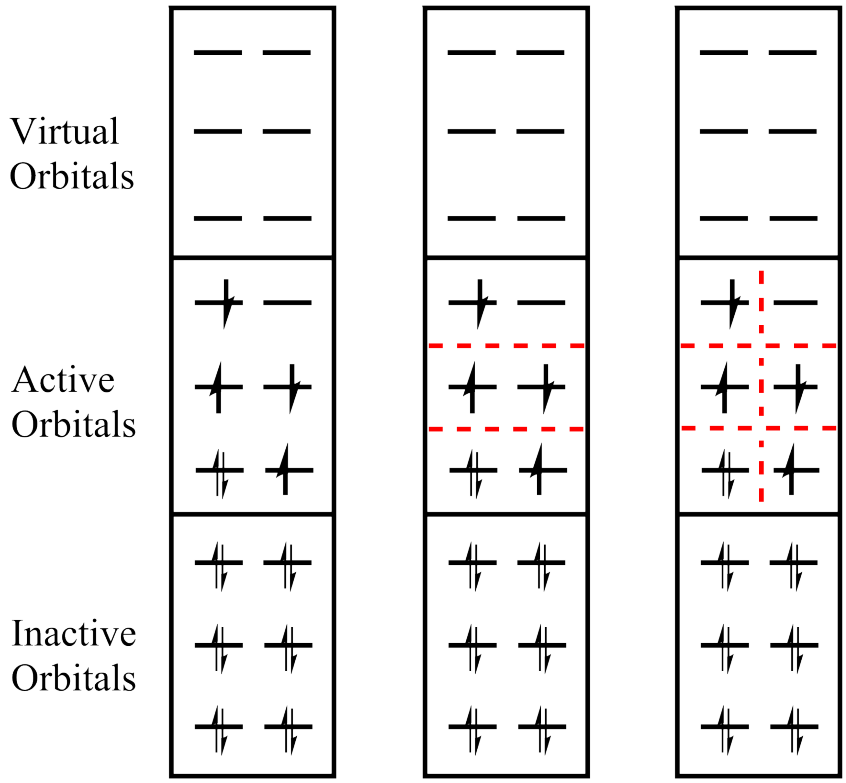

Figure 2.1. Scheme of the orbital spaces for a configuration in a CAS(6,6)(left). The RAS (center) and GAS (right) variants for the same configuration. This example contains six GAS subspaces but any arbitrary number can be used.

The active space selection requires chemical knowledge of the system and the behavior that is to be modeled. The active space is defined by the number of electrons (n) and molecular orbitals (m) and the wave function is expanded as a full CI within the CAS(n,m). In general, the larger the CAS, the more accurate results are obtained, converging in principle to the FCI result. However, the size of the CI space increases exponentially with the active space and in nearly all practical applications the limit of the CAS is reached considering 16 electrons in 16 orbitals.

The Restricted Active Space (RAS) [12] method is an extension of the CASSCF that reduces the number of configurations by creating two additional active spaces and restricting the number of electrons and holes respectively. In this way, RASSCF can work with larger active spaces without dramatically increasing the CI space.

The Generalized Active Space (GAS) [13, 14] method is based on the same idea, but with any number of active subspaces and orbital occupation numbers. GASSCF helps increasing the number of orbitals in the active space by defining the minimum and maximum number of electrons in each space. The spin multiplicity is set globally, and not for each subspace. It requires a great chemical knowledge of the system to take full advantage of the method, but it has the potential to bring within reach the MC-SCF studies of bigger molecules.

All these methods are a truncation of the FCI configuration space and this suggests that something might be missing in the estimation of the correlation energy. Typically, these methods recover the near-degeneracy correlation effects (static correlation) that appear between electrons at large separations in space. However, there is a second correlation effect (dynamic correlation) that results from the interaction between electrons at short distance [15–17]. The wave function is usually not largely affected by the dynamic correlation, but in order to obtain accurate energies the dynamic correlation needs to be considered. This can be done by large scale CI, coupled cluster and perturbation theory calculations. In the next section we present the perturbation theory approach to correct the CAS/RAS/GAS energies.

2.4 Second order Perturbation Theory in MC-SCF

Perturbation theory has been extensively used at different levels of theory. It assumes that the Hamiltonian can be partitioned in a zeroth order term ($\hat{H}_0$) and a perturbation term ($\hat{H}'$). Similarly, the wave function and energy are expanded as a polynomial of λ, the parameter that governs the perturbation. The zeroth-order Hamiltonian defines an exactly solvable model system and its solutions (eigenvalues and eigenfunctions) are used to derive equations that correct the energy and wave function of the model system upon a perturbation. In principle succesive application of higher order corrections leads to better approximations of the exact solution. In the Møller-Plesset partition, $\hat{H}_0$ is taken as the sum of the Fock operators defined in the previous section. The reference wave function is the Hartree-Fock determinant and the zeroth order energy is the sum of the orbital energies. At first-order of perturbation one recovers the Hartree-Fock energy and only at second-order of

perturbation electron correlation effects come into play. The two-electron character of the Hamiltonian combined with Brillouin's theorem makes that the first-order wave function can be restricted to the Hartree-Fock determinant and doubly excited determinants. The expression of the second-order energy correction is

$$E_2 = \sum_{i<j,r<s} \frac{|\left\langle \Psi_0 \right| \hat{H}' \left| \Psi_{ij}^{rs} \right\rangle|^2}{\epsilon_i + \epsilon_j - \epsilon_r - \epsilon_s} \tag{2.9}$$

The extension to the Multiconfigurational case (MC-PT2) has been successful in many electronic structure problems. In particular, CASPT2 [18, 19] and RASPT2 [20] have been extensively used in the study of excited states and transition metal complexes. The zeroth-order Hamiltonian in CASPT2 is the sum of one-electron Fock-type operators that exactly reduces to the Møller-Plesset Hamiltonian in the limit of zero active orbitals. With the CASSCF reference wave function, the first-order correction considers all configurations that can be generated by applying single and double excitation operators on the CASSCF wave function as a whole, that is, the so-called contracted expansion of the first-order wave function.

One of the major issues of MC-PT2 in this implementation is the possible appearance of so-called intruder states; excited configurations that make an artificially large contribution to the energy and wave function corrections. The approximate nature of the zeroth-order Hamiltonian (only containing one-electron operators) can lead to very small energy differences between the reference wave function and excited configurations. In consequence, the second-order correction to the energy becomes very large and the results are no longer reliable. The best solution to this problem is the extension of the active space in such a way that the trouble-causing configuration becomes part of the reference wave function. Alternatively, one can apply the level-shifted variant of CASPT2 or RASPT2, in which the expectation values of all external configurations are shifted up by a fixed amount to avoid near-degeneracies. The second-order estimate of the energy is a posteriori corrected for this level shift. This technique has been proved to work very well and it is the standard for the MC-PT2 calculations.

Recently, a PT2 implementation for the GASSCF wave function (GASPT2) [21] has been developed and it is expected to appear soon in the commercial version of

standard codes. It will be interesting to see the results on larger molecules, since MC-PT2 has been restricted to small/medium size systems and active spaces.

2.5 Density Functional Theory (DFT)

A different approach is used in Density Functional Theory methods. The idea in DFT is to express the electronic energy as a functional of the electron density ($\rho(r)$), which is related to the probability of finding an electron in position r.

Hohenberg and Kohn provided mathematical proof that the electron density determines the nucleus-electron interaction V_{ne} and that there is a universal functional $F[\rho]$ that describes the kinetic $T[\rho]$ and electron-electron interaction $V_{ee}[\rho]$ energies.

$$E[\rho] = V_{ne}[\rho] + T[\rho] + V_{ee}[\rho] = V_{ne}[\rho] + F[\rho] \tag{2.10}$$

They proposed a variational method to find $F[\rho]$, but the exact functional is still unknown. In an attempt to solve the problem, Kohn and Sham proposed a theory that defines $F[\rho]$ as the sum of three terms: the classical Coulomb repulsion $J[\rho]$, the kinetic energy of a system with non-interacting electrons $T_s[\rho]$ and a term called exchange-correlation energy $E_{XC}[\rho]$.

$$F[\rho] = T_s[\rho] + J[\rho] + E_{XC}[\rho] \tag{2.11}$$

They introduce orbitals to the problem in a formalism that resembles Hartree-Fock theory and calculated exactly the first two terms. The third term, that contains the electron-electron interactions and a small kinetic part, must be approximated for the electronic energy to be obtained.

$$E[\rho] = V_{ne}[\rho] + T_s[\rho] + J[\rho] + E_{XC}[\rho] \tag{2.12}$$

There are different levels of approximation of the exchange-correlation energy, but most of the methods split the term into an exchange part $E_X[\rho]$ and a correlation part $E_C[\rho]$.

$$E_{XC}[\rho] = E_X[\rho] + E_C[\rho] \tag{2.13}$$

In the simplest method, Local Density Approximation (LDA), the exchange part of the functional corresponds to the analytic expression derived by Dirac for the uniform electron gas [22] (Eq. 2.14) whereas the correlation energy was derived by fitting a ρ-dependent expression to accurate quantum Monte Carlo results [23]. The method has limited use but it works reasonably well for metallic systems and gives surprisingly accurate geometries for molecular structures.

$$E_X^{LDA}[\rho] = \int \rho^{4/3}(\mathbf{r})d\mathbf{r} \tag{2.14}$$

Generalized gradient approximation (GGA) functionals consider the exchange-correlation term as a function of the electron density and its gradient $\nabla\rho$. The exchange functionals extend the Dirac's form of LDA with an analytic gradient expansion. Two of the most used exchange functionals were developed by Becke (B88X) [24] and Perdew-Burke-Ernzerhof (PBE) [25].

$$E_X^{GGA}[\rho, \nabla\rho] = \int \rho^{4/3}(\mathbf{r}) f(\frac{\nabla\rho(r)}{\rho^{4/3}(r)})d\mathbf{r} \tag{2.15}$$

The GGA correlation functionals were derived to fit the energy of the helium atom, in this work we used the Lee-Yang-Parr (LYP) [26] and the Perdew (P86) [27] correlation functionals that combined with Becke's B88X give the BLYP and BP86 functionals respectively. In most cases, GGA results are an improvement over LDA, which prompted the further extension of the functionals. The meta-GGA functionals include the electron density, gradient and Laplacian ($\nabla^2\rho$) as well as the kinetic energy density (τ), making them computationally more expensive but with a wider range of applications [28].

Finally, a brief mention to the so-called hybrid functionals which has been widely used in chemistry. These functionals include a term with the exact exchange energy, calculated as in Hartree-Fock with the Kohn-Sham orbitals, using semi-empirical parameters to obtain surprisingly good results. The most used density functional is B3LYP [29], the hybrid version of BLYP.

2.6 Ab initio Molecular Dynamics

The study of stationary systems assumes that nuclei remain frozen at a certain position, and the focus is on the electronic motion. In cases like chemical reactions or thermal movement, important information can be extracted by following the behavior of the system in time. In order to simulate the temporal evolution of the nuclei, a new set of equations needs to be solved.

The most common methods that study the dynamics of atoms and molecules use the classical Newton's equations of motion. The forces that direct the trajectory of the particles can be empirically defined (classical MD, force fields) or computed from the potential energy of an electronic structure calculation (ab initio MD). The ab initio molecular dynamics methods are based on the Born-Oppenheimer (BO) approximation. In the BOMD method, each step of the nuclear motion requires solving the electronic problem, which makes the method very costly computationally.

In order to avoid the calculation of the electronic part at each step, Car and Parrinello (CP) developed a method that introduces the electronic motion as fictitious variables in the equations of motion. After an initial standard electronic structure calculation, accurate nuclear forces are computed by a fictitious dynamics of the electrons that preserves the electronic ground state of the system for each new configuration of the nuclei. The method requires smaller time steps, compared to the BOMD, but it has been proven very effective. The CPMD method made ab initio molecular dynamics a standard tool in the quantum chemistry field.

Molecular dynamics simulation are usually carried out for a constant volume, number of particles and temperature, what is called a canonical ensemble (N, V, T). In order to control the temperature, a thermostat algorithm is required. The Nosé-Hoover thermostat is one of the most used methods, which introduces in the Hamiltonian an extra degree of freedom for the heat bath.

2.7 Electron Transport Calculations

Electrical current, the flow of electrons through some species, is induced by the application of an external field. This is usually achieved by placing the species (contact) between two electrodes at a finite voltage difference (bias), what is called a

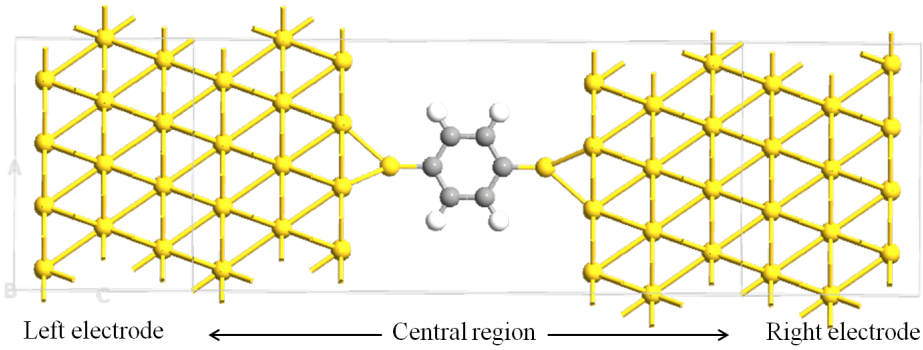

Figure 2.2. Example of a device configuration composed by gold electrodes and a benzene molecule (contact).

device configuration (Figure 2.2). The contact, initially in thermodynamical equilibrium, will evolve with time to a non equilibrium state. The simulation of a device configuration and the computation of electron transport properties (transmission and conductance) requires a method that solves the time-dependent Schrödinger equation for a complex semi-periodic system in a non equilibrium state.

A useful method that provides a solution to the aforementioned problem is based on non-equilibrium Green's Functions formalism (NEGF). NEGF can be coupled with standard electronic structure methods (for example DFT) to obtain time dependent expectation values of one-electron operators [30]. A Green's function is characterized by two space-time coordinates and describes the evolution of a system with an added (or removed) particle. In order to simplify the set up of the problem, the system is divided into three regions and it is assumed that the properties of the left and right electrodes can be modeled as a bulk, solving the fully periodic electrode cell. The central region contains a part of the electrodes so that the effective potential in the edges matches the bulk potential. The non equilibrium electron density is computed in a self-consistent procedure using the NEGF formalism for the Hamiltonian of the finite central region.

Chapter 3

The Potential Energy Surface of Trichromium EMACs

3.1 Introduction

Trichromium EMACs, $Cr_3(dpa)_4X_2$, are among the simplest yet more challenging members of the EMACs family. The axial ligands (X = Br, I, NO_3, BF_4, CN, NCS) define the structural features of the metal chain, but the complex nature of the Cr–Cr bonds makes the compounds have an inherent flexibility and their magnetic, redox and electron transport properties can, in principle, be tuned to serve many purposes. According to the sigma-donor character of the axial ligands the metal chain can be symmetric (equal Cr–Cr distances) or asymmetric. The two prototypical cases are cyanide (CN^-), which present Cr–Cr distances of 2.37 Å, and nitrate (NO_3^-) that forms an extremely asymmetric structure with distances of 1.93 and 2.64 Å.

$Cr_3(dpa)_4(NCS)_2$ is probably the most interesting compound of this family. Having sulfur's high affinity to gold and proven transmission properties make it a candidate material in electronics. X-ray diffractions for the crystal were interpreted to arise from an asymmetric structure with Cr-Cr distances of 2.23-2.48 Å and 2.21-2.46 Å for benzene and toluene crystallization solvents, respectively. Theoretical results

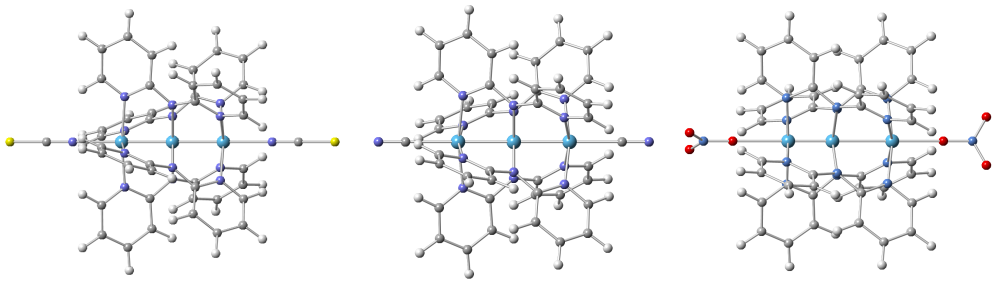

Figure 3.1. EMAC structures studied: $Cr_3(dpa)_4(X)_2$, with X = NCS^- (left), CN^- (center), NO_3^- (right). The atoms are colored in white (H), grey (C), blue (N), red (O), yellow (S) and light-blue (Cr).

obtained with DFT calculations indicated a rather flat potential energy surface (PES) which ultimately favors symmetric structures [6]. In addition, the electron transport properties follow a counter intuitive rational, where the calculated conductance is larger for an asymmetric structure than for the symmetric isomer. Given the apparent contradiction between the DFT results and the experimental structure determination, and the link between conductivity and symmetry of the metal chain, it is of paramount importance to identify the structural motifs of the molecule that can be present in a device configuration. The apparent flexibility of the chain would allow for a collection of structures that would average the properties and result in a less controlled technological application.

Considering the large number of unpaired electrons of the Cr(II) d^4 ion, a substantial multiconfigurational (MC) character can be anticipated for the metal chain. Hence, it has to be established to what extent a monodeterminantal approach such as DFT is able to correctly describe the potential energy surface of the EMACs with three Cr ions and to decide on the relative stability of the symmetric and antisymmetric forms. In this work we use multiconfiguration wave function methods to obtain information on the electronic structure of three chromium EMACs (X = NCS, CN and NO_3, Figure 3.1) and investigate the energy landscape of possible symmetric and asymmetric structures of the gas phase. In addition, we shed light on the metal–metal bonding character which will be explored in detail in chapter 5.

3.2 Computational Information

The full geometry optimization of the EMAC is in general computationally too expensive for a MC wave function approach, all the more when dynamic electron correlation is considered. Therefore, we first generate a set of DFT optimized structures where all but the Cr-Cr distances were relaxed. Then, MC single point energy calculations on the DFT structures are carried out to construct the potential energy surface (PES) and determine the optimal Cr-Cr distances.

DFT geometry optimizations were performed with GAUSSIAN 09 [31], using the BP86 [32] functional with the def2-TZVP basis for the one-electron functions of Cr and def2-SVP for the rest of the atoms (H, C, N, O, S) [33]. The geometry is optimized for the $M_S = 2$ determinant with up-down-up spin ordering on the three Cr ions. Note that this determinant does not represent a real quintet state but rather a mixture of different spin eigenfunctions, as usual in the broken symmetry approach [34].

Multiconfigurational wave functions were constructed following the complete active space self-consistent field (CASSCF) approach. The active space contains twelve orbitals and twelve electrons. The active orbitals are depicted in figure 3.2 and can be considered to a large extent as twelve different linear combinations of the atomic Cr-3d orbitals that hold the unpaired electrons of the Cr(II) ion in a (quasi-)octahedral coordination sphere. The active orbitals are labeled as *bonding*, *anti-bonding* and *non-bonding orbitals*, and also by their symmetry character with respect to the rotation around the Cr-Cr-Cr axis as σ, π or δ. CASSCF accurately accounts for non-dynamic electron correlation related to the near-degeneracy of several electronic configurations but does not provide reliable relative energies because it does not include the effect of dynamic electron correlation. This effect was included by complete active space second-order perturbation theory (CASPT2) using the CASSCF wave function as zeroth-order description.

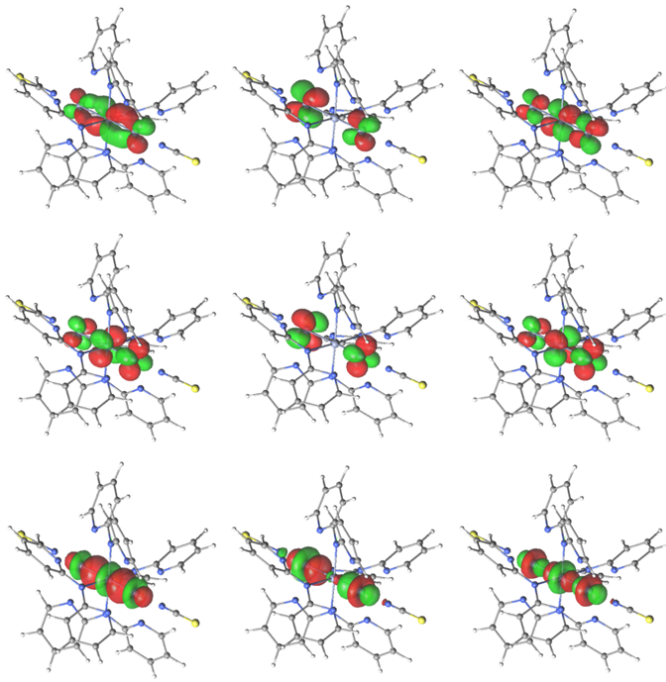

Figure 3.2. Active molecular orbitals for $Cr_3(dpa)_4(NCS)_2$ of the CASSCF calculations. The MOs are classified in σ (bottom), δ (middle) and π (top) character and bonding (left), non-bonding (center) and anti-bonding (right) type. Only 3 out of 6 π orbitals are shown, the other three are obtained by a 90 degree rotation around the Cr-Cr-Cr axis.

CASSCF/CASPT2 single point calculations were done with MOLCAS 7.8 package [35]. Atomic natural orbitals optimized for relativistic corrections and core correlation (ANO–RCC) basis sets were used to expand the orbitals [36]. The large primitive set of functions is contracted to [2s] for H, [3s,2p] for C, [4s,3p,1d] for N and O, [4s,3p] for S and [6s,5p,4d,2f,1g] for Cr. Scalar relativistic effects were included using the Douglas–Kroll–Hess Hamiltonian. The computational costs from the two-electron integrals were reduced by the Cholesky decomposition technique (threshold was set to 10^{-8} a.u.) [37]. We used the standard zeroth-order Hamiltonian and an imaginary shift of 0.2 a.u. to avoid the appearance of weak intruder states in the CASPT2 calculations. All single point calculations were performed for the electronic state with quintet spin coupling arising from the antiferromagnetic coupling of the S = 2 spin moments of the Cr(II) ions in the EMAC.

The contour plots were obtained with the program Surfer® 12 [38]. The Kriging interpolation method (slope=1, anisotropy=1;0) was used to construct the surfaces from the calculated energies, which are represented as red dots.

3.3 Potential Energy Surfaces

In this section we explore the Potential Energy Surface (PES) of trichromium EMACs in terms of the Cr–Cr distances. We are interested in the regions of minimum energy, but most importantly the shape and depth of the PES which in principle can allow multiple structures given accessible thermal energy. Previous DFT results indicated very small energy differences between symmetric and asymmetric structures, ultimately favoring symmetric global minima for all the compounds.

We obtained the DFT and CASPT2 PES, which are represented in Figure 3.3. The best match between DFT and CASPT2 features occurs for $Cr_3(dpa)_4(CN)_2$. Both methods present a fairly flat PES with the symmetric region having the minimal energy. This structure has been experimentally characterized as symmetric, suggesting that DFT should be able to predict the Cr–Cr X-ray distances, and indeed it does surprisingly well (Table 3.1). The CASPT2 minimum has longer Cr–Cr distances (2.42 vs 2.37 Å) but the PES is slightly less shallow in the symmetric region, compared to the very extended DFT.

The first differences between DFT and CASPT2 are evident in the $Cr_3(dpa)_4(NCS)_2$ case. While DFT does not change the flatness nor the minimum structure from the previous compound, CASPT2 does present some new features. The PES at CASPT2 level presents multiple minima in the symmetric region (equal Cr–Cr distances) with the most stable one characterized by Cr-Cr distances of 2.33 Å. In addition, the surface shapes into an asymmetric minimum around 2.0-2.6 Å, 2.3 kcal/mol higher than the symmetric one. None of these minima matches the experimental structure (2.23-2.48 Å), which according to the CASPT2 PES would be a saddle point. Such differences should be attributed to the fact that present calculations represent an isolated molecule (gas phase), whereas the experimental structure is characterized in the crystalline phase where neighboring molecules in the solid can interact and change the landscape. However, the technological application of these

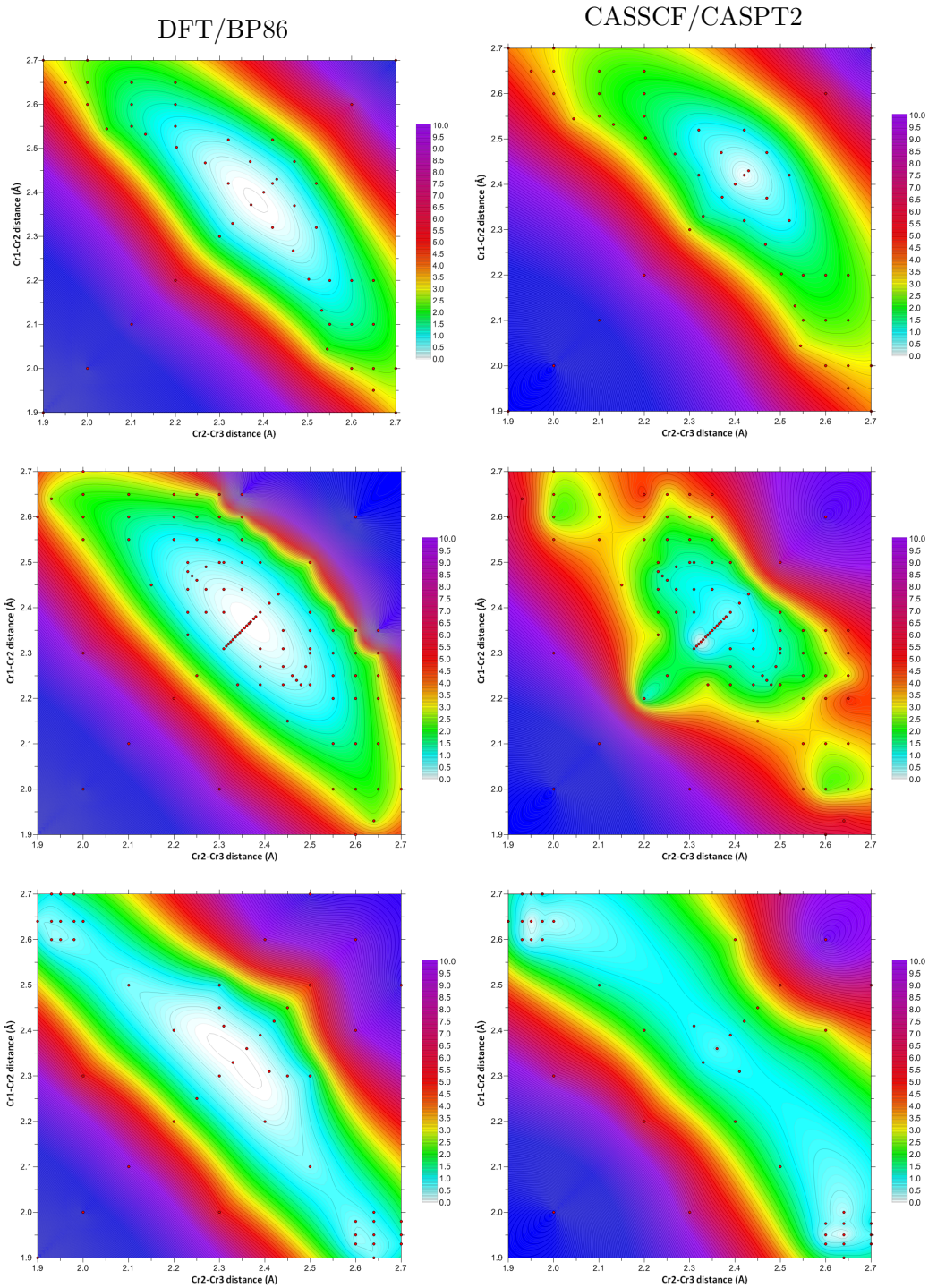

Figure 3.3. BP86 and CASPT2 Potential Energy Surfaces (PES) contour plots (kcal/mol) for CN (top), NCS (center) and NO_3 (bottom).

Table 3.1. Most relevant distances (Å) from the X-Ray characterization and calculated DFT and CASPT2 minima of the three chromium EMACs.

	$\mathbf{Cr_1}$-$\mathbf{Cr_2}$	$\mathbf{Cr_2}$-$\mathbf{Cr_3}$	Cr-$\mathbf{N}_{in}$	Cr-$\mathbf{N}_{out}$	Cr-$\mathbf{N}_{ax}$
$Cr_3(dpa)_4(CN)_2$					
X-Ray	2.37	2.37	2.03	2.12	2.28
DFT	2.37	2.37	2.04	2.12	2.19
CASPT2	2.42	2.42	2.06	2.14	2.28
$Cr_3(dpa)_4(NCS)_2$					
X-Ray	2.23	2.48	2.04	2.11	2.20
DFT	2.37	2.37	2.04	2.12	2.10
CASPT2	2.33	2.33	2.06	2.13	2.23
$Cr_3(dpa)_4(NO_3)_2$					
X-Ray	1.93	2.64	2.04	2.11	2.09 ; 2.30
DFT	2.33	2.33	2.04	2.10	2.14
CASPT2	1.95	2.64	2.06	2.11	2.25 ; 2.44

EMACs is foreseen as single molecule devices, which have little to no intermolecular interactions and resembles more the gas phase than the crystal.

Finally, $Cr_3(dpa)_4(NO_3)_2$ results show extremely flat PES with DFT favoring again a symmetric global minimum. On the other hand, CASPT2 depicts the lowest minimum in the asymmetric region (1.93, 2.64 Å), very close to the experimental structure of 1.95 and 2.64 Å. This case confirms that CASPT2 is not biased towards symmetric structures like DFT appears to be. In other words, CASPT2 can reproduce the experiment in the two prototypical examples (CN and NO_3), and this could help to validate the NCS results.

The results of the global minima are presented in Table 3.1. In summary, whilst both DFT and CASPT2 agree that the potential energy surfaces are very flat, there are marked differences between the two methods, which suggest that the MCSCF approach captures the difference between the symmetric and unsymmetric structures more accurately.

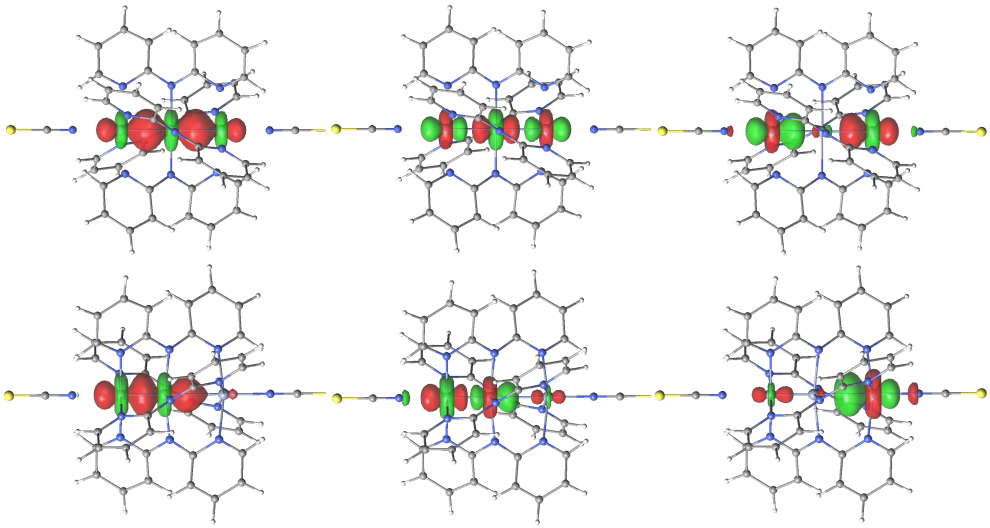

Figure 3.4. Sigma Natural Molecular Orbitals for the symmetric (top, 2.33–2.33 Å) and asymmetric (bottom, 1.93–2.64 Å) NCS structures. Orbitals can be classified as Bonding (left) antibonding (middle) and non-bonding (right).

3.4 Wave function analysis

Although the quintet spin eigenfunction of a system with 12 unpaired electrons is by definition a linear combination of many determinants, this does not necessarily imply a multiconfigurational wave function. The typical description of the Cr-Cr bonds in the trinuclear EMACs as a 3-center/3-electron case suggests a wave function dominated by a single electronic configuration, such as

$$|(\sigma)^2(\sigma_{nb})^1(\sigma^*)^0(\delta)^1(\delta_{nb})^1(\delta^*)^1(\pi)^1(\pi_{nb})^1(\pi^*)^1|$$

where the molecular orbitals correspond to those of Figure 3.2. In this section we will analyze the multiconfigurational nature of the CASSCF wave function and the importance of other electronic configurations in the symmetric and asymmetric forms of the Cr *trimer* and put the 3-center/3-electron picture to the test.

Figure 3.4 shows the σ natural molecular orbitals for two structures of the NCS case, symmetric (top) and asymmetric (bottom). It can be seen that the symmetric structure, which corresponds to the lowest minimum at CASPT2 level with Cr-Cr distances of 2.33 Å, has the orbitals delocalized in the three Cr atoms. However, in

the asymmetric structure (1.93–2.64 Å) the bonding and antibonding orbitals have contributions almost exclusively from the short–distance pair. This pseudo dimeric representation appears only for highly asymmetric structures, when the difference between distances is greater than 0.6 Å. Table 3.2 lists the most important configurations of the CAS(12,12) wave functions for the two cases. All configurations listed in Table 3.2 have three electrons in the σ, δ, π_x and π_y orbitals, all other configurations with more (or less) electrons in one of the orbital manifolds have negligible weight in the wave function. The most striking result from this wave function analysis is that the electronic structure of the Cr_3 complex is highly multiconfigurational. There is no clearly dominating electronic configuration, neither in the symmetric nor in the asymmetric form. The largest contribution in the former is less than 11%, while it increases somewhat to approximately 34% in the latter. The traditional picture in terms of a three-center/three-electron bond is obviously only part of the story, since it only accounts for 10.7% (6.6%) of the wave function in the symmetric (asymmetric) complexes.

The situation becomes clearer if we consider each symmetry-distinct manifold (σ, δ, π) in turn and collect together all configurations with a common component. For example, the combined weights of all the CSFs that contain $(\sigma)^2(\sigma_{nb})^1(\sigma^*)^0$, regardless of the distribution of electrons in the δ and π orbitals, make up 61.4% of the total wavefunction. Table 3.3 collects the combined weights of these pseudo-configurations (PCs). The dominance of the $(\sigma)^2(\sigma_{nb})^1(\sigma^*)^0$ PC (61.4%) over its doubly excited counterpart, $(\sigma)^0(\sigma_{nb})^1(\sigma^*)^2$ PC (10.2%) would indicate a formal σ bond close to 1. At the opposite end of the spectrum, the near identical contributions of the $(\delta)^2(\delta_{nb})^1(\delta^*)^0$ and $(\delta)^0(\delta_{nb})^1(\delta^*)^2$ PCs (30.5% and 29.2%, respectively), is consistent with a negligible net contribution from δ bonding. The π manifold sits between these two extremes: contributions of 40.6% and 19.0% from $(\pi)^2(\pi_{nb})^1(\pi^*)^1$ and $(\pi)^0(\pi_{nb})^1(\pi^*)^2$, respectively, indicate a non-negligible contribution from π bonding, particularly given that there are two orthogonal π bonds to consider.

Turning to the asymmetric isomer, we note immediately that the wavefunction is dominated to a far greater extent by the $(\sigma)^2(\sigma_{nb})^1(\sigma^*)^0$ PC (77.5% vs 61.4% in the symmetric case) and, indeed, by the single configuration (34.0% in Table 3.2) $|(\sigma)^2(\sigma_{nb})^1(\sigma^*)^0(\delta)^2(\delta_{nb})^1(\delta^*)^0(\pi)^2(\pi_{nb})^1(\pi^*)^0|$. Similar features are apparent

Table 3.2. Most important configurations (%) of CAS(12,12) from two structures of $Cr_3(dpa)_4(NCS)_2$. Symmetric (2.33-2.33 Å) and asymmetric (1.93-2.64 Å).

Configurations[a]	Symmetric	Asymmetric
$(\sigma)^2(\sigma_{nb})^1(\sigma^*)^0(\delta)^2(\delta_{nb})^1(\delta^*)^0(\pi)^2(\pi_{nb})^1(\pi^*)^0$	8.4	34.0
$(\sigma)^2(\sigma_{nb})^1(\sigma^*)^0(\delta)^2(\delta_{nb})^1(\delta^*)^0(\pi)^1(\pi_{nb})^1(\pi^*)^1$	7.3	2.5
$(\sigma)^2(\sigma_{nb})^1(\sigma^*)^0(\delta)^2(\delta_{nb})^1(\delta^*)^0(\pi)^0(\pi_{nb})^1(\pi^*)^2$	3.5	3.4
$(\sigma)^2(\sigma_{nb})^1(\sigma^*)^0(\delta)^1(\delta_{nb})^1(\delta^*)^1(\pi)^2(\pi_{nb})^1(\pi^*)^0$	10.9	6.7
$(\sigma)^2(\sigma_{nb})^1(\sigma^*)^0(\delta)^1(\delta_{nb})^1(\delta^*)^1(\pi)^1(\pi_{nb})^1(\pi^*)^1$	10.7	6.6
$(\sigma)^2(\sigma_{nb})^1(\sigma^*)^0(\delta)^1(\delta_{nb})^1(\delta^*)^1(\pi)^0(\pi_{nb})^1(\pi^*)^2$	4.7	0.9
$(\sigma)^2(\sigma_{nb})^1(\sigma^*)^0(\delta)^0(\delta_{nb})^1(\delta^*)^2(\pi)^2(\pi_{nb})^1(\pi^*)^0$	6.9	18.9
$(\sigma)^2(\sigma_{nb})^1(\sigma^*)^0(\delta)^0(\delta_{nb})^1(\delta^*)^2(\pi)^1(\pi_{nb})^1(\pi^*)^1$	6.1	1.7
$(\sigma)^2(\sigma_{nb})^1(\sigma^*)^0(\delta)^0(\delta_{nb})^1(\delta^*)^2(\pi)^0(\pi_{nb})^1(\pi^*)^2$	3.0	2.4
$(\sigma)^1(\sigma_{nb})^1(\sigma^*)^1(\delta)^2(\delta_{nb})^1(\delta^*)^0(\pi)^2(\pi_{nb})^1(\pi^*)^0$	3.2	1.9
$(\sigma)^1(\sigma_{nb})^1(\sigma^*)^1(\delta)^2(\delta_{nb})^1(\delta^*)^0(\pi)^1(\pi_{nb})^1(\pi^*)^1$	3.4	2.1
$(\sigma)^1(\sigma_{nb})^1(\sigma^*)^1(\delta)^2(\delta_{nb})^1(\delta^*)^0(\pi)^0(\pi_{nb})^1(\pi^*)^2$	1.6	0.5
$(\sigma)^1(\sigma_{nb})^1(\sigma^*)^1(\delta)^1(\delta_{nb})^1(\delta^*)^1(\pi)^2(\pi_{nb})^1(\pi^*)^0$	4.8	3.9
$(\sigma)^1(\sigma_{nb})^1(\sigma^*)^1(\delta)^1(\delta_{nb})^1(\delta^*)^1(\pi)^1(\pi_{nb})^1(\pi^*)^1$	5.3	1.2
$(\sigma)^1(\sigma_{nb})^1(\sigma^*)^1(\delta)^1(\delta_{nb})^1(\delta^*)^1(\pi)^0(\pi_{nb})^1(\pi^*)^2$	2.4	0.8
$(\sigma)^1(\sigma_{nb})^1(\sigma^*)^1(\delta)^0(\delta_{nb})^1(\delta^*)^2(\pi)^2(\pi_{nb})^1(\pi^*)^0$	2.7	1.3
$(\sigma)^1(\sigma_{nb})^1(\sigma^*)^1(\delta)^0(\delta_{nb})^1(\delta^*)^2(\pi)^1(\pi_{nb})^1(\pi^*)^1$	3.0	1.6
$(\sigma)^1(\sigma_{nb})^1(\sigma^*)^1(\delta)^0(\delta_{nb})^1(\delta^*)^2(\pi)^0(\pi_{nb})^1(\pi^*)^2$	1.4	0.4
$(\sigma)^0(\sigma_{nb})^1(\sigma^*)^2(\delta)^2(\delta_{nb})^1(\delta^*)^0(\pi)^2(\pi_{nb})^1(\pi^*)^0$	1.1	1.8
$(\sigma)^0(\sigma_{nb})^1(\sigma^*)^2(\delta)^2(\delta_{nb})^1(\delta^*)^0(\pi)^1(\pi_{nb})^1(\pi^*)^1$	1.2	0.4
$(\sigma)^0(\sigma_{nb})^1(\sigma^*)^2(\delta)^2(\delta_{nb})^1(\delta^*)^0(\pi)^0(\pi_{nb})^1(\pi^*)^2$	0.7	0.8
$(\sigma)^0(\sigma_{nb})^1(\sigma^*)^1(\delta)^1(\delta_{nb})^1(\delta^*)^1(\pi)^2(\pi_{nb})^1(\pi^*)^0$	1.6	0.6
$(\sigma)^0(\sigma_{nb})^1(\sigma^*)^1(\delta)^1(\delta_{nb})^1(\delta^*)^1(\pi)^1(\pi_{nb})^1(\pi^*)^1$	1.8	0.8
$(\sigma)^0(\sigma_{nb})^1(\sigma^*)^1(\delta)^1(\delta_{nb})^1(\delta^*)^1(\pi)^0(\pi_{nb})^1(\pi^*)^2$	1.0	0.3
$(\sigma)^0(\sigma_{nb})^1(\sigma^*)^1(\delta)^0(\delta_{nb})^1(\delta^*)^2(\pi)^2(\pi_{nb})^1(\pi^*)^0$	1.0	1.3
$(\sigma)^0(\sigma_{nb})^1(\sigma^*)^1(\delta)^0(\delta_{nb})^1(\delta^*)^2(\pi)^1(\pi_{nb})^1(\pi^*)^1$	1.1	0.3
$(\sigma)^0(\sigma_{nb})^1(\sigma^*)^1(\delta)^0(\delta_{nb})^1(\delta^*)^2(\pi)^0(\pi_{nb})^1(\pi^*)^2$	0.7	0.8

a) Relevant configurations arranged by the local σ manifold configuration.

Table 3.3. Dominant pseudo-configurations contributions (%) for the three orbital manifolds in symmetric and asymmetric isomers of $Cr_3(dpa)_4(NCS)_2$.

Pseudo-configurations	Symmetric	Asymmetric
$(\sigma)^2...(\sigma_{nb})^1...(\sigma^*)^0$	61.4	77.5
$(\sigma)^1...(\sigma_{nb})^1...(\sigma^*)^1$	27.8	13.7
$(\sigma)^0...(\sigma_{nb})^1...(\sigma^*)^2$	10.2	7.0
$(\delta)^2...(\delta_{nb})^1...(\delta^*)^0$	30.5	48.0
$(\delta)^1...(\delta_{nb})^1...(\delta^*)^1$	43.1	22.0
$(\delta)^0...(\delta_{nb})^1...(\delta^*)^2$	26.0	29.2
$(\pi)^2...(\pi_{nb})^1...(\pi^*)^0$	40.6	71.2
$(\pi)^1...(\pi_{nb})^1...(\pi^*)^1$	39.9	17.6
$(\pi)^0...(\pi_{nb})^1...(\pi^*)^2$	19.0	10.5

in each of the symmetry-distinct manifolds, σ, δ and π, where the configuration with 2 electrons in the bonding orbital assumes much greater significance. These observations suggest that the four antibonding orbitals (σ^*, δ^* and 2 x π^*) are more destabilized in the asymmetric form, leading to a higher formal bond order.

3.5 Role of the terminal ligand

In order to explain the differences between the axial ligands different hypothesis have been presented. McGrady and co–workers [5] have argued that the distortion towards asymmetric Cr_3 chains is driven by the mixing of σ and σ_{nb} orbitals, only possible when the center of symmetry is removed. Strong sigma donor axial ligands will destabilize all three members of the manifold (σ, σ_{nb} and σ^*), but the non-bonding orbital will be most sensitive because it is localized solely on the terminal Cr centers. The net effect of strong σ donors is therefore to increase the separation of the σ and σ_{nb} orbitals, stabilizing the symmetric form. Berry and co-workers [39] have approached the problem from a complementary perspective, arguing that strong σ donors selectively destabilize the asymmetric structure by raising the energy of both the σ component of the localized quadruple Cr–Cr bond and the d_{z^2} orbital of the isolated Cr(II) center, but only destabilize the σ_{nb} orbital in the

delocalized alternative. On this basis they argue that in the absence of terminal ligands the Cr_3 chain should be asymmetric, and indeed calculations of the unligated dication $[Cr_3(dpa)_4]^{2+}$ confirm this to be the case. While the details of the two models are subtly different, both emphasize the importance of the sigma manifold in determining the balance between symmetric and asymmetric structures.

In this section we will show how the terminal ligand affects the wave function and ultimately the preferred structure, focusing on the configurations of the sigma manifold. Ideally, one would monitor the changes in the weights of the Configuration State Function (CSF) as a function of the axial ligand identity. However, this is not possible because the ground state CASSCF wave function has no clearly dominating CSFs that can be used to follow the variations with respect to the axial ligands. Our solution to the problem of small CSF weights has two parts. First we collapse the CSFs for the sigma orbitals like we did in Table 3.3, making use of the Generalized Active Space (GAS) restrictions. Forcing the δ and π manifolds, GAS reduces the number of CSFs to only 13, compared to over 95000 in CASSCF, most of them (8) of the general formula $(\sigma)^A(\sigma_{nb})^B(\sigma^*)^C(\delta)^1(\delta_{nb})^1(\delta^*)^1(\pi)^2(\pi_{nb})^1(\pi^*)^0$, where A+B+C = 3. Table 3.4 shows the contributions of the CSFs for the GAS ground state (S = 3) wave function, which are very similar to the pseudo–configurations presented for the CASSCF (S = 2) (Table 3.3, upper block). Since the sigma orbitals have different symmetry with respect to the inversion center (σ and σ^* *gerade*, σ_{nb} *ungerade*), the CSFs are separated in two groups of different symmetry, that interact only when the Cr_3 chain symmetry is distorted.

The second part consists of using Effective Hamiltonian theory [35, 40, 41] to map the wave function onto the small model space spanned by the eight conveniently chosen CSFs (Table 3.4). The so-obtained Effective Hamiltonian matrix elements concentrate all the information contained in the multiconfigurational wave function in a few key matrix elements ($H_{eff}(i,j)$, Equation 3.1) providing valuable information about the mechanism that governs the relative stability of symmetric and asymmetric forms of Cr_3 chains.

$$H_{eff}(i,j) = \sum_{k}^{states} CSF(k,i) * E(k) * CSF(k,j) \tag{3.1}$$

Table 3.4. Contributions (%) to the ground state GASSCF wavefunction for different symmetric structures (d(Cr-Cr) = 2.33 Å).

	GAS CSF	NO_3	NCS	CN
1	$(\sigma)^2(\sigma_{nb})^1(\sigma^*)^0$	69.5	70.0	70.7
2	$(\sigma)^u(\sigma_{nb})^u(\sigma^*)^d$	4.5	4.5	4.4
3	$(\sigma)^u(\sigma_{nb})^d(\sigma^*)^u$	12.3	12.1	11.9
4	$(\sigma)^0(\sigma_{nb})^1(\sigma^*)^2$	11.4	11.2	10.9
5	$(\sigma)^2(\sigma_{nb})^0(\sigma^*)^1$	0.0	0.0	0.0
6	$(\sigma)^1(\sigma_{nb})^2(\sigma^*)^0$	0.0	0.0	0.0
7	$(\sigma)^1(\sigma_{nb})^0(\sigma^*)^2$	0.0	0.0	0.0
8	$(\sigma)^0(\sigma_{nb})^2(\sigma^*)^1$	0.0	0.0	0.0

Table 3.5 presents the EH matrix for the symmetric minimum of $Cr_3(dpa)_4(NCS)_2$. The matrix has two blocks of CSFs and by diagonalizing the upper 4x4 matrix spanned by the *ungerade* CSFs we obtain a stabilization of the $(\sigma)^2(\sigma_{nb})^1(\sigma^*)^0$ configuration of 4.45 eV. Notice that the interaction between the $(\sigma)^2(\sigma_{nb})^1(\sigma^*)^0$ configuration and the other three *ungerade* CSFs is on the same order of magnitude. Following the same steps for the other two ligands (see annex in section 3.7), we determined that this stabilization is smaller for CN (4.34 eV) and larger for NO_3 (4.50 eV) compared to the NCS. The difference in stabilization cannot be solely attributed to changes in the diagonal elements (that is, the energies of the CSFs) but is also caused by changes in the interaction among the *ungerade* determinants. Upon further inspection, we identify the stabilization differences are caused by the H_{12} and H_{44} terms. By definition (Equation 3.1), the product of $CSF(k,i) * CSF(k,j)$ is maximum when both are equal or similarly large, which means that the matrix element reflects the degree of mixing the two CSFs (i,j) have, as in the degree of bi-configurational character of the wave function of the relevant states. The non-diagonal H_{12} term increases in absolute value as $NO_3 > NCS > CN$ which is related with the multiconfigurational character of the wave functions of the excited states ($E(k)$). It is worth mentioning that the contributions of the ground state are not directly counted, since we set its energy to zero ($E(1) = 0.0$ eV). However, the character of the ground state wave function impacts the wave function of the excited states since they all have to be orthogonal to the ground state. In sum, NO_3 has the most multiconfigurational wave function and that means the largest $|H_{12}|$

Table 3.5. Effective Hamiltonian matrix for the symmetric $Cr_3(dpa)_4(NCS)_2$ minimum (d(Cr-Cr) = 2.33 Å). All elements are given in eV.

CSFs	1	2	3	4	5	6	7	8
1	0.00	4.24	-3.43	4.60	0.00	0.00	0.00	0.00
2	4.24	10.68	-0.19	-5.27	0.00	0.00	0.00	0.00
3	-3.43	-0.19	11.50	1.60	0.00	0.00	0.00	0.00
4	4.60	-5.27	1.60	13.64	0.00	0.00	0.00	0.00
5	0.00	0.00	0.00	0.00	5.05	-4.29	1.42	4.24
6	0.00	0.00	0.00	0.00	-4.29	5.87	4.66	2.91
7	0.00	0.00	0.00	0.00	1.42	4.66	11.97	-4.29
8	0.00	0.00	0.00	0.00	4.24	2.91	-4.29	12.54

and stabilization of the $(\sigma)^2(\sigma_{nb})^1(\sigma^*)^0$ configuration.

We repeat the calculations for an asymmetric structure with d(Cr-Cr) = 2.28 and 2.38 Å, a small distortion from the symmetric minimum (d(Cr-Cr) = 2.33 Å). Table 3.6 shows there is a non-negligible mixture between the two CSFs groups but after the diagonalization, we can see that this does not affect the stabilization of the $(\sigma)^2(\sigma_{nb})^1(\sigma^*)^0$ configuration. In all cases, the stabilization of the asymmetric structure is lower than for the symmetric counterpart, but the trend is the same. This suggest that breaking the symmetry in the chain has an energy penalty for all the compounds, and the NO_3 is the one that suffers the smallest penalty. This energy stabilization cannot be used to compare structures, because it only considers a small part of the total energy. Instead, this hints towards the idea that NO_3 can surpass this asymmetrization penalty and reach highly asymmetric regions which might turn around the stabilization. The calculation of the effective hamiltonian on such structure (i.e. 1.93-2.68 Å) can show a larger stabilization that the symmetric one for NO_3. However, due to the localized nature of the molecular orbitals the analysis cannot be reproduced and/or compared with the symmetric case. In our future work, we will tackle this problem using localization techniques that allow us to work with a delocalized picture of molecular orbitals.

Table 3.6. Effective Hamiltonian matrix for an asymmetric distortion (d(Cr-Cr) = 2.28-2.38 Å) around the $Cr_3(dpa)_4(NCS)_2$ minimum. All elements are given in eV.

CSFs	1	2	3	4	5	6	7	8
1	0.00	-3.93	3.37	4.61	0.47	-0.57	0.55	-0.51
2	-3.93	10.52	0.00	5.12	-1.40	1.35	-1.04	1.11
3	3.37	0.00	11.65	-1.29	0.64	-1.13	0.62	-0.64
4	4.61	5.12	-1.29	14.14	-0.51	0.54	-0.79	0.90
5	0.47	-1.40	0.64	-0.51	5.27	4.07	-1.15	4.00
6	-0.57	1.35	-1.13	0.54	4.07	6.32	4.47	-2.85
7	0.55	-1.04	0.62	-0.79	-1.15	4.47	12.44	4.06
8	-0.51	1.11	-0.64	0.90	4.00	-2.85	4.06	13.28

3.6 Concluding remarks

In this chapter, we shed light on the multiconfigurational character of the electronic structure of chromium EMACs. The methodology used proved to be in good agreement with experiment for the cases of CN and NO_3 and we discussed the differences between the σ-donor ligands and how they influence the geometry. The wave function analysis questioned the established three-center/three-electron picture and suggested σ and π bonding might be equally important in these EMACs. In addition, we explored the effects of the ligands into the wave function and the stabilization of the dominant configuration by means of the effective hamiltonian model. The results suggest that NO_3 high multiconfigurational wave function might stabilize an asymmetric structure, while the strong σ-donor ligands cannot. All the structures had extremely flat PES as function of the Cr–Cr distances, which could indicate a high flexibility of the central atom at experimental work temperature. The challenging case of $Cr_3(dpa)_4(NCS)_2$, where experiment and theory were not in agreement, could be attributed to such flexibility of the central Cr. In the next chapter, we address the importance of temperature and the solid packing effects by means of ab initio molecular dynamics simulations.

3.7 Annex

Table 3.7. Effective Hamiltonian matrix for the symmetric $Cr_3(dpa)_4(CN)_2$ structure (d(Cr-Cr) = 2.33 Å). All elements are given in eV.

CSFs	1	2	3	4	5	6	7	8
1	0.00	4.13	-3.44	4.57	0.00	0.00	0.00	0.00
2	4.13	10.63	-0.17	-5.25	0.00	0.00	0.00	0.00
3	-3.44	-0.17	11.54	1.46	0.00	0.00	0.00	0.00
4	4.57	-5.25	1.46	13.79	0.00	0.00	0.00	0.00
5	0.00	0.00	0.00	0.00	4.96	-4.22	1.37	4.16
6	0.00	0.00	0.00	0.00	-4.22	5.94	4.61	2.98
7	0.00	0.00	0.00	0.00	1.37	4.61	11.94	-4.22
8	0.00	0.00	0.00	0.00	4.16	2.98	-4.22	12.71

Table 3.8. Effective Hamiltonian matrix for an asymmetric distortion (d(Cr-Cr) = 2.28-2.38 Å) around the $Cr_3(dpa)_4(CN)_2$ structure. All elements are given in eV.

CSFs	1	2	3	4	5	6	7	8
1	0.00	3.84	-3.38	4.58	-0.46	-0.55	0.54	0.50
2	3.84	10.45	0.03	-5.10	-1.38	-1.31	1.02	1.06
3	-3.38	0.03	11.63	1.18	0.63	1.10	-0.62	-0.63
4	4.58	-5.10	1.18	14.18	0.50	0.53	-0.79	-0.87
5	-0.46	-1.38	0.63	0.50	5.16	-4.01	1.12	3.94
6	-0.55	-1.31	1.10	0.53	-4.01	6.34	4.41	2.92
7	0.54	1.02	-0.62	-0.79	1.12	4.41	12.35	-4.00
8	0.50	1.06	-0.63	-0.87	3.94	2.92	-4.00	13.35

Table 3.9. Effective Hamiltonian matrix for the symmetric $Cr_3(dpa)_4(NO_3)_2$ structure (d(Cr-Cr) = 2.33 Å). All elements are given in eV.

CSFs	1	2	3	4	5	6	7	8
1	0.00	-4.33	3.29	4.60	0.00	0.00	0.00	0.00
2	-4.33	10.65	-0.17	5.15	0.00	0.00	0.00	0.00
3	3.29	-0.17	11.35	-1.82	0.00	0.00	0.00	0.00
4	4.60	5.15	-1.82	13.42	0.00	0.00	0.00	0.00
5	0.00	0.00	0.00	0.00	5.20	4.30	-1.56	4.28
6	0.00	0.00	0.00	0.00	4.30	5.65	4.62	-2.76
7	0.00	0.00	0.00	0.00	-1.56	4.62	12.02	4.30
8	0.00	0.00	0.00	0.00	4.28	-2.76	4.30	12.17

Table 3.10. Effective Hamiltonian matrix for an asymmetric distortion (d(Cr-Cr) = 2.28-2.38 Å) around the $Cr_3(dpa)_4(NO_3)_2$ structure. All elements are given in eV.

CSFs	1	2	3	4	5	6	7	8
1	0.00	-4.16	3.32	4.58	0.28	-0.37	0.34	-0.32
2	-4.16	10.66	-0.11	5.13	-0.86	0.85	-0.64	0.73
3	3.32	-0.11	11.52	-1.61	0.39	-0.72	0.36	-0.39
4	4.58	5.13	-1.61	13.86	-0.32	0.33	-0.47	0.58
5	0.28	-0.86	0.39	-0.32	5.26	4.19	-1.38	4.16
6	-0.37	0.85	-0.72	0.33	4.19	5.90	4.55	-2.77
7	0.34	-0.64	0.36	-0.47	-1.38	4.55	12.32	4.19
8	-0.32	0.73	-0.39	0.58	4.16	-2.77	4.19	12.69

The Potential Energy Surface of Trichromium EMACs

Chapter 4

Ab initio Molecular Dynamics on Trichromium EMACs

4.1 Introduction

In the previous chapter we presented the landscape of the Potential Energy Surface (PES) of three EMACs (Figure 4.1), generated by a collection of single point CASSCF/CASPT2 calculations. The results depict an extremely flat PES and a symmetric global minimum for $Cr_3(dpa)_4(NCS)_2$. The disagreement with experiment could be attributed to the single molecule nature of the calculation, which lacks the packing effects of the crystal. However, ultimately the EMACs will be used in a device configuration with (presumably) no intermolecular interactions, which resembles more the gas phase than a crystal environment. In addition, such devices might be used at a finite temperature. Given the flatness of the PES of such molecules, any thermal energy could result in a collection of accessible structures averaging relevant properties.

In this sense, the previous static picture does not reveal the effects of temperature in the structural flexibility of the chromium chains. In this chapter, we account for this effect by performing ab initio molecular dynamics to explore the PES of the aforementioned compounds. This is a computationally demanding task,

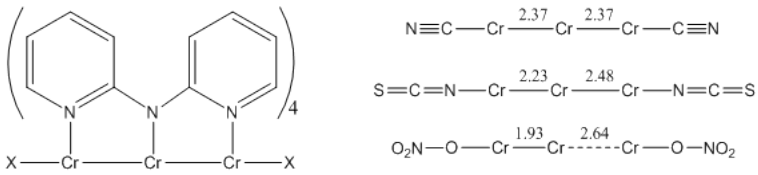

Figure 4.1. Schematic representation of trichromium EMACs (left) and experimental Cr-Cr distances (Å) for the different axial ligands (X = CN, NCS and NO_3, right).

which escapes the reach of what Multiconfigurational methods can do. As of today, CASSCF/CASPT2 molecular dynamics are not possible for the active space and size of these systems. The alternative is DFT, which we previously criticized as it showed a bias towards symmetric structures. Nevertheless, the results of DFT were comparable to CASPT2 for the global minima in two of the three examples, and in the case of $Cr_3(dpa)_4(CN)_2$ both methods depicted a similar shape for the PES. We accept that DFT might not be the most accurate method, but in this task it can provide valuable information at a reasonable computational cost.

Finally, we include a study of the crystalline phase of the three compounds, to shed some light on the importance of the packing effects on these compounds. For extended systems, DFT has been the method of choice for most of the latest studies, and in our case it provides the means to compare with the gas phase results in an equal footing.

4.2 Computational Information

Single molecule ab initio molecular dynamics have been performed using the Car-Parrinello approach in CPMD 3.15 [42] DFT/BLYP[24, 26]. was used with the corresponding Trouiller-Martins normconserving pseudo-potentials and a cutoff of 90 Ry. Standard isotope mass were used for all the atoms except for H, which was replaced by deuterium in order to increase the time step in the dynamics (4.0 a.u. = 0.0968 fs). An orthorhombic box of dimensions 25.0 x 15.0 x 15.0 (Å) was used after a series of tests, to avoid any interactions between the periodic replica. NVT with Nosé-Hoover thermostat was used with frequencies of 2100 and 10000 cm^{-1} for

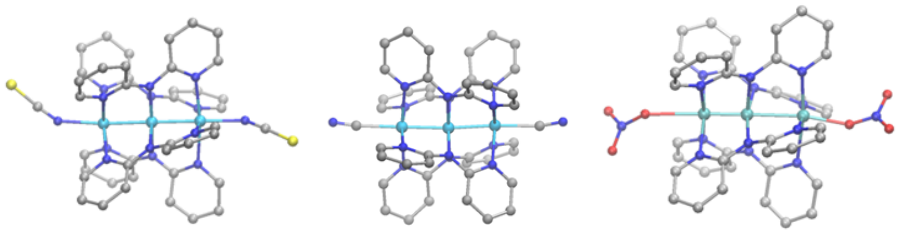

Figure 4.2. Structures of $Cr_3(dpa)_4(NCS)_2$ (left), $Cr_3(dpa)_4(CN)_2$ (left) and $Cr_3(dpa)_4(NO_3)_2$ (right). Color code: Cr (teal), N (blue), C (grey), S (yellow) and H omitted for clarity.

ions and electrons, respectively. A fictitious electron mass of 600 a.u. was used for all the molecules, whereas the fictitious electron kinetic energy was obtained from a preliminary annealing process. For the 300 K run, the values were 0.01810, 0.01739, 0.01909 a.u. for NCS, NO_3 and CN, respectively. Ab initio molecular dynamics were carried out upon experimental crystal cells with VASP 5.3 code [43–47]. The projector-augmented-wave (PAW) formalism [48] and plane waves of 400 eV cutoff were used, with the DFT/PBE [25] method. A timestep of 0.1000 fs was used at 300 K for a canonical ensemble using the algorithm of Nosé, with a frequency of temperature oscillations given by a Nosé mass of $0.438x10^{-27}$, $0.404x10^{-27}$ and $0.187x10^{-27}$ a.u. for NCS, NO_3 and CN, respectively.

4.3 Gas Phase Results

In this section, we discuss the results of the molecular dynamics simulations of the three chromium EMACs as isolated species (Figure 4.2). Previous calculations of the potential energy surface (PES), expanded from the two Cr-Cr distances, showed in all cases relative flat energy landscapes. These results suggest that, given a certain amount of thermal energy, the central Cr can move freely, creating several structures that are known to have different relevant properties. The example that motivated this work is the difference in conductance between isomers of $Cr_3(dpa)_4(NCS)_2$ that differ only in the arrangement of the Cr chain. Under this hypothesis, a device configuration constructed with molecules of $Cr_3(dpa)_4(NCS)_2$ would measure the average conductance of a collection of structures that could easily fluctuate by the

accessible thermal energy in the experiment. Gas phase simulations are a good approximation of a device configuration, where there are no interactions between molecules, and can be used to understand the conductance properties of these and similar materials to be used in new nano-devices.

The evolution of the two Cr-Cr distances in $Cr_3(dpa)_4(NCS)_2$ during the molecular dynamics can be seen in Figure 4.3. Along the simulation, the two distances (represented by red and blue lines) oscillate between two distinct regions. Most of the time (90%), the Cr-Cr distances appear close to a value of 2.3 $\pm$0.1 Å, but in some cases the distances are elongated to 2.5-2.6 Å. In addition, this elongation is alternated between the two Cr-Cr distances in what appears to be a collective movement of the Cr_3 backbone. In most cases, when one distance increases, the other one remain in the shorter region (around 2.3 Å). This determines unsymmetrical structures where the difference between the two Cr-Cr distances ($\Delta dist$) is larger than 0.2 Å. Finally, this is represented in Figure 4.4, where a histogram of $\Delta dist$ is shown. We can distinguish one principal distribution around 0.0 Å, which indicates structures with two similar Cr-Cr distances. These structures ($|\Delta dist| < 0.15$ Å) represent more than 70% of the total and the average Cr-Cr distance is 2.35 Å. However, there is non-negligible number of unsymmetrical structures ($|\Delta dist| > 0.20$ Å) that can be observed in a minor distribution around $\pm$0.30 Å. The proportion of unsymmetrical structures diminishes (to less than 1%) when the temperature decreases to 50 K (blue set in Figure 4.4), confirming the effect of the thermal energy.

The simulation of $Cr_3(dpa)_4(CN)_2$ (Figure 4.5) presents similar results. In this case, 60% of the total structures are symmetric ($|\Delta dist| < 0.15$ Å) and the average Cr-Cr distance is 2.38 Å, in agreement with previous static DFT calculations and experimental results. The similarities between NCS and CN are consistent with previous results that suggest both structures to be symmetrical, with a really flat PES. These two ligands have a relatively strong sigma donor character compared to NO_3, which is labeled as a weak donor ligand. The latter favors an unsymmetrical arrangement of the Cr chain and it should be no surprise to obtain two distinct Cr–Cr distances during the molecular dynamics (Figure 4.6). The oscillations are much smaller than in the previous cases, and the average values (1.95 and 2.62 Å) are in very good agreement with the experimental structure (1.93 and 2.64 Å). However, it must be noted that the DFT calculations reported in the previous chapter yielded

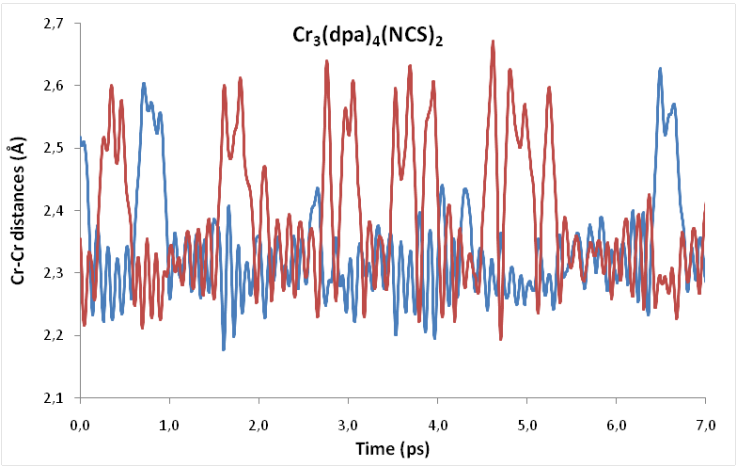

Figure 4.3. Chromium distances from the molecular dynamics of $Cr_3(dpa)_4(NCS)_2$.

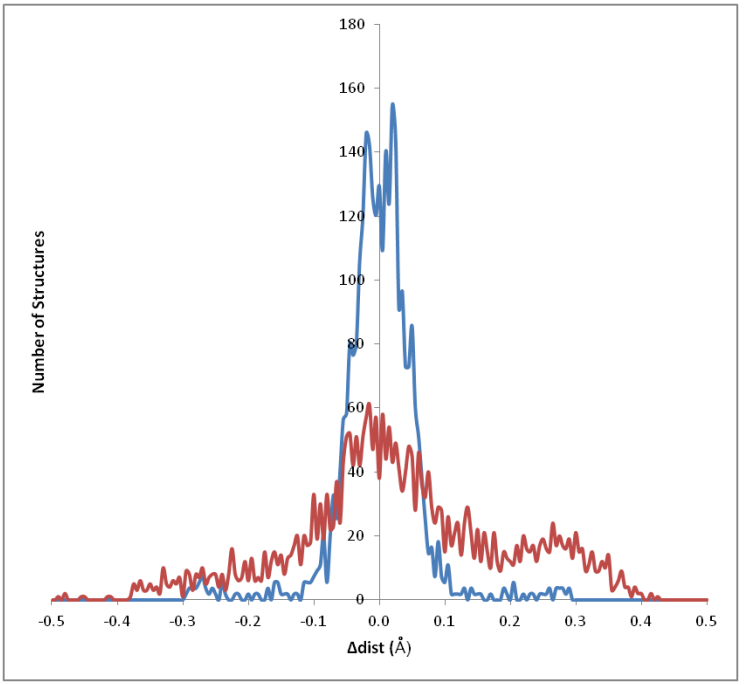

Figure 4.4. Histograms of the difference between Cr-Cr distances ($\Delta dist$ in Å) for $Cr_3(dpa)_4(NCS)_2$ at two different temperatures: 300 K (red) and 50 K (blue).

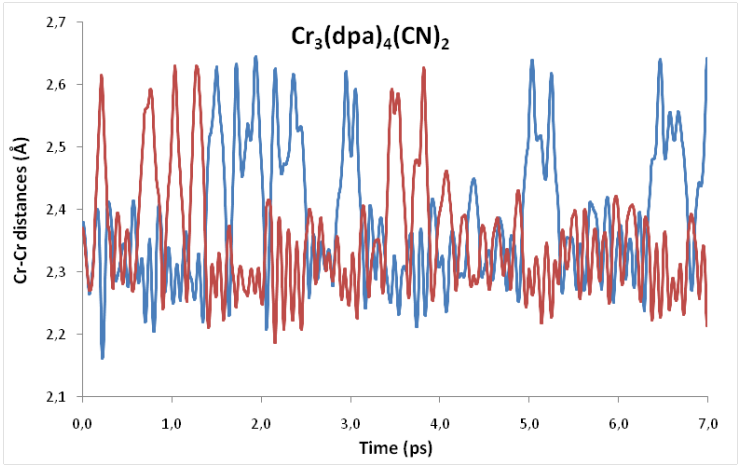

Figure 4.5. Chromium distances from the molecular dynamics of $Cr_3(dpa)_4(CN)_2$.

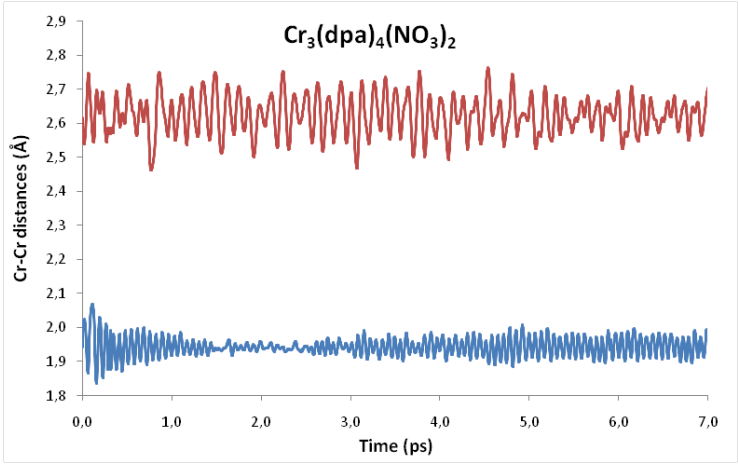

Figure 4.6. Chromium distances from the molecular dynamics of $Cr_3(dpa)_4(NO_3)_2$.

structures with symmetrical Cr-Cr chains. There are a few possible explanations for these discrepancies in the DFT results. It is not our goal to focus on this point, but we can mention there is a difference in the orientation of the NO_3^- ligands, which are usually aligned with respect to the Cr_3 chain but in this case appear distorted (Figure 4.2). This could be related to the absence of symmetry along the Cr_3 chain and/or by the constraints imposed by the replicated cell in the calculation. However, both cases have been investigated and ruled out. Other differences such as basis set and pseudopotentials could be responsible for favoring the asymmetric structure in the MD calculations but are more difficult to check.

4.4 Crystalline Phase Results

In this section we present the results of the molecular dynamics simulations in the crystal cell for the three compounds. Figure 4.7 shows the chromium-chromium distances for part of the run for the NO_3 system. In this case, there are eight unique distances reported because the unit cell contains four EMAC molecules. It can be seen that there are two clearly different sets of distances, one group of four oscillate around 2.6 Å, whereas the other do the same at 1.8 Å. This behavior is the same observed for the gas phase dynamics of NO_3, which indicates that the constrains of the packing effects plays little to no role for this molecule. Finally, it is worth mentioning that the average structure is in good agreement with the experimental data (1.93, 2.64 Å). The case of CN, represented in Figure 4.8, features four unique Cr-Cr distances, from the two EMAC molecules in the unit cell. During most of the simulation time, the distances oscillate around 1.8 and 2.6 Å, similar to the NO_3 case. However, there are a few instances where the distances come close to 2.3 Å and a symmetric structure is observed. Compared to the gas phase results at the same temperature (300 K), which feature predominant symmetric structures, the EMAC structures in the unit cell are mainly asymmetric, indicating a possible packing or neighboring effect to explain this difference.

Lastly, Figure 4.9 shows the results for $Cr_3(dpa)_4(NCS)_2$ in the solid unit cell. The results are similar to the CN case, observing asymmetric structures along the simulation with average distances of 1.7 and 2.6 Å. The unit cell of the solid consist of

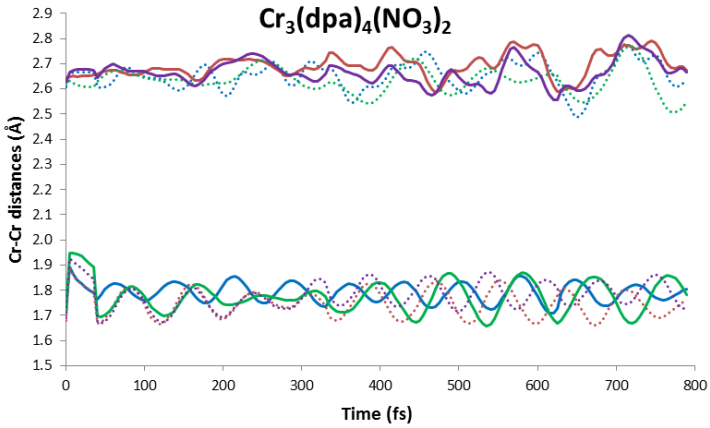

Figure 4.7. Chromium distances from the molecular dynamics of $Cr_3(dpa)_4(NO_3)_2$ in the crystalline phase.

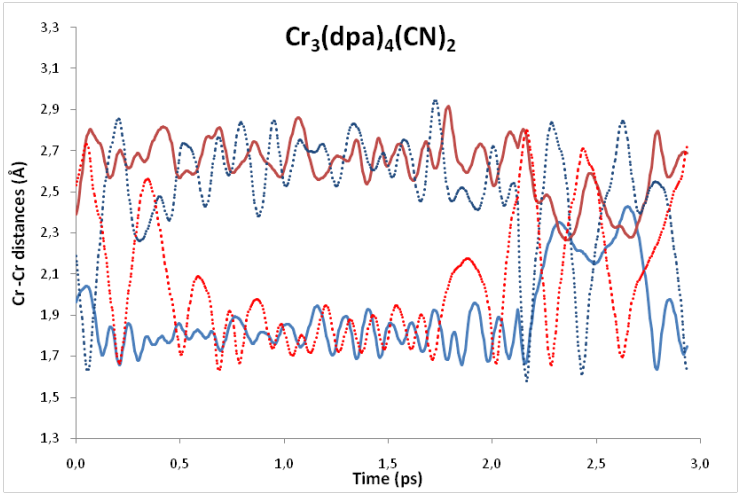

Figure 4.8. Chromium distances from the molecular dynamics of $Cr_3(dpa)_4(CN)_2$ in the crystalline phase.

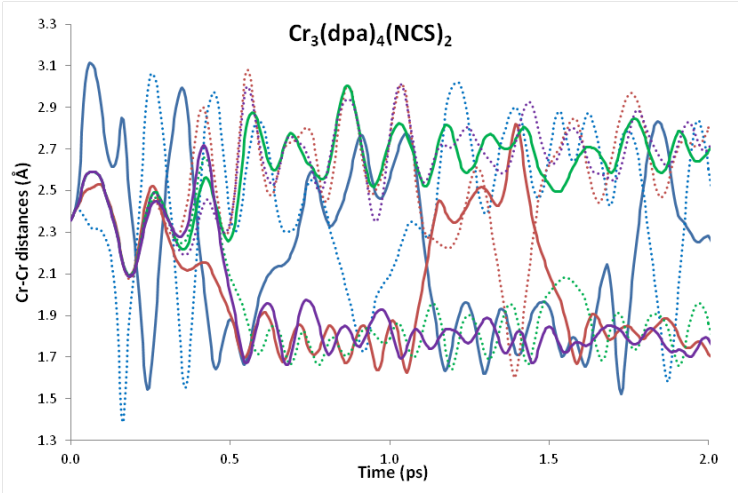

Figure 4.9. Chromium distances from the molecular dynamics of $Cr_3(dpa)_4(NCS)_2$ in the crystalline phase.

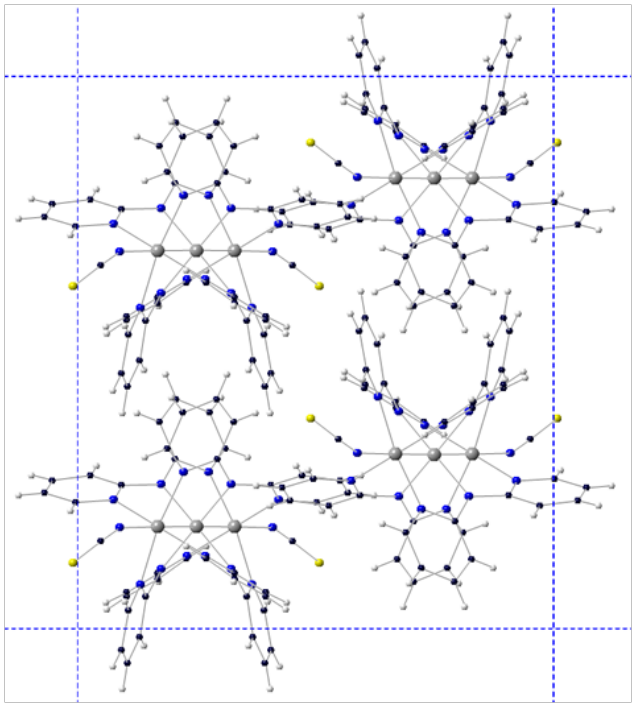

Figure 4.10. Unit cell of the $Cr_3(dpa)_4(NCS)_2$ view along the c axis.

four EMAC molecules and a side view of the cell (Figure 4.10) shows the interaction between molecules resulting in the torsion of the NCS ligand with respect to the Cr chain. This distortion that appeared occasionally in the gas phase simulation, is constant in the solid simulation.

4.5 Concluding remarks

We have used molecular dynamic simulations to show the effect of thermal energy on the structural flexibility of chromium EMACs. We observed the different behavior of the axial ligands. In both phases, the weak sigma donor NO_3 present asymmetric structures with Cr–Cr distances that are in agreement with the experimental values. NCS and CN, having a stronger sigma donor character, present a mixture of symmetric and asymmetric structures along the molecular dynamics. In the gas phase, where there is no interactions between molecules, both compounds favor symmetric structures. In the solid state, the packing effects and neighbor interaction favor asymmetric structures. This interaction appears evident in the torsion of the axial ligand with respect to the chromium chain axis.

In sum, thermal effects should be taken into account when working with flexible materials such as chromium EMACs. Solid packing and neighboring effects appear to be important in molecules with very flat PES, i. e. axial donor of intermediate strength, to tip the scale in favor of asymmetric chains.

Chapter 5

Metal–Metal Bonding in chromium compounds

5.1 Introduction

The study of the metal–metal interactions in transition metal complexes has been a topic of interest among the inorganic and physical chemistry community. From multiple bonds to non-covalent magnetic interactions, the problem can be formulated in terms of one electron functions (orbitals) and the electron count of the bimetallic species. A high count of nd electrons (Ni, Cu) creates no formal bond but an (antiferro)magnetic interaction between the metals. On the other hand, partially filled nd shells (Cr, Co) translates into occupied orbitals of bonding character in the metal chain and formal metal-metal bonds. In all cases, the accurate treatment of electron correlation, both static and dynamic, is required. The most notorious example is the chromium dimer, Cr_2, which even to this date is a typical prototype molecule to test new methods [49–52].

The ligated chromium dimer Cr_2L_n has been studied extensively as well. It is well established that compounds with tetra-bridging ligands (Cr_2L_4) exhibit short Cr–Cr distances (1.7 - 2.0 Å) [53]. The axial coordination of donor ligands (X) to Cr_2L_4 leads to elongation of the Cr–Cr distance, and values of 2.2 to 2.7 Å have been

documented in a variety of $Cr_2L_4X_2$ complexes [54]. Several theoretical studies have focused on the bonding trends of Cr_2L_4 for different L, as well as varying the charge of the metal ions. Neutral Cr(0) species are characterized by the shortest Cr-Cr distances (around 1.7 Å) and the bond has been identified to be of quintuple nature based on the observation that the $\sigma^2\pi^4\delta^4$ configuration dominates the electronic structure [55, 56]. On the other hand, compounds that present Cr(II) ions exhibit a more elongated Cr–Cr bond, a dominant $\sigma^2\pi^4\delta^2$ configuration and bonding is more compatible with a quadruple bond [57]. The studies of $Cr_2L_4X_2$ compounds with Cr(II) ions are less numerous. Multiconfigurational Self-consistent Field (MCSCF) methods were previously used for model systems [58–60] but recent bonding analysis has been limited to DFT based methods like natural bond order (NBO) or extended transition state natural orbital for chemical valence (ETS-NOCV) [61].

EMACs offer the opportunity to study multimetallic complexes, with various degrees of metal-metal interactions. In chromium EMACs, the Cr_2 unit is part of a larger structure, coupled with at least one other transition metal (M). In such cases, the Cr–Cr distance varies from short to long depending on the identity of M and the axial ligand X. The most challenging cases are the Cr_3 compounds, which are strongly influenced by the axial ligands. In chapter 3, we used multiconfigurational methods to find structural tendencies in the Cr_3 compounds. The results confirmed an extremely flat potential energy surface for the Cr–Cr distances, indicating that for intermediate donor strength both symmetric and asymmetric forms can be encountered. The preferred conformation will depend on the subtle environment effects such as temperature, crystal packing or electrode surface clamping. This was confirmed in chapter 4, where ab initio molecular dynamics simulations indicated that thermal energy and crystal packing effects play an important role.

In this chapter we continue the study of the electronic structure of chromium EMACs, focusing on the metal–metal bonding multiplicity and their symmetry (σ, δ and π) contributions. The analysis of the wave function with the effective bond order (EBO)[56] procedure permits to quantify the effect of geometry distortion and changes in the axial ligand on the bond character.

Our analysis starts with dichromium species $Cr_2(O_2CCH_3)_4$ (**1**) and $Cr_2(O_2CCH_3)_4(H_2O)_2$ (**2**). These molecules feature short (1.966 Å) and long (2.362

Å) Cr–Cr distances, respectively, and can be used as simple models to understand the effect of the axial ligand on the wavefunction. Then, we study $Cr_2(dpa)_4$ (**3**),[62] precursor in the synthesis of many chromium EMACs. Paired with a transition metal complex, Cr_2M chains can be formed, which resemble a Cr_2^{4+} dimer with a penta coordinated non-interacting M^{2+}. We analyze different Cr_2M EMACs (M = Mn, Fe, Ni, Zn) with Cl as the axial ligand.[63–65] Finally, we explore the Cr_3 compounds with various axial ligands (X = Cl, NCS, CN, NO_3).[39]

5.2 Computational Details

Given the large number of unpaired electrons of the Cr(II) d^4 ion, a substantial multiconfigurational (MC) character can be expected for the all the compounds. In this sense, we used the complete active space self-consistent field (CASSCF) approach to obtain reliable wave function and natural orbitals. For the systems with only two Cr atoms, the active space contains eight electrons and eight orbitals, CAS(8,8). For the Cr_2M systems, the active space includes also M-3d orbitals that hold unpaired electrons. The ground state of the Cr_2 systems is a singlet. In the case of Cr_2M, the ground state multiplicity is given by the spin moment of the quasi-octahedral M(II) ion. Table 5.1 summarizes the active space and ground state spin multiplicity for the different Cr_2M systems.

Single point CASSCF calculations were performed in MOLCAS 8.0 package [66]. Atomic natural orbitals optimized for relativistic corrections and core correlation (ANO–RCC) basis sets of TZP level for the metals (DZP for the other atoms) were used to expand the orbitals [36]. Scalar relativistic effects were included using the Douglas–Kroll–Hess Hamiltonian. The computational costs from the two-electron integrals were reduced by the Cholesky decomposition technique (threshold was set to 10^{-8} a.u.) [37].

All the calculations were done on experimental structures obtained from the cited references. In addition, for each system, one structure with a fixed Cr–Cr distance was prepared by a restricted geometry optimization with DFT. These "forced" structures are very useful for the analysis of the Cr-Cr bond. The ADF program [67–69] was used for the geometry optimizations, using the BLYP functional with TZP basis for Cr and M and DZP for the rest of the atoms (H, C, N, O, Cl).

Table 5.1. Ground state spin multiplicity (S) and active spaces for the Cr_2M systems studied.

M(II)	d^n	**S**	**Active Space**$^{(a)}$
Zn	d^{10}	S=0	CAS(8,8)
Ni	d^8	S=1	CAS(10,10)
Fe	d^6	S=2	CAS(14,13)
Mn	d^5	S=5/2	CAS(13,13)
Cr	d^4	S=2	CAS(12,12)

(a) CAS(n, m) identifies an active space with n electrons and m orbitals

5.3 Bonding Analysis on Cr_2X_4 and $Cr_2X_4L_2$

The tetra-acetate bridged chromium dimer $Cr_2(O_2CCH_3)_4$ (**1**) has a short Cr-Cr distance of 1.97 Å. Figure 5.1 shows the molecular orbitals and natural occupation numbers obtained in the CASSCF(8,8) calculation. Using the natural orbital occupation numbers, we obtained a total EBO of 1.94 units (Table 5.2). The EBO decomposition in σ, δ and π show that the bond is composed of a nearly single σ bond and two slightly weaker contributions of the π_x and π_y manifold. The δ orbitals do not participate in the Cr-Cr bond.

In the hydrated complex, $Cr_2(O_2CCH_3)_4(H_2O)_2$ (**2**), the Cr-Cr distance elongates to 2.36 Å, and the EBO decreases to 0.87 units. The weaker overlap between the orbitals affects significantly the π contributions to the bond, but also the σ bond is weakened. In the first compound, the Cr atoms made a multiple Cr-Cr bond to share electron density. Once the axial ligand (H_2O) is present, it donates electron density towards the Cr atoms by Cr-X bonding, reducing the charge in the Cr as shown by the Mulliken analysis. In our calculations, the Cr-Cr bond order is reduced in one unit, from 2 to 1. We also calculated the EBO for the hydrated complex at a Cr-Cr distance of 1.97 Å(**2***). Even though the active space does not include H_2O orbitals, the effect of the ligand can be seen in the small differences in the occupation numbers and EBO values compared with the H_2O-free compound. Here we can compare the EBO values with the natural bond order (NBO) analysis which has higher values overall, but fails to distinguish between the two $Cr_2(O_2CCH_3)_4(H_2O)_2$ structures

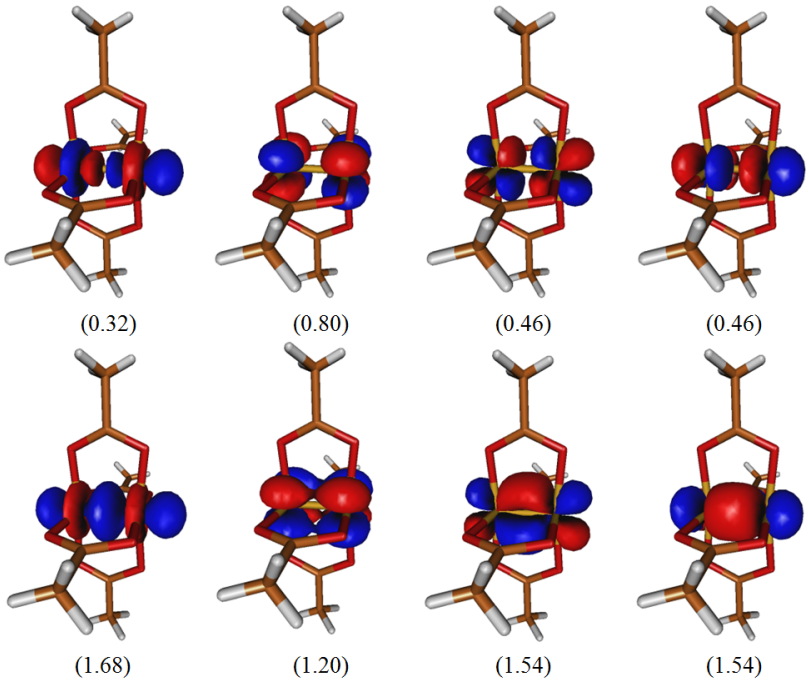

Figure 5.1. CASSCF(8,8) molecular orbitals and natural occupation numbers for $Cr_2(O_2CCH_3)_4$. Symmetry of the orbitals: σ, δ, π_x and π_y from left to right. Bonding (bottom) and anti-bonding (top) character.

Table 5.2. CASSCF(8,8) natural orbital occupation numbers and EBO for a collection of Cr_2 systems. We present the Mulliken Cr charge and the LoProp based NBO analysis.

	1	**2**	**2***	**3**	**3***	**4**
d(Cr-Cr) Å	**1.97**	**2.36**	**1.97**	**1.94**	**2.30**	**2.30**
σ	1.67	1.43	1.68	1.69	1.49	1.47
π	3.08	2.33	3.12	3.20	2.47	2.44
δ	1.19	1.05	1.21	1.25	1.06	1.18
σ^*	0.32	0.56	0.32	0.31	0.51	0.53
π^*	0.91	1.66	0.87	0.80	1.58	1.56
δ^*	0.80	0.94	0.79	0.75	0.94	0.82
EBO σ	0.67	0.43	0.68	0.69	0.49	0.47
EBO π	1.08	0.33	1.12	1.20	0.45	0.44
EBO δ	0.19	0.11	0.20	0.25	0.06	0.18
Total EBO	1.94	0.87	2.00	2.14	1.00	1.09
Cr charge	0.865	0.818	0.672	0.705	0.799	-
NBO	2.384	1.796	1.759	2.450	-	-

(**2** and **2***). Our results are in agreement with previous GMO-CI calculations on $Cr_2(O_2CH)_4$ (**4**), presented in Table 5.2. Finally, the case of $Cr_2(dpa)_4$ (**3** and **3***) follows the same trends of the acetate, regarding the short and long distances EBO (2 and 1 respectively).

Table 5.3. CASSCF(m,n) natural orbital occupation numbers and EBO for Cr_2M systems.

	Cr_2Zn		**Cr_2Ni**		**Cr_2Fe**		**Cr_2Mn**	
d(Cr-Cr) Å	**2.00**	**2.30**	**2.03**	**2.30**	**2.02**	**2.30**	**2.04**	**2.30**
d(Cr-M) Å	**2.78**	**2.74**	**2.58**	**2.47**	**2.71**	**2.57**	**2.78**	**2.57**
σ	1.65	1.45	1.63	1.46	1.64	1.46	1.64	1.51
π	3.02	2.40	2.92	2.40	2.95	2.40	2.92	2.44
δ	1.12	1.04	1.11	1.04	1.11	1.04	1.11	1.05
σ^*	0.34	0.55	0.37	0.54	0.36	0.54	0.36	0.49
π^*	0.98	1.60	1.08	1.60	1.04	1.60	1.08	1.56
δ^*	0.88	0.96	0.89	0.96	0.89	0.96	0.89	0.95
EBO σ	0.66	0.45	0.63	0.46	0.64	0.46	0.64	0.51
EBO π	1.02	0.40	0.92	0.40	0.96	0.40	0.92	0.44
EBO δ	0.12	0.04	0.11	0.04	0.11	0.04	0.11	0.05
Total EBO	1.80	0.89	1.66	0.90	1.71	0.90	1.67	1.00

5.4 Metal bonding on Cr_2M EMACs

As mentioned before, $Cr_2(dpa)_4$ is the precursor in the experimental synthesis of several Cr_2M EMACs. In our work, we followed the trend in the Cr-Cr bond by studying these systems. We used the experimental structures of $Cr_2M(dpa)_4Cl_2$ (M=Zn, Ni, Fe, Mn) to calculate natural orbital occupation numbers and EBO values. The active space of the Zn case contained 8 electrons and 8 orbitals from the Cr_2 unit, due to Zn(II) being diamagnetic (d^{10}). The compounds where M(II) had unpaired electrons required an extension of the active space. We took into account the high spin configuration of the octahedral M ion and extensive testing, in order to find the proper active spaces. The active space and ground state multiplicities are shown in Table 5.1. It is worth mentioning that in the cases where M orbitals were added to the active space, the molecular orbitals presented almost no mixture between the Cr_2 and M units, which made the EBO analysis straightforward.

In addition to the experimental structures, we analyzed DFT optimized structures with fixed Cr-Cr equal to 2.30 Å. Table 5.3 shows the Effective Bond Orders for the Cr-Cr unit in Cr_2M and the trend is in agreement with previous Cr_2 results.

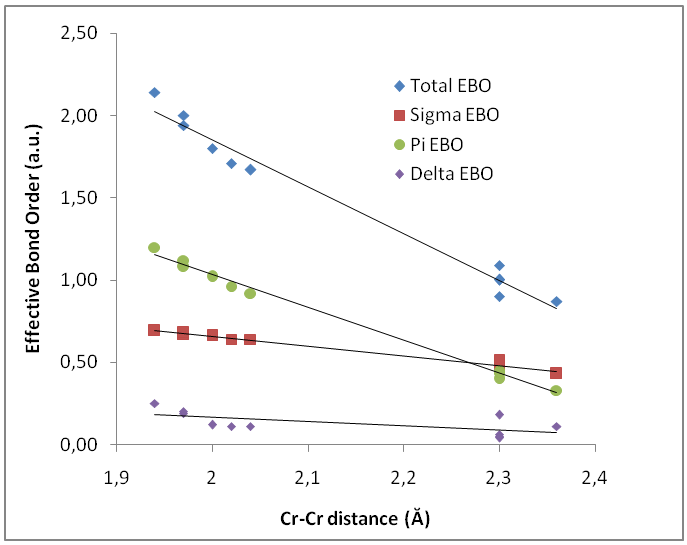

Figure 5.2. Effective Bond Order (a.u.) as a function of the Cr-Cr distance (Å) for the Cr_2 and Cr_2M combined.

This indicates that for these systems there is no interaction between Cr_2 and M, as expected from the long distance. If we combine the calculated EBOs from all the systems studied so far, and analyze the relationship with the Cr-Cr distance we can see the clear trends. Figure 5.2 shows that the EBO decreases with the Cr-Cr distance, an expected trend since it is a measure of the bonding between two atoms. Moreover, we observe the different components of the EBO have different slopes. At smaller distances π dominates over σ due to the fact that there are twice as many orbitals (π_x and π_y), but the bonding contributions decay at a different rate due to different overlap of the orbitals. The σ orbitals are more resilient than the π ones, that is, their overlap is not that dependent on the Cr-Cr distance.

So far the EBO has been helpful to analyze the Cr-Cr bond, due to the localized nature of the molecular orbitals. Any case that present delocalized CASSCF molecular orbitals along the whole Cr_2M chain would in principle make the analysis more complicated. In that scenario, the EBO would reflect the total bonding of the chain, relevant if we were in the presence of a system with a predominant 3-center bond. However, localization techniques, which consist of unitary transformation of the natural orbitals, can be used to create a new set of orbitals where the bonding and non-bonding orbitals are localized either on the left or the right pair of atoms

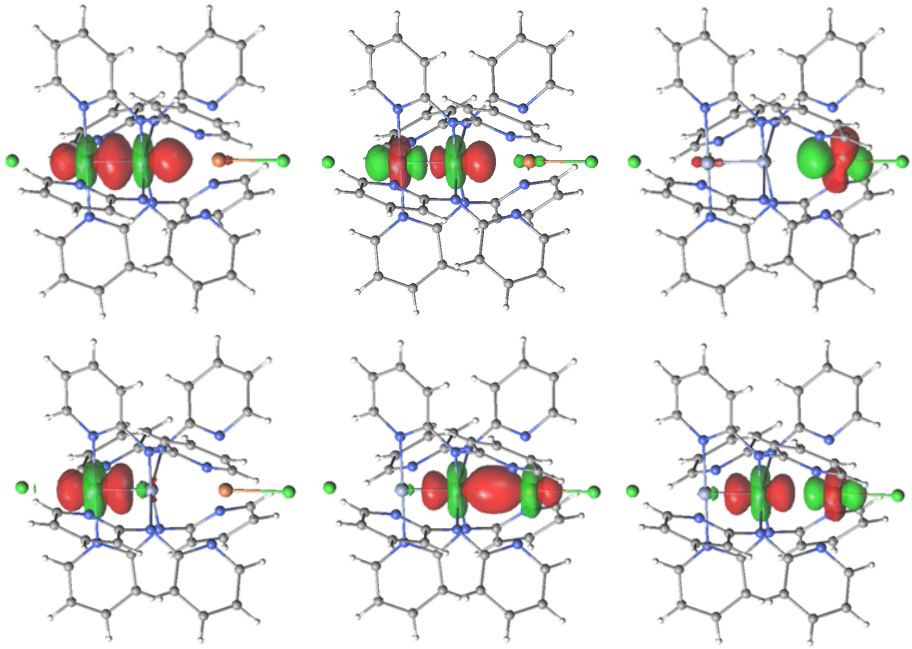

Figure 5.3. Sigma molecular orbitals for Cr_2Fe experimental structure (2.02 Å). Natural (top) and CrFe localized (bottom) orbitals.

of the chain. As an example, we used this technique in the Cr_2Fe case, to obtain bonding and anti-bonding molecular orbitals localized on the CrFe unit (Figure 5.3). The bond order analysis for this new set of molecular orbitals showed an EBO close to 0, which is expected since there was no interaction between Cr and Fe. Nevertheless, this presents an opportunity to study more complicated systems like Cr_3 EMACs, where the bonding is more delocalized along the 3 centers, and obtain specific contributions to the total bond from each significant Cr-Cr pair.

5.5 Metal bonding on Cr_3 EMACs

In this section we analyze the Cr-Cr bond of trimetallic Chromium chains. The general formula $Cr_3(dpa)_4X_2$ suggests two equivalent terminal Cr atoms. As such, both Cr-Cr bonds are expected to be equal and the chain symmetric. However, it is accepted that weak sigma donor ligands (X) influence the Cr_3 chain, favoring

asymmetrical structures. This is the case of NO_3, which has been characterized experimentally with short and long (1.93 and 2.64 Å) Cr-Cr distances. In chapter 3 we have shown an asymmetric minimum (1.95 and 2.64 Å) and the localized nature of the molecular orbitals in the short Cr-Cr pair. Table 5.4 presents the natural occupation numbers and the EBO for the Cr_3 compounds. NO_3^- values are in agreement with previous Cr_2M as well as $Cr_2(dpa)_4$. On the other hand, CN^- strong sigma donor character favors symmetrical structures and has been characterized with one Cr-Cr distance of 2.37 Å. Our CASSCF/CASPT2 calculations featured a symmetric minimum in good agreement with the experiment (2.42 Å). For this symmetrical chains, the molecular orbitals appear delocalized with contributions from the three Cr-3d atomic orbitals. In this case, the values reported in Table 5.4 correspond to these delocalized orbitals, the EBO value close to 1 (0.93) indicating a single bond shared between the 3 centers. This is an example of a 3-center 2-electron bond, a term adopted from the organic chemistry literature. In between the two previous cases, Cl and NCS appear. Characterized as intermediate structures, they present two close distances (2.23 and 2.48 Å). The molecular orbitals are delocalized in the whole chain and the occupation numbers and EBO values are close to the CN case. For the NCS, we present the results for the structure that had the minimum energy at CASSCF/CASPT2 level: a symmetrical chain with Cr-Cr distances of 2.33 Å that shows comparable EBO values with the experimental structure.

At this point, we make use of localization techniques to obtain molecular orbitals with contributions from specific atomic Cr-3d orbitals and then calculate the occupation numbers and effective bond order for each case. For the NCS, we worked with symmetric (2.33 Å), experimental (2.23-2.48 Å) and highly asymmetric (1.93-2.64 Å) structures to obtain molecular orbitals localized on the Cr-Cr pairs of each side of the chain. Table 5.5 shows the results of the occupation numbers and EBO for each highlighted Cr-Cr pair. Starting with the symmetric chain, both localizations (left, right) produce equal results, a total EBO of 0.61 for the Cr-Cr bond with important contributions from the σ and π electrons. The original delocalized EBO for this structure was 0.99, and we should reiterate that the partial/localized EBO's cannot be add up to obtain the delocalized one, since in the former we are double counting the contributions from the central atom. What we can do with the partial EBO's is to quantify the relative strength of each (left, right) Cr-Cr bond. In the symmetric case this is trivial, since both distances are equal and therefore

Table 5.4. CASSCF(12,12) natural orbital occupation numbers and EBO for $Cr_3(dpa)_4X_2$ systems. Non-bonding orbitals are omitted.

	NO_3^-	Cl^-	NCS^-		CN^-
d(Cr_1-Cr_2) Å	**1.93**	**2.23**	**2.23**	**2.33**	**2.37**
d(Cr_2-Cr_3) Å	**2.64**	**2.48**	**2.48**	**2.33**	**2.37**
σ	1.69	1.52	1.52	1.51	1.50
π	3.20	2.48	2.50	2.44	2.39
δ	1.19	1.05	1.05	1.04	1.04
σ^*	0.31	0.48	0.48	0.49	0.50
π^*	0.80	1.52	1.50	1.56	1.61
δ^*	0.81	0.95	0.95	0.96	0.96
EBO σ	0.69	0.52	0.52	0.51	0.50
EBO π	1.20	0.48	0.50	0.44	0.39
EBO δ	0.19	0.05	0.05	0.04	0.04
Total EBO	2.08	1.05	1.07	0.99	0.93

Table 5.5. CASSCF(12,12) occupation numbers and EBO for localized orbitals of $Cr_3(dpa)_4(NCS)_2$. Non-bonding orbitals are omitted.

d(Cr_1-Cr_2) Å	**2.33**	**2.23**	2.23	**1.93**	1.93
d(Cr_2-Cr_3) Å	**2.33**	2.48	**2.48**	2.64	**2.64**
Localized pair Cr_i	1-2 / 2-3	1-2	2-3	1-2	2-3
σ	1.30	1.42	1.18	1.71	0.93
π	2.27	2.45	2.09	3.21	2.04
δ	1.03	1.04	1.01	1.19	1.03
σ^*	0.70	0.53	0.87	0.29	0.89
π^*	1.72	1.53	1.90	0.79	2.02
δ^*	0.97	0.95	0.98	0.81	0.94
EBO σ	0.30	0.42	0.16	0.71	0.02
EBO π	0.28	0.46	0.10	1.21	0.01
EBO δ	0.03	0.05	0.02	0.19	0.04
Total EBO	0.61	0.92	0.28	2.11	0.07

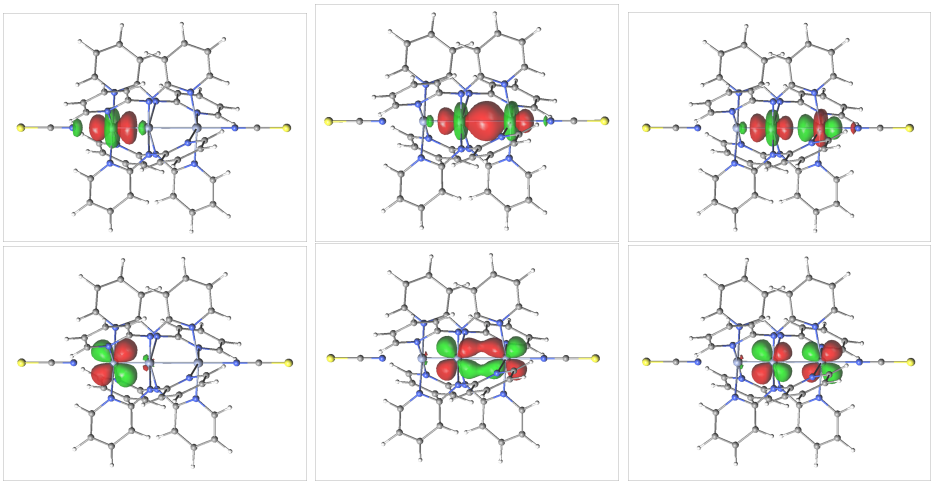

Figure 5.4. Long pair localized molecular orbitals for asymmetric NCS chain (1.93-2.64 Å). σ (top) and π_{xy} (bottom) orbitals.

their EBO and relative strength are equal. The left-right comparison have value in the case of non-symmetric chains, and for the experimental structure the difference between the short (2.23 Å) and long (2.48 Å) is already apparent. The former has a larger EBO (0.92 compared to 0.28) and the ratio short:long is larger than 3:1. That means that from the total bonding character of the delocalized chain, more than 75% comes from the short distance Cr-Cr pair. Finally, we show the results of an asymmetric chain, with the Cr-Cr distances of the experimental NO_3^- structure. In this case the natural orbitals were already localized on the short Cr-Cr pair, and the total EBO was similar to the NO_3^- experimental case. The localization of the long Cr-Cr pair (Figure 5.4) resulted in total EBO close to zero (0.07), as in the Cr_2Fe case. In sum, the three structures represent cases were the left:right bonds contributions range from 1:1 (symmetric, 50%), 3:1 (intermediate, 75%) to fully localized (asymmetric, 100%). Similar results were obtained for CN and NO_3 axial ligands.

5.6 Concluding remarks

In this chapter, we have used electronic structure calculations to investigate the metal-metal bonding character in Cr_2 and Cr_2M compounds. The Effective Bond Order (EBO) concept was used to observe trends in the bond multiplicity and the contributions from the different orbital symmetry (σ, δ and π). The Cr_2 EBO results show a linear tendency with respect to the metal-metal distance, with a total EBO that varies from 2.00 to 1.00. The most relevant contributions were from the σ and π manifolds, the latter having a larger dependence with the Cr-Cr distance. We have shown that even for medium distances (2.3 - 2.4 Å) the π bond contribution is not negligible and close to the σ one. The results for the Cr_2M compounds followed similar trends, where the total EBO comes almost exclusively from the contribution of the Cr_2 unit. Finally, we explored the $Cr_3(dpa)_4(X)_2$ structures showing the differences the axial ligands generate. CN^- and NCS^- ligands favor delocalized molecular orbitals where the EBO reflects the global bonding of the Cr-Cr-Cr chain. In such cases, we used localization techniques to quantify the contributions from each Cr-Cr pair. We compared the EBO for three structures with different asymmetric character and the results can quantify the relative contributions of each pair to the total bond. In future works, we will explore this methodology to study larger systems containing 5 to 7 metals.

Metal–Metal Bonding in chromium compounds

Chapter 6

Magnetism in Nickel bimetallic compounds and EMACs

6.1 Introduction

The calculation of accurate magnetic coupling constants has been a relevant theoretical problem for many years. The smallness of the energy differences and the antagonist physical effects involved in the interaction between spin moments make this a challenging topic for theoreticians. The difference dedicated configuration interaction (DDCI) method [70, 71] has been proven capable to produce coupling strengths in good agreement with the experimental findings for binuclear complexes and, more recently, also for polynuclear systems [72]. Due to the variational nature of the method, DDCI can be applied with a minimal complete active space configuration interaction (CASCI) reference wave function, which makes it easy to use and attractive from a conceptual point of view [73–75]. However, the high computational cost associated with DDCI calculations makes the method less suitable for systems with large ligands, many magnetic centers, or many unpaired electrons per magnetic center. Several variants of DDCI were developed in order to reduce the computational cost for such large systems, obtaining promising results [76–81].

A second family of methods commonly used in the calculation of magnetic couplings are those based on multiconfigurational reference perturbation theory (MRPT). Applied to second order (MC-PT2), these methods provide a computationally efficient alternative to DDCI extending the applicability range of the *ab initio* methods to larger systems. Although MC-PT2 gives in general a rather reasonable description, there are some points that need to be carefully addressed in order to extract relevant conclusions from the perturbative treatment of the magnetic coupling. In the first place, one should be aware of the possible appearance of intruder states, and special attention in the definition of $\hat{H}^{(0)}$ must be taken. Compared to DDCI, MC-PT2 results may show a strong dependence on the size of the active space, usually requiring the inclusion of ligand orbitals and a second set of magnetic orbitals in order to obtain quantitative results [82, 83]. Calculations based on a minimal active space reference wave function tend to underestimate the coupling strength by ∼60-80%.

In a recent study of binuclear copper complexes [84], the origin of the underestimation of magnetic coupling constants (J) in MC-PT2 methods with minimal active space has been identified. The bare CAS description generates less delocalized molecular orbitals compared to those obtained with DDCI [85], and the usage of natural DDCI orbitals for the perturbative treatment of the dynamic electron correlation greatly improves the calculated magnetic couplings. Such approach is of course not very efficient, but the authors propose a strategy to obtain a set of orbitals that maximally resembles the natural DDCI orbitals without going beyond the minimal active space. In the first part of this chapter, we extend the aforementioned strategy to test its applicability in binuclear nickel complexes, in an attempt to obtain a simple and computationally efficient scheme for the calculation of magnetic coupling constants based on a minimal active space in systems where DDCI cannot be applied anymore. The main purpose of this part is to give more evidence to the finding that the systematic underestimation of the J values in MCPT2 calculations finds its origin in the poor quality of the molecular orbitals obtained in a minimal CAS treatment of the electronic structure.

Better orbitals can be obtained in two ways, either by minimizing the CASSCF energy for an average of neutral and ionic states (topic of the first part of this chapter, see section 6.3) or in a more conventional approach by extending the active

space with ligand orbitals localized on the bridge between the magnetic centers. This second strategy has been applied many times before with reasonable success [86] but runs into problems for systems with many magnetic centers. Moreover, any MC-PT2 treatment becomes computationally more and more expensive when the number of atoms of the complex increases. Although the magnetic interactions of Ni(II) based EMACs have been treated some years ago within a standard CASPT2 approach [87], the Ni_3 EMAC required a lot of computational resources and it seems difficult to apply the standard approach for the Ni_5 or even longer Ni-based EMACs reported in the literature. Therefore, in the second part of this chapter (section 6.4) we focus our attention on a new method to combine the treatment of non-dynamic correlation through a multiconfigurational approach with a DFT based calculation of the dynamic correlation.

6.2 Computational Details

A simple yet accurate phenomenological Hamiltonian that accounts for the coupling between the local spin angular moments S_i and S_j was first introduced by Heisenberg as

$$\hat{H} = -J\hat{S}_i \cdot \hat{S}_j \tag{6.1}$$

where $\hat{S}_i$ is the total spin operator of site i and J parametrizes the coupling strength. Negative J-values correspond to antiferromagnetic coupling. In the complexes considered here, each Ni(II) ion has a triplet ground state, giving rise to quintet, triplet and singlet states when coupled to the other Ni(II) ion in the complex. The Heisenberg Hamiltonian predicts a regular energy spacing between these three states, known as the Landé pattern:

$$E(S-1) - E(S) = JS \tag{6.2}$$

To investigate the importance of the deviations to the Heisenberg Hamiltonian, we calculated J from the energy difference of singlet and triplet, and triplet and quintet

$$E(S=0) - E(S=1) = J \tag{6.3}$$

$$\frac{1}{2}\left(E(S=1) - E(S=2)\right) = J \tag{6.4}$$

When the two J values are equal the states follow the so called "Heisenberg behavior". Otherwise one should either extend the model Hamiltonian with biquadratic interactions terms [75, 88–90], or put doubts on the reliability of the computational scheme [83].

The orbital optimizations and CASPT2 calculations were performed using MOLCAS 7.8 [35]. The CASDI program [91, 92] was used to perform the DDCI calculations and the NEVPT2 results were obtained with the computer code developed at the University of Ferrara [93]. MCPDFT calculations were performed with the translated PBE variant in a developers version of MOLCAS 8.1 [66], from the University of Minnesota [94, 95]. Relativistic Atomic Natural Orbitals (ANO-RCC) basis sets were used, contracted to [2s] for H, [3s,2p] for C and N in external ligands, [3s,2p,1d] for O and bridging C and N, [4s,3p,1d] for Cl and S, and [5s,4p,3d] for Ni. The DDCI calculations are at the limit of what is still feasible, especially for the complexes with voluminous ligands. To reduce the number of inactive (virtual) MOs and consequently the size of the DDCI space, we apply the dedicated orbital transformation [76, 96] to order the MOs by decreasing importance for the energy differences [97]. The less important MOs were excluded from the generation of the CI expansion. To avoid any bias towards a particular spin state in the DDCI calculations, we used the iterative DDCI scheme [98]. The results are made independent of the starting orbital set by constructing average natural orbitals by diagonalizing the triplet-quintet average DDCI density matrix and perform a new DDCI step with the average orbitals. The process is iterated until the energy difference becomes constant, normally in three or four steps.

The original zeroth-order Hamiltonian [99] was used in CASPT2 because this choice has been shown to be more adequate for magnetic couplings than the present zeroth-order Hamiltonian [100] based on the $IPEA = 0.25$ Hartree parameter. The zeroth-order Hamiltonian of n-electron valence PT2 (NEVPT2) [101–104] is based on Dyall's model Hamiltonian [105], which contains all two-electron interactions among the active electrons. We have used both the strongly-contracted (SC) and partially-contracted (PC) variant of NEVPT2.

6.3 MC-PT2 in Ni_2 complexes with minimal active space

6.3.1 The State Average methodology

Binuclear copper complexes present two Cu(II) sites (d^9 configuration) with spin angular moments $S = \frac{1}{2}$. The minimal active space in that case contains two electrons in two orbitals CAS(2,2). In the cited study [84], instead of optimizing the orbitals for the ground state triplet or singlet (or an average of them), the reference wave function is obtained as a state average (SA) of two singlet states. The first one is the ground state singlet dominated by configurations with one unpaired electron per magnetic site (*neutral* singlet), and the second state is the so-called *ionic* singlet, which is dominated by configurations where the unpaired electron of one magnetic site is transferred to the other. Because of the double occupancy of the magnetic orbitals in the ionic singlet, the inclusion of this state in the orbital optimization procedure results in a set of orbitals with a higher degree of delocalization than the standard procedure. The optimal ratio between neutral and ionic states was determined by maximizing the overlap of the SA optimized magnetic orbitals with the natural DDCI orbitals. A ratio of 70% - 30% was found to give maximum overlap in a representative series of complexes and this ratio also turned out to provide accurate magnetic couplings when used in the perturbative treatment of the dynamic electron correlation based on a minimal active space.

In the case binuclear nickel systems, the two Ni(II) sites (d^8 configuration) have spin angular moments $S = 1$ and the minimal active space to account for their magnetic coupling includes four electrons in four orbitals CAS(4,4). As test systems, we selected a series of complexes with different bridges, represented in Figure 6.1. The structure of the complexes was taken from X-ray crystallographic data and (when necessary) slightly modified to adapt it to a specific symmetry point group. Previous studies suggest that small geometrical changes to symmetrize the structure do not significantly affect the calculated coupling strength [106, 107].

First, we present two complexes which have a double end-to-end azido bridge between the Ni(II). The general formula is $[Ni(\mu_{1,3}\text{-}N_3)(R)]_2^{2+}$, where the external ligands are R = 5,5,7,12,12,14-hexamethyltetraazacyclotetradecane (**1a**) and 1,2-diaminopropane (**1b**). Both compounds have a strong antiferromagnetic coupling

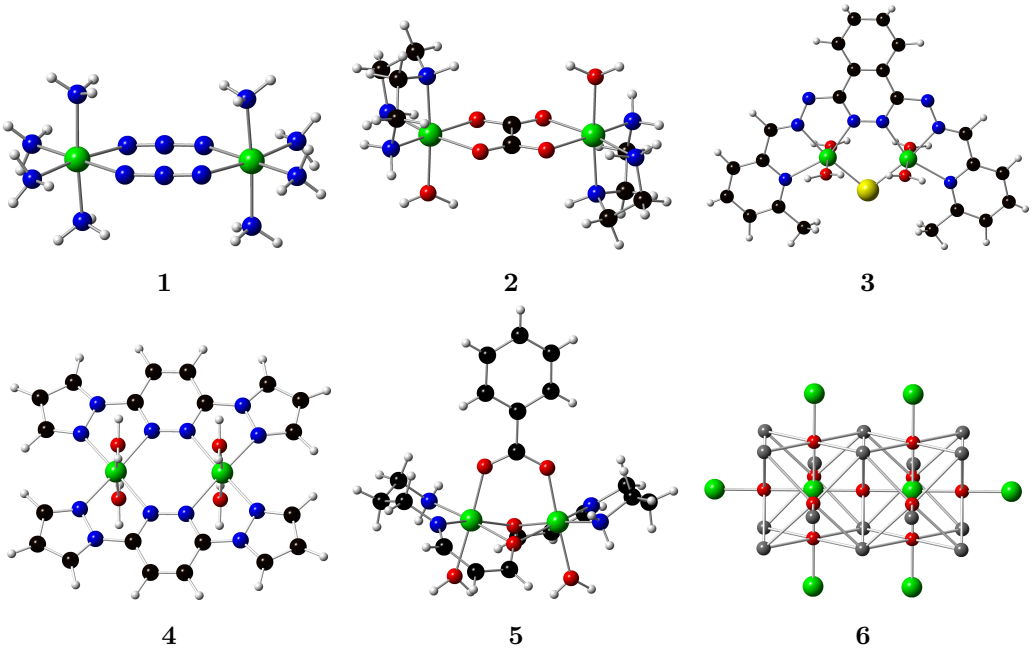

Figure 6.1. Structures of the Ni_2 systems. Color coding for the atoms: nickel, green; carbon, black; oxygen, red; nitrogen, blue; chlorine, yellow; hydrogen, white; lanthanum, grey.

Figure 6.2. Symmetry-adapted g magnetic orbitals for system **1b**. (Isovalue = 0.03)

(J) of -75.1 and -114.5 cm^{-1} respectively [108, 109], and they differ in the dihedral angle between the Ni(II) coordination spheres with respect to the bridge [109, 110]. To facilitate the calculations we have replaced the external ligands with NH_3 groups. As for the symmetrization, this only has a weak influence on the calculated coupling [107].

$[Ni_2(dien)_2(H_2O)_2(ox)]^{+2}$ (dien = diethylenetriamine, ox = oxalate) (**2**) with $J = -28.8$ cm^{-1} has an oxalato-bridge [111]. More complex bridges are found in the complexes **3**-**5**. First we consider $[Ni_2(PHP6Me)Cl(H_20)_4]^{3+}$ (PHP6Me = 1,4-bis((6-methylpyridine-2-carboxaldimino)amino)phthalazine) (**3**)[112] with $J = -25.98$ cm^{-1} and $[Ni_2(ppd)_2(H_20)_4]^{4+}$ (ppd = 3,6-bis(1'-pyrazolyl)pyridazine) (**4**) [113] with $J = -29.6$ cm^{-1}. The Ni(II) ions in $[Ni_2L_2(O_2CPh)(H_2O)2]^+$ (L = 2-[(3-Methylamino-propyl imino)-methyl]-phenoxide) (**5**) [114] with $J = -16.48$ cm^{-1} are coupled through a triple bridge: one carboxylate group and two alkoxo groups. Finally, the Ni(II) ions in La_2NiO_4 (**6**) are connected by an O^{2-} ion. The linear Ni–O–Ni pathway gives rise to a very strong coupling ($J = -240$ cm^{-1}). The coupling in this extended system was calculated using a Ni_2O_{11} fragment embedded in a set of point charges and total ion potentials simulating the Madelung potential of the infinite crystal and the short-range Coulomb and exchange interactions with the surrounding, respectively.

The reference wave function for the DDCI and MC-PT2 calculations was obtained at the CASSCF(4,4) level. The compounds present a C_i symmetry point group, except **4** which has C_{2v}. Figure 6.2 shows the magnetic orbitals of gerade (g) symmetry, a combination of $3d_{xy}$ (a) and $3d_{z^2}$ (b) Ni orbitals. According to previous studies, the former has a higher contribution to the spin coupling due to the favorable delocalization in the plane containing the nickel and the bridge atoms [89].

To obtain a test set of molecular orbitals with a larger degree of delocalization an excited electronic state with ionic character has to be identified. However, due to the size of the active space, a large number of ionic singlet states appear in the calculation, in contrast to the copper case where at most two ionic states are possible. Moreover, local excited states (d-d transitions) also form part of the CAS space. Therefore, the first step was to identify the states which were relevant for the magnetic coupling under study.

To facilitate the analysis of the electronic states the symmetry adapted magnetic orbitals were transformed to local atomic-like orbitals by a unitary transformation based on the projection of a model vector in the active space [79]. Orbitals localized on the left/right Ni(II) ion are labelled with A and B, respectively. The ground state (1^1A_g) is dominated by the configuration state functions with one electron in each magnetic orbital arising from the $M_S = 0, \pm 1$ components of the local triplet states. This "neutral" character of the ground state is also present in the first nine excited singlet states. All these states have multiconfigurational character and are dominated by configurations in which an electron is transferred from one magnetic orbitals to the other on the same site. Their energy is in the region between 4 and 10 eV above the ground state. The next excited singlet state is at 26 eV above the ground state at CASSCF level. This ionic state (8^1A_g) is basically a combination of two configurations; one with two electrons in $A_{3d_{xy}}$ and two singlet coupled electrons in $A_{3d_{z^2}}$ and $B_{3d_{xy}}$, and the other with two electrons in $B_{3d_{xy}}$ and two singlet coupled electrons in $A_{3d_{xy}}$ and $B_{3d_{z^2}}$. That is, one of the $3d_{z^2}$ orbitals loses its electron in favor of the other atom's $3d_{xy}$ orbital. Close in energy we found similar ionic states with configurations where the $3d_{z^2}$ orbitals are doubly occupied instead of the $3d_{xy}$ ones. Finally, more than 90 eV above the ground state there are two doubly ionic states with configurations where the 4 electrons belong to a single atom. Taking into account that the $3d_{xy}$ orbitals are more important for the spin coupling than the $3d_{z^2}$ ones, we selected the first ionic gerade state for the SA-CASSCF calculations, obtaining a set of MOs from wave functions with a mixing of 50% 1^1A_g / 50% 8^1A_g ($W = 50\%$) up to 90% 1^1A_g / 10% 8^1A_g ($W = 90\%$) following the recipe applied for the Cu(II) binuclear complexes [84].

The overlap of the magnetic orbitals obtained in the SA-CASSCF with different weights of ionic state (S) with the natural DDCI orbitals (N) is calculated by

$$ovl(S,N) = \sqrt{\frac{\sum_{i\in S}\sum_{j\in N} | < i|j > |^2}{n}} \tag{6.5}$$

where n is the total number of magnetic orbitals (four in this case) and i and j are the SA-CASSCF and IDDCI magnetic orbitals, respectively. This ensures that the calculated overlap does not depend on the particular representation of the magnetic orbitals (localized-delocalized and redundant orbital rotations in the active space).

Table 6.1. Magnetic coupling constant -J(cm^{-1}) calculated using state specific CASSCF(4,4) MOs for complexes **1a**, **2** and **3**. The J-values refer to E(S)-E(T) and [E(T)-E(Q)]/2, except for IDDCI where only the latter is reported.

	1a	**2**	**3**
CASCI	10 / 11	4 / 3	2 / 2
CASPT2	62 / 48	22 / 17	20 / 13
SC-NEVPT2	27 / 24	7 / 6	6 / 5
PC-NEVPT2	29 / 26	7 / 7	7 / 6
IDDCI	65	21	15
Exp.	75.1	28.8	26

6.3.2 Results

Table 6.1 shows the magnetic coupling constant J for systems **1a**, **2** and **3** using the state specific CASSCF(4,4) molecular orbitals. As stated before, NEVPT2 couplings with these MOs are weaker than the IDDCI result, which in turn is in rather good agreement with experiment. Small differences may arise from the symmetrization, modelling of the external ligands and truncation of the MO space after the dedicated orbital transformation. The CASPT2 estimates of J obtained from E(S)-E(T) are reasonable. If we analyze the deviation from the Heisenberg behavior, we observe that NEVPT2 results nicely fit the Landé pattern, while CASPT2 shows significant deviations. For these systems, the number of determinants in the singlet DDCI functions are rather large ($\approx 1.0 \times 10^8$) and it becomes computationally quite expensive to obtain IDDCI converged energies for the singlets. Hence, we cannot directly access the degree of deviation from Heisenberg at this level of calculation. However, previous theoretical studies on system **1a** [110] and related complexes [83, 115] show that the deviations obtained in DDCI are in general small. This means that the deviations to the Heisenberg behavior observed with CASPT2 are not physically grounded, as previously concluded for other complexes [83, 116, 117].

To decide on the optimal weight of the ionic state in the SA-CASSCF orbital optimization, we have calculated the overlap of the magnetic orbitals for different weights of the neutral state (W). Table 6.2 shows how the overlap of the SA-CASSCF and IDDCI natural magnetic orbitals evolves as function of W. The trend

Table 6.2. Overlap of the magnetic SA-CASSCF and IDDCI natural orbitals for different weights (W, %) of the neutral state used in the orbital optimization. $W = 100\%$ correspond to the singlet ground state MOs. The maximum overlap is marked in bold.

W	**1a**	**1b**	**2**	**3**	**4**	**5**	**6**
50	0.9675	0.9722	0.9903	0.9905	0.9845	0.9919	0.9891
60	0.9913	0.9914	0.9950	0.9959	0.9947	0.9959	0.9951
65	0.9950	0.9947	0.9959	0.9975	0.9965	0.9966	0.9969
70	0.9962	0.9959	**0.9962**	0.9984	**0.9971**	**0.9967**	0.9981
75	**0.9962**	**0.9961**	0.9960	0.9989	0.9968	0.9964	0.9986
80	0.9957	0.9958	0.9956	**0.9991**	0.9962	0.9960	**0.9987**
90	0.9938	0.9946	0.9939	0.9987	0.9938	0.9944	0.9977
100	0.9918	0.9929	0.9925	0.9979	0.9919	0.9930	0.9967

is more or less uniform for all the compounds, increasing with the neutral % until reaching a maximum and then decreasing again for smaller weights of the ionic state. This "inverted parabola" shape is consistent with the previous copper study. The maximum is located in the region between $W = 70$ to 80, with an overlap quite close to 1, as found for the copper complexes.

This is also illustrated in Figure 6.3, where it can be clearly seen that the singlet state CASSCF $3d_{xy}$ orbital is more compact, more localized on the metals, than the IDDCI natural orbital. As stated before, this difference is crucial when working with MC-PT2 methods. We can also see that the SA-CASSCF orbital is quite similar to the IDDCI natural orbital.

In Table 6.3, we present the NEVPT2 results for systems **1a**, **2** and **3** obtained with the cited SA-CASSCF MOs, focusing on the optimal range $W = 70 - 80\%$ based on the overlap analysis. As in the case of the Cu(II) dinuclear complexes,[84] a decrease of the neutral weight (W) in the SA orbitals leads to an increase of the antiferromagnetic character of the coupling. The calculated values reach a nearly exact coincidence with the IDDCI estimates around $W = 70\%$; for **1** at slightly larger value and for **2** at somewhat smaller W. This is the same percentage of neutral/ionic mixing found for Cu compounds. Despite the fact that Ni ion has a local $S = 1$ spin state, only one of the two unpaired electrons can be efficiently coupled by means of the superexchange through the bridging ligands. Therefore,

Table 6.3. PC-NEVPT2 magnetic coupling constants -J (cm^{-1}) for **1a**, **2** and **3** as function of the weight of the neutral state W (%) used in the SA-CASSCF(4,4) orbital optimization. The values refer to E(S)-E(T) and [E(T)-E(Q)]/2.

W	**1a**	**2**	**3**
65	125 / 126	21 / 21	21 / 20
70	81 / 81	17 / 17	15 / 15
75	56 / 56	14 / 14	11 / 11
80	41 / 41	12 / 12	9 / 9
IDDCI	65	21	15

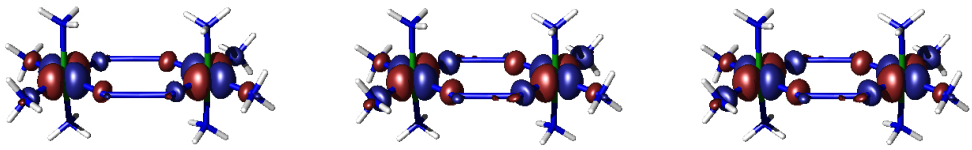

a **b** **c**

Figure 6.3. Symmetry-adapted gerade magnetic orbital of $3d_{xy}$ character of complex **1b** for singlet state specific CASSCF (a), SA-CASSCF ($W = 70$) (b) and IDDCI Natural Orbitals (c). (Isovalue = 0.03)

similar mechanisms are governing the physics of the binuclear Cu and Ni complexes, and this could explain why they behave in a similar way regarding the optimization of the MOs in the state-average procedure.

Furthermore, the results in Table 6.3 show that the Landé pattern for the splitting of the three spin states is maintained for all weights in the NEVPT2 calculations. Using SA-CASSCF orbitals to express the reference wave functions for CASPT2 does not lead to an improved description. The deviations to the Heisenberg behavior remain (or get worse) and the calculated J-values are not better than those obtained with state-specific orbitals using the singlet-triplet energy difference to determine J.

Table 6.4 shows the magnetic coupling constant with state specific and SA-CASSCF MOs ($W = 70 - 80\%$) for complexes **1b** and **4-6**. In line with the analysis for **1a**, **2** and **3**, the same pattern is observed, that is, (i) too small values for CASCI and NEVPT2 with state specific MOs, (ii) reasonable agreement with IDDCI and

Table 6.4. Magnetic coupling constant -J(cm^{-1}) calculated for systems **1b** and **4-6**. The values refer to E(S)-E(T) and [E(T)-E(Q)]/2.

	1b	**4**	**5**	**6**
CASCI	14 / 13	5 / 4	1 / 1	76 / 70
CASPT2	87 / 68	23 / 16	5 / 1	219 / 206
SC-NEVPT2	24 / 23	12 / 11	4 / 2	162 / 147
PC-NEVPT2	27 / 27	13 / 12	1 / 2	168 / 154
IDDCI	94	19	3	228
W	PC-NEVPT2 with SA-CASSCF MOs			
70	53 / 52	21 / 21	9 / 9	206 / 214
75	42 / 42	17 / 17	5 / 5	177 / 183
80	37 / 36	14 / 14	3 / 3	155 / 160
Exp.	115	29.6	16.5	242

experiment for CASPT2 when state-specific orbitals are used only if the singlet-triplet energy difference is considered, (iii) significant improvement when NEVPT2 is applied with SA-CASSCF($W = 70\%$) orbitals, (iv) and important deviations to Heisenberg in the CASPT2 spectrum. The large coupling between the Ni(II) ions in La_2NiO_4 crystal (**6**) is also reasonably reproduced with NEVPT2 based on SA-CASSCF($W = 70\%$) orbitals, although small deviations from the Landé pattern are observed. These deviations were reported for DDCI calculations as well and were ascribed to a non-negligible contribution of biquadratic interactions [89].

Finally, we compare the performance of the different methods taking into account the percent error with respect to the experimental values. Table 6.5 shows the percent difference between the calculated and experimental J values. First of all, we can see the good performance of singlet-triplet CASPT2 using state specific MOs, with an average error of 27%. It is worth mentioning again that CASPT2 does not follow the Landé pattern expected from the Heisenberg behavior and in cases with weak coupling the ground state is not always the correct one.[83] Moreover, it can be anticipated that CASPT2 will be less suitable for antiferromagnetic systems with many unpaired electrons. In these cases, J is only accessible from the energy difference between the states with the highest spin multiplicity due to the size of the active space for low-spin coupled states. However, the deviations in the Landé

Table 6.5. Percent errors (%) for the different methods used in this work.

	State Specific		State Average	
	CASPT2	PC-NEVPT2	PC-NEVPT2	IDDCI
1a	17	61	8	13
1b	24	76	54	18
2	24	76	41	27
3	23	77	42	42
4	22	59	29	36
5	70	112	45	-
6	10	31	13	6
Average	27	70	33	24

pattern for these states observed here makes such approach highly unreliable.

As stated before state specific PC-NEVPT2 performs poorly in our study (average of 70% error) but the use of SA-CASSCF MOs with a 70% of neutral weight greatly improves the results of this method (33% error) and results become comparable to CASPT2 with the advantage of correct Heisenberg behavior and no appearance of intruder states. Finally, we need to mention the IDDCI performance (24% error) which is slightly bigger than generally obtained with this method in other compounds. The IDDCI results are directly affected by the approximations made in this work, namely a removal of virtual orbitals to reduce the space of determinants to make the calculations of the biggest systems tractable.

6.4 Magnetism in nickel EMACs

Several Ni(II) based EMACs of increasing length have been reported, ranging from the 'standard' Ni_3 chain to EMACs with 9 metal ions in a row [118, 119]. All these EMACs share the common characteristic that the ions at the ends of the chain have two unpaired electrons coupled to triplet, while the inner ions are all diamagnetic. Therefore they present unique opportunities to study the mechanism that govern the magnetic coupling between metal centers. Compounds with varying number of

Table 6.6. Experimental magnetic coupling constant -J(cm^{-1}) and the distance between terminal centers (magnetic) (Å) for different Ni(II) EMACs [118, 119].

Compounds	-J	d(Ni_1-Ni_n)
$Ni_3(dpa)_4Cl_2$	99	4.886
$Ni_5(tpda)_4Cl_2$	8.3	9.380
$Ni_7(teptra)_4Cl_2$	3.8	13.812
$Ni_9(peptea)_4Cl_2$	1.7	18.344
$Ni_5(tpda)_4(NCS)_2$	9.24	9.330
$Ni_5(tpda)_4(N_3)_2$	8.17	9.354
$Ni_5(tpda)_4Cl_2$	8.27	9.382
$Ni_5(tpda)_4(CN)_2$	6.40	9.392

nickel atoms in the chain show that the magnetic coupling between two centers is inversely proportional with the distance between them (upper part of Table 6.6). In almost any transition metal complex, changing the distance between the magnetic centers requires altering the bridging ligands that connect and support them in place but in the case of EMACs, this can be achieved by changing the axial ligands (X) which are not in the path of the magnetic coupling (lower part of Table 6.6). In this section we propose the use of the newly developed Multiconfigurational pair-density functional theory, MCPDFT, in the $Ni_3(dpa)_4Cl_2$ compound, discuss the case of larger systems and present the results of the Ni_5 case.

6.4.1 Multiconfigurational pair-density functional theory

One of the problems of DFT is the treatment of multireference systems and nearly degenerate states in an accurate way. On the other hand, MCSCF methods are able to treat such systems without much problems, except they do not account for the dynamic correlation and require a post-SCF (CI, MC-PT2) correction which is usually computationally demanding. Many attempts to combine the best of both methods have been proposed, either by adding some amount of DFT-based correlation to a multiconfigurational wave function calculation or adding some amount of wave function correlation to a DFT calculation (see references in [94])

Multiconfigurational Pair-Density Functional Theory (MCPDFT)[94] is a method that describes static correlation by a MCSCF calculation, and includes dynamic correlation with a DFT-based approach. One of the main problems that arise in such treatment is the double counting of electron correlation. A second problem is that existing functionals are not compatible with spin densities of multiconfigurational wave functions. According to the developers of the MCPDFT method, double counting is solved by considering only the Coulomb and a part of the kinetic energy from the MCSCF calculation, and the two-electron terms with the DFT-based formalism.

$$E = V_{nn} + \langle \Psi | \, T + V_{ne} \, | \Psi \rangle + V_c[\rho] + E_{ot}[\rho(r), \Pi(r)] \tag{6.6}$$

The density functional form is expressed in terms of the total spin density ρ and the on-top pair density Π, defined by[120]

$$\Pi(r) = \binom{N}{2} \int |\Psi(r_1\sigma_1, r_2\sigma_2, ..., r_N\sigma_N)|^2 d\sigma_1 d\sigma_2 ... d\sigma_N dr_3 ... dr_N \tag{6.7}$$

given $r_1 = r_2 = r$, where r_i and σ_i are space and spin variables respectively.

The idea of using the on-top density in DFT is not new [121–123], but the contribution of this method is the formulation of the on-top density functional $E_{ot}[\rho(r), \Pi(r)]$ which is compatible with the multiconfigurational wave function. As a first approximation E_{ot} is a translation of the previously developed exchange-correlation functionals of spin densities $\mathrm{E}_{xc}(\rho, m, \nabla\rho, \nabla m)$, where m is the spin magnetization density.

$$\rho(r) = \rho_\alpha(r) + \rho_\beta(r) \tag{6.8}$$

$$m(r) = \rho_\alpha(r) - \rho_\beta(r) \tag{6.9}$$

which for a single determinant wave function are related to Π as

$$m(r) = \rho(r)[1 - R(r)]^{1/2} \tag{6.10}$$

$$R(r) = \frac{4\Pi(r)}{\rho(r)^2} \tag{6.11}$$

with $R \leq 1$ for all r. For multiconfigurational wave functions R can be larger than 1, and in that case $R[\rho(r), \Pi(r)]$ is set to one, in order to generalize the on-top density functional as

$$E_{ot}[\rho(r), \Pi(r)] = E_{xc}\left(\rho(r), \rho(r)[1 - R(r)]^{1/2}, \nabla\rho(r), \nabla\rho(r)[1 - R(r)]^{1/2}\right) \tag{6.12}$$

6.4.2 Magnetic coupling parameters for Ni_3 and Ni_5 EMACs

We start the discussion of the MCPDFT results by comparing it to previous work performed on the Ni_3 EMAC with standard CASSCF/CASPT2 calculations.[87, 124] We used the same geometry, basis set and molecular orbitals as the information was available in our work. Table 6.7 shows the results of the different MC methods with minimal and extended active spaces, the DFT (PBE and B3LYP) and experimental values. MCPDFT performs as CASPT2 does, recovering the dynamic correlation to improve the results of the CASSCF calculation. For the extended active space, CAS(10,13), MCPDFT is almost as good as CASPT2, a method with a much larger computational cost. Compared to DFT, MCPDFT gives a much better description than the parent PBE functional, and similar results to the broadly used hybrid B3LYP.

So far, the study of nickel EMACs with multiconfigurational methods has been restricted to the Ni_3 case. Here we propose to extend the study to larger systems, starting with the $Ni_5(tpda)_4(NCS)_2$ compound. As in all the nickel EMACs, the minimal active space consist of four electrons in four orbitals CAS(4,4) of σ-$3d_{z^2}$ and δ^*-$3d_{xy}$ character. Following the recipe of the Ni_3 case, the extended active space would require 9 orbitals per diamagnetic nickel, an amount far from what the actual multiconfiguration schemes can handle. Upon further review of the molecular

Table 6.7. Magnetic coupling constant -J(cm^{-1}) calculated for $Ni_3(dpa)_4Cl_2$. The values refer to the average of E(S)-E(T) and [E(T)-E(Q)]/2.

Method	-J	Ref
CAS(4,4)	7.0	[87]
CASPT2(4,4)	48.6	[87]
MCPDFT(4,4)	23.1	this work
CAS(10,13)	31.1	[87]
CASPT2(10,13)	97.5	[87]
MCPDFT(10,13)	93.7	this work
PBE	537	this work
B3LYP	112.5	[124]
Exp.	99-108	[119, 125]

orbitals, we noticed that the molecular orbitals of the internal Ni(II) can be found delocalized in this inner diamagnetic Ni_3 chain, present inside the Ni_5 EMACs. From these molecular orbitals, we selected those that share the character of the magnetic orbitals (σ and δ) and participate in the exchange path. Since the occupation numbers of the additional orbitals are very close to two or zero, the Restricted Active Space (RAS) formalism was used with up to two holes and two particles. This is a good approximation to the problem, which otherwise would be much more difficult to converge in the full CASSCF(16,20). Figure 6.4 shows the molecular orbitals used in the extended RASSCF(6,4,10) calculation. The six additional occupied orbitals (labeled 1σ and 1δ) consist of the inner Ni_3 3d σ and δ manifolds. The unoccupied orbitals include the 4d σ and δ orbitals of the Ni_3 part (six, 4σ and 4δ) and the magnetic centers (four, 3σ and 3δ). The latter molecular orbitals were not included in the previous study of the trimetallic chain, but our tests suggest that their inclusion helps the convergence of the active space as it can been seen they share some contributions with the inner Ni_3 part.

Table 6.8 presents the results of the magnetic coupling constant for $Ni_5(tpda)_4(NCS)_2$, where the minimal active space CAS(4,4) is once again insufficient to distinguish between triplet and quintet states. The correction of the MCPDFT method improves the description, and with the extended active space RAS(6,4,10) it achieves a fairly good agreement with the experimental value. This

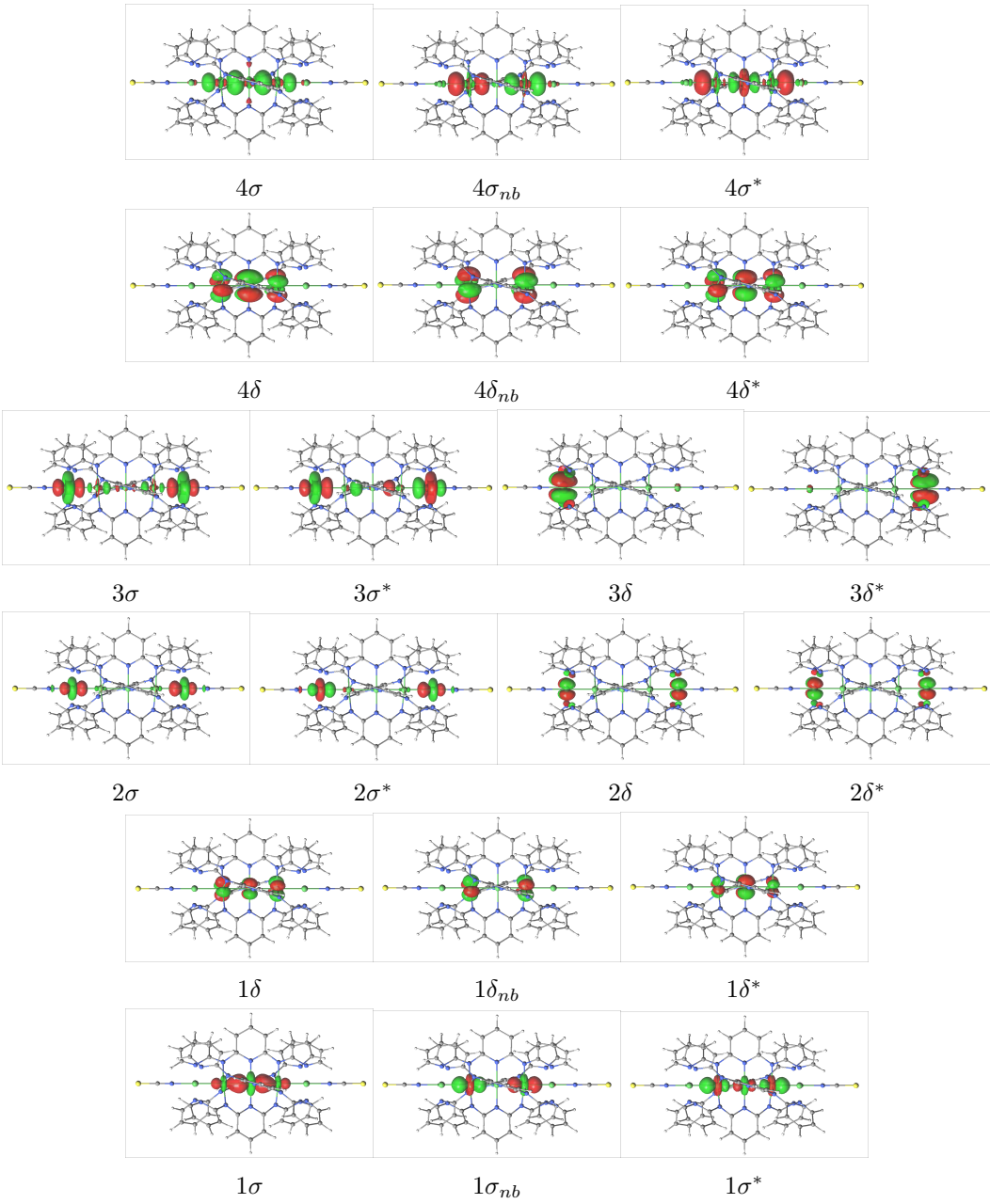

Figure 6.4. Molecular orbitals of the RAS(6,4,10) active space of $Ni_5(tpda)_4(NCS)_2$. Orbitals labeled by the RAS space (1 for RAS1, 2 for RAS2, and 3 and 4 for RAS3), their symmetry along the Ni_5 axis (σ or δ) and the *bonding* character (bonding, non-bonding or antibonding).

is a promising result because the MCPDFT step requires less CPU-time that the preceding optimization of the RASSCF wave function. In standard MC-PT2 application for such large systems this is normally the other way around; the treatment of the dynamic correlation takes much longer than the multiconfigurational wave function optimization. Furthermore, we observe that the selection of the twenty active orbitals gives a very reasonable estimate of J after the MCPDFT treatment, whereas RASPT2 with this reference wave function predicts two nearly uncoupled Ni(II) ions at the extreme of the chain.

Table 6.8. Magnetic coupling constant -J(cm^{-1}) calculated for $Ni_5(tpda)_4(NCS)_2$. The values refer to [E(T)-E(Q)]/2.

Method	-J
CAS(4,4)	0.04
MCPDFT	0.39
RAS(6,4,10)	0.08
MCPDFT	6.45
Exp.	9.24

6.5 Conclusions

In this chapter we studied two different approaches in the calculation of magnetic coupling constants. First we expanded the study of the role of magnetic orbitals in MC-PT2 methods. After the cited results on copper, the natural choice was to focus on nickel binuclear complexes as the next step in complexity. The study covers a wide range of antiferromagnetically coupled compounds with different bridge types, which serve as a good testing ground. The results are promising as we show that PC-NEVPT2 can be greatly improved using a set of MOs that are easy to obtain but have the same characteristics as the natural orbitals determined via a computationally expensive scheme. The proposed strategy has an outstanding "accuracy / computational cost" ratio, which might lead this computational scheme to a further wide use. Although the complexity of this technique increases with the number of unpaired electrons and magnetic centers –there will be more and more

roots between the magnetically interesting neutral state and the first ionic state– our future work will be focused on the application to more complex systems, where DDCI calculations are definitely out of the question.

In the second part of this chapter, we presented an efficient alternative to the conventional MC-PT2 methods. As most MCSCF methods, MCPDFT relies on the chemical knowledge of the system to identify the extended active spaces but it has proven satisfactory in the Ni_3 and Ni_5 compounds. The case of the Ni_5 is the first MC calculation on the magnetism of such a large EMAC, which is not tractable with the standard MC-PT2 methods. To further explore the reliability of the MCPDFT method, we are currently applying the method to other systems listed in Table 6.6. Thereafter, the method should be tested for other metal ions and geometries.

Chapter 7

Electron Transport in Gated ruthenium EMACs

7.1 Introduction

EMACs can be considered one of the simplest models of molecular wires in the growing field of molecular electronics. Having a chain of transition metal ions allows for a specific control in the composition, compared to macroscopic wires, and opens up the possibility of systematic structure/function relationships studies [5].

Many studies have shed some light on the question of what is needed to effectively conduct current [6, 126]. Based on a simple model of coherent electron transport, a molecule between two electrode surfaces experiences shift and broadening of its electronic levels, compared to the gas phase. In equilibrium the Fermi levels of both electrodes (source and drain) are equal (Figure 7.1 left), but when a voltage difference is applied between the two electrodes, the levels differ creating a bias window (Figure 7.1 right). Electron transport occurs only if energy levels of the molecule (channels) appear in the bias window and have the proper characteristics (i.e. Green's functions used to compute the electrical current are proportional to the molecular orbital contributions from the atoms directly bonded to the surfaces).

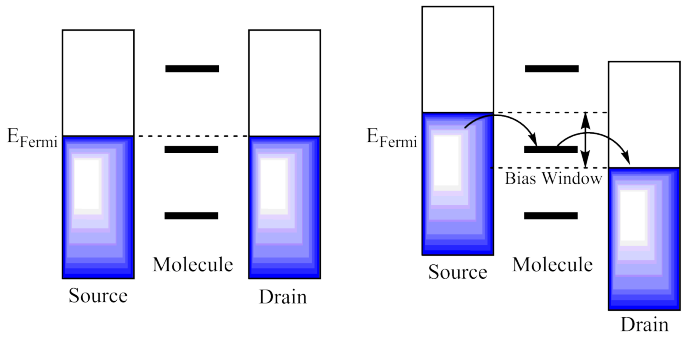

Figure 7.1. Schematic representation of electron transport. The equilibrium state (left) and the applied bias (right) that generates the current from the source to the drain electrodes.

The next logical step is to study how to control current flow in the way that rectifiers and transistors do in solid-state architectures. In the solid-state context, switching of current is done by a gate potential applied across the scattering region. The technique of electrochemical gating has emerged over the past decade as an alternative strategy, where the potential of the contact can be controlled separately to the source and drain, such that the molecule of interest can be driven through different oxidation states, each with (potentially) very different conductance properties. In this way, we can hope to switch between highly conductive and insulating states. A number of studies have shown that the conductivity passes through a maximum when a redox-active orbital enters the bias window between source and drain electrodes, leading to *off-on-off* sequences.

In the context of the EMACs, Peng's group have explored the potential gating for two triruthenium EMACs, $Ru_3(dpa)_4(X)_2$ (X = CN, NCS) [4]. Setting the potential of the gold surface (the working electrode) at specific points, they were able to cycle between 0 and +1 oxidation states, and concluded that whilst the conductance of $Ru_3(dpa)_4(NCS)_2$ was rather independent of oxidation state, the CN-capped analogue increased it by a factor of 2 upon 1-electron oxidation. The conductance was however, not studied systematically as a function of gate voltage, so it is not possible to say whether these values are representative of *on* or *off* states. In a subsequent study, the same authors reported the synthesis and electron transport properties of the closely related species $[Ru_3(npa)_4(NCS)_2]^+$, where npa is the tridentate naphthyridyl ligand (Figure 7.2).[127] The asymmetric nature of the ligand offers the

potential for isomerism in the tetra-helicate, and the crystallographically characterised molecule has 3 ligands oriented in one direction and one in the opposite. Unlike dpa analogues, the EMAC is isolated as a cation (crystallising with a PF_6^- counterion), and the Ru-Ru bond lengths are somewhat longer than those in neutral $Ru_3(dpa)_4(NCS)_2$ (see Table 7.1). The measured conductance of this asymmetric cationic EMAC is lower than that for $[Ru_3(npa)_4(NCS)_2]^+$, a difference that was ascribed to the longer Ru-Ru bonds in the former.

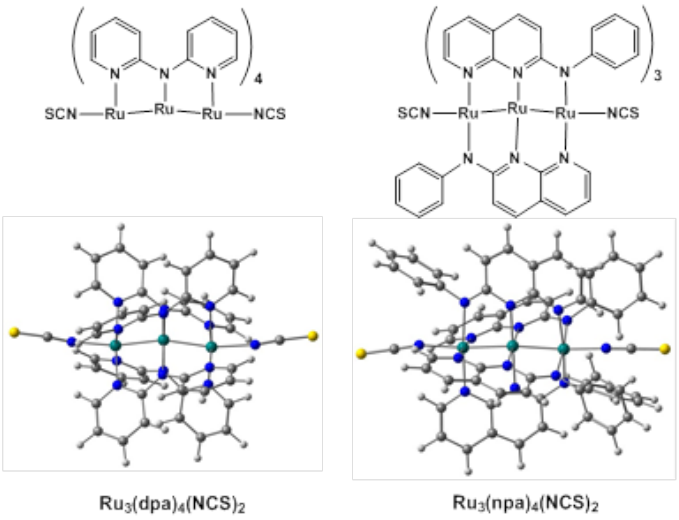

Figure 7.2. Structures of compounds **1** and **2**.

Theoretical studies by McGrady's group on the electronic structure of the $Ru_3(dpa)_4(X)_2$ molecules showed that the ground state multiplicity varies from singlet to triplet depending on the linearity of the Ru-Ru-Ru unit [128]. A bent Ru_3 chain (Ru-Ru-Ru angle of 170 degrees for NCS) favors a singlet ground state and has a higher conductivity compared to the linear triplet state. In addition, they established the π component of the Ru-Ru bond as the dominant transmission pathway, with the vacant π^* orbital lying just above the Fermi level.

In this work, we apply DFT to explore the effects of gate potential on the conductance of the Ru_3 EMACs, $Ru_3(dpa)_4(NCS)_2$ (**1**) and its asymmetric analogue, $[Ru_3(npa)_4(NCS)_2]^+$ ($\mathbf{2}^+$) (Figure 7.2). The inclusion of a gate potential offers the possibility of tuning the alignment of the Fermi level with the transmission channels, and changing substantially the dominant transport mechanisms. From a com-

Table 7.1. Principal distances (Å) and angles (^{o}) of the ruthenium EMACs. $Ru_3(dpa)_4(NCS)_2$ (**1**) and $[Ru_3(npa)_4(NCS)_2]^+$ (**2**$^+$).

Compound	Ru-Ru	Ru-NCS	Ru-N_{py}	Ru-N_{am}	Ru-Ru-Ru
1					
Experimental	2.28	2.24	2.08	2.12	171.2
DFT/PBE	2.33	2.09	2.06-2.22	2.02-2.16	165.7
2$^+$					
Experimental	2.35 2.36	2.11 2.18	2.00-2.18	1.99-2.09	170.3
DFT/PBE	2.36 2.37	2.01 2.07	2.02-2.23	2.02-2.14	167.5

putational perspective, however, the inclusion of an electrochemical gate potential represents a significant challenge, simply because the periodic nature of the treatment of the electrode surface resists the formation of charged species. It is, however, possible to mimic the effects of the electrochemical gate by including a counterion in the unit cell that will effectively add or remove an electron from the molecule under study. Here, we compare this approach to the more conventional application of a solid state gate potential, and show that both roughly yield comparable results. We show that the presence of a gating potential shifts the molecular energy levels in a predictable way relative to the Fermi level, with distinct peaks in the conductance trace emerging as these levels enter the bias window.

Finally, we study the asymmetry of complex **2** given by the npa ligand. We compare the electrical current of the experimental 3:1 ligand distribution with a fictitious 2:2 isomer, in order to see if this asymmetry produces an effect on the electron transport and whether the system could have rectifier character.

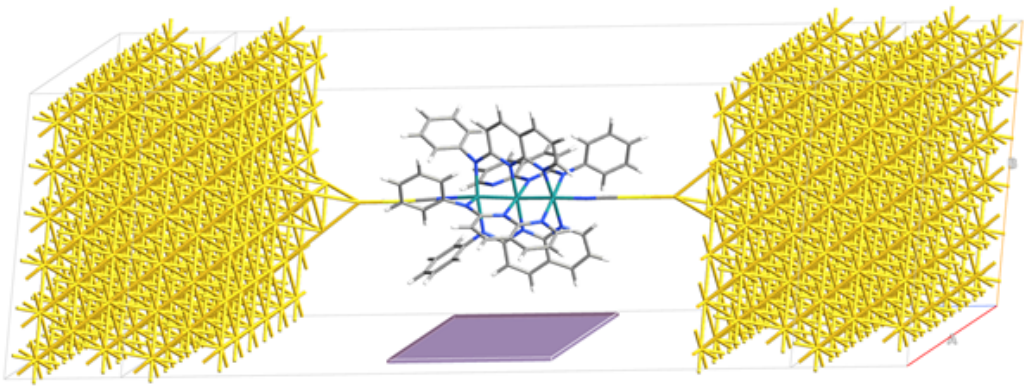

Figure 7.3. Device configuration with $Ru_3(npa)_4(NCS)_2$ (**2**) between two (1,1,1) gold electrodes.

7.2 Computational Details

All calculations on the isolated molecules were performed with the Amsterdam Density Functional package (ADF2013.01)[67–69] using the PBE [129] functional with relativistic scalar corrections (ZORA) [130] and TZP and DZP basis sets for Ru and the main-group atoms, respectively.

All the calculations of the device configuration were done with the Atomistic Toolkit software package, ATK 13.8.1 program [30, 131–134]. The methodology combines a density functional theory treatment of the electronic structure with the Keldysh non-equilibrium Green's function approach to simulate coherent transport [135–138]. The transport calculations were performed using the LDA functional with the self-interaction correction of Perdew and Zunger [139]. Numerical basis sets of DZP quality on all the atoms except for Au (SZP) were used, and core electrons were described by norm-conserving pseudopotentials [140]. The electronic structure of the systems at equilibrium was converged using a 300 Ry mesh cutoff, a finite temperature of 300 K at the electrodes and the real-space density constraint at the electrodes. Sampling of the Brillouin zone was performed using a MonkhorstPack grid [141] with 300 k-points along the transport direction. The molecular orbitals in the scattering region are the eigenfunctions of the Molecular Projected Self-consistent Hamiltonian (MPSH). A (1,1,1) gold surface was used with six slabs on each electrode. Additionally, a pyramidal tip of four gold atoms was constructed to

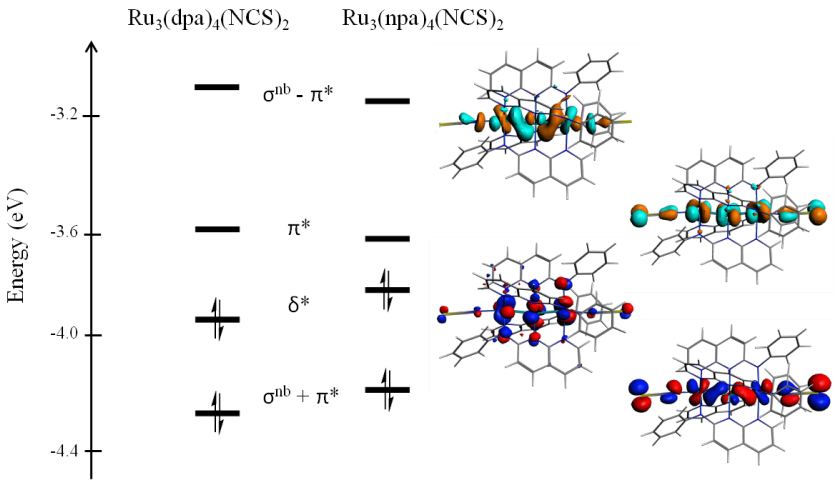

Figure 7.4. Kohn-Sham molecular orbitals for the gas phase calculations.

increase the separation between the molecule and the surface and avoid any close contacts, particularly with the terminal phenyl groups of the npa ligands. The gate electrode consisted of two regions (parallelograms), a thin metallic one, which sets the potential, and a wide dielectric one. The coordinates of the regions were set up following the ideas at quantumwise.com. Figure 7.3 shows the device configuration of npa with the gate electrode region. The regions span a rectangle of 13 Å(x) by 10 Å(z) in the xz plane, centered with respect to the coordinates of the central Ru atom. The width of the two regions: metallic 0.05 Å and dielectric 0.25 Å.

7.3 Electronic structure and gate electrode's effect

As discussed in previous works, triruthenium EMAC structures favor non-linear Ru_3 chain with bond lengths and angles reported in Table 7.1. The distinct bending of the Ru_3 unit leads to mixing of the σ orbitals with one component of the previously degenerate π. The frontier Kohn-Sham orbitals for **1** and **2** as calculated in the gas phase, are compared in Figure 7.4. It features a HOMO with Ru-Ru-Ru δ^* character, which in the case of $\mathbf{2}^+$ constitutes the SOMO, and a LUMO with strictly Ru π^* character. Orbitals further from the Fermi level (HOMO-1, LUMO+1) have mix σ/π character, arising from σ^{nb} and 'in-plane' π^*. The relative positions of the frontier

orbitals of the two systems are roughly similar, although the δ^* HOMO/SOMO lies much closer to the π^* LUMO than the $\sigma^{nb} + \pi^*$ HOMO-1 in $\mathbf{2}^+$, leading to the apparently facile oxidation.

In the device configuration, the most relevant molecular levels can be projected into the HOMO-1, HOMO and LUMO molecular orbitals previously discussed (Figure 7.5). Figure 7.6 presents the transmission spectra of the two compounds of interest, **1** and **2**, without source-drain bias. Before adding the gate electrode (Figure 7.6 top) both systems present significant transmission peaks corresponding to the aforementioned channels ($\sigma^{nb} + \pi^*$, δ^* and π^*). The δ^* peak is considerably narrower than the other two, as the atomic orbitals involved lie parallel to the gold surface, leading to very weak coupling. The spin-α (blue) and spin-β (red) components of the molecular orbitals ($\sigma^{nb} + \pi^*$, δ^* and π^*) are degenerate and the δ^* orbital falls below the Fermi level for both systems. This indicates that following absorption onto the gold surface, **2** is effectively neutral, rather than cationic as in the isolated molecule. This is a natural consequence of the periodic nature of calculations which prevent unit cells from carrying a net charge. However, we can see that the δ^* (HOMO) orbital is distinctly closer to the Fermi level for **2**, consistent with the greater ease of oxidation, and also with the narrower HOMO-LUMO gap in the isolated molecule.

At this point we include the solid gate electrode and observe the effect of the gate potential (in Volts) on the transmission spectrum. The first thing we notice is that the channels respond to the presence of the metallic gate electrode even with 0.0 V applied voltage (Figure 7.6 bottom). Both systems shift the transmission peaks down and in the case of **1**, the spectrum retains most of its features. For **2**, however, the downshift is sufficient to bring the lower tail of the π^* peak below the Fermi level, and transfer of electron density from the gold surface leads to splitting of all peaks into spin-α and spin-β components (the exchange interaction ensures that it is energetically more favorable to transfer a single electron with defined spin (α) than to transfer the same amount of unpolarised spin density).

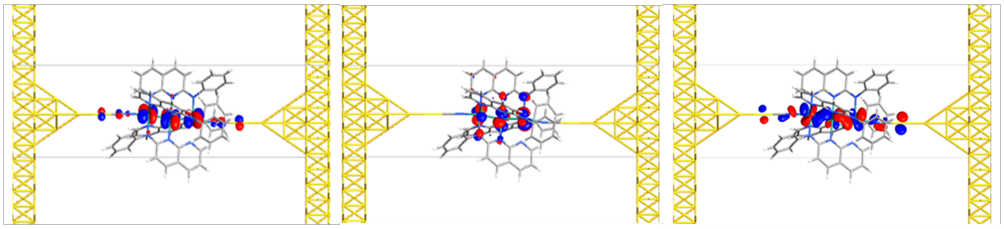

Figure 7.5. Projected Molecular orbitals from the frontier energy levels (π^* left, δ^* center and $\sigma^{nb} + \pi^*$ right) represented in the transmission spectrum of **2**.

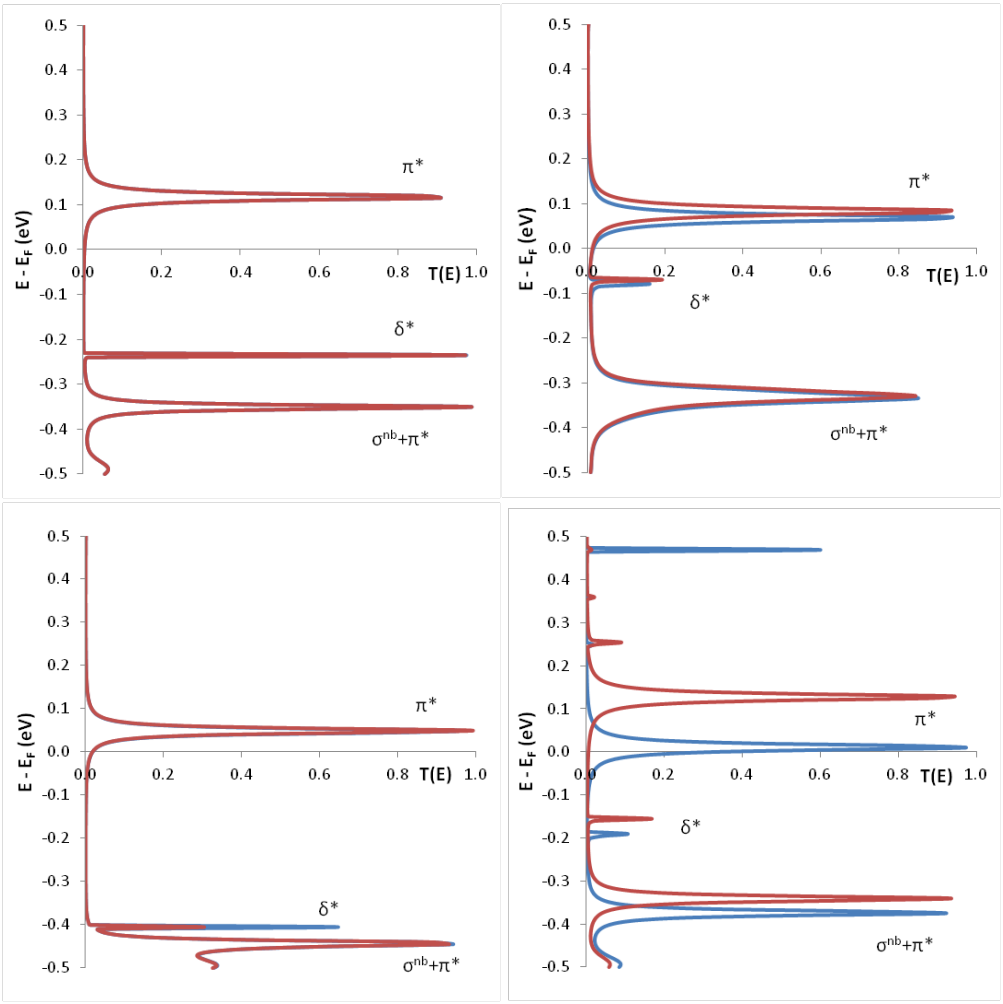

Figure 7.6. Transmission Spectra for **1** (left) and **2** (right) without source-drain bias. Calculation without the gate (top) and with a gate potential of 0.0 V (bottom). Spin-α (blue) and spin-β (red) components.

The evolution of the eigenvalues of the molecular projected self-consistent Hamiltonian (MPSH) with the gate potential is shown in Figure 7.7. As the gate potential drives molecular levels across the Fermi level the molecule is oxidized or reduced, and switched between diamagnetic states, where the spin-α and spin-β components (blue and red, respectively) of each level are degenerate, and paramagnetic states where the two components diverge. In the case of **1**, at a gate potential of -1.0 V the δ* level remains wholly below the Fermi level and the molecular region is neutral. In contrast, at -3.5 V, the spin-α and spin-β components of the δ* channel span the Fermi level and the complex is 1-electron oxidized. Even at more negative gate voltage (-8.0 V), the spin-α component of the δ* orbital is also raised above the Fermi level, the molecule is oxidized to the diamagnetic $\mathbf{1}^{2+}$ state and the degeneracy of the spin-α and spin-β components is restored. At the opposite end, a positive gate potential of +1.0 V, pushes down the spin-α component of the π* orbital below the Fermi level, effectively reducing the molecule to the paramagnetic $\mathbf{1}^{-}$ state. The same sequence of redox events is observed for **2**, but the gate potentials required to drive the redox transitions are significantly different. Taking into account that the presence of the gate electrode is already sufficient to partially reduce the system (**2** at 0.0 V), we observe that at -1.0 V the levels recover their relative position from before the addition of the gate electrode (Figure 7.7 non-connected levels at 0.0 V correspond to gate-free calculation). For negative potentials, a one-electron oxidation $\mathbf{2}^{+}$ is observed at -2.5 V, and the double oxidation to $\mathbf{2}^{2+}$ requires a potential of -6.0 V. These results are consistent with the experimental observation that **2** is isolated as a cation while **1** is neutral.

The value of the transmission at the Fermi level, T(0), gives an idea of the conductance of the molecule upon an applied bias potential. Figure 7.8 shows T(0) as a function of gate voltage for the two compounds and the typical *off-on-off-on* behavior expected as molecular levels cross the Fermi level. The *on* state corresponding to the δ* orbital is very sharp and narrow, reflecting the rather weak coupling of the level to the electrode, whereas the *on* state for the π* level is broader and more intense.

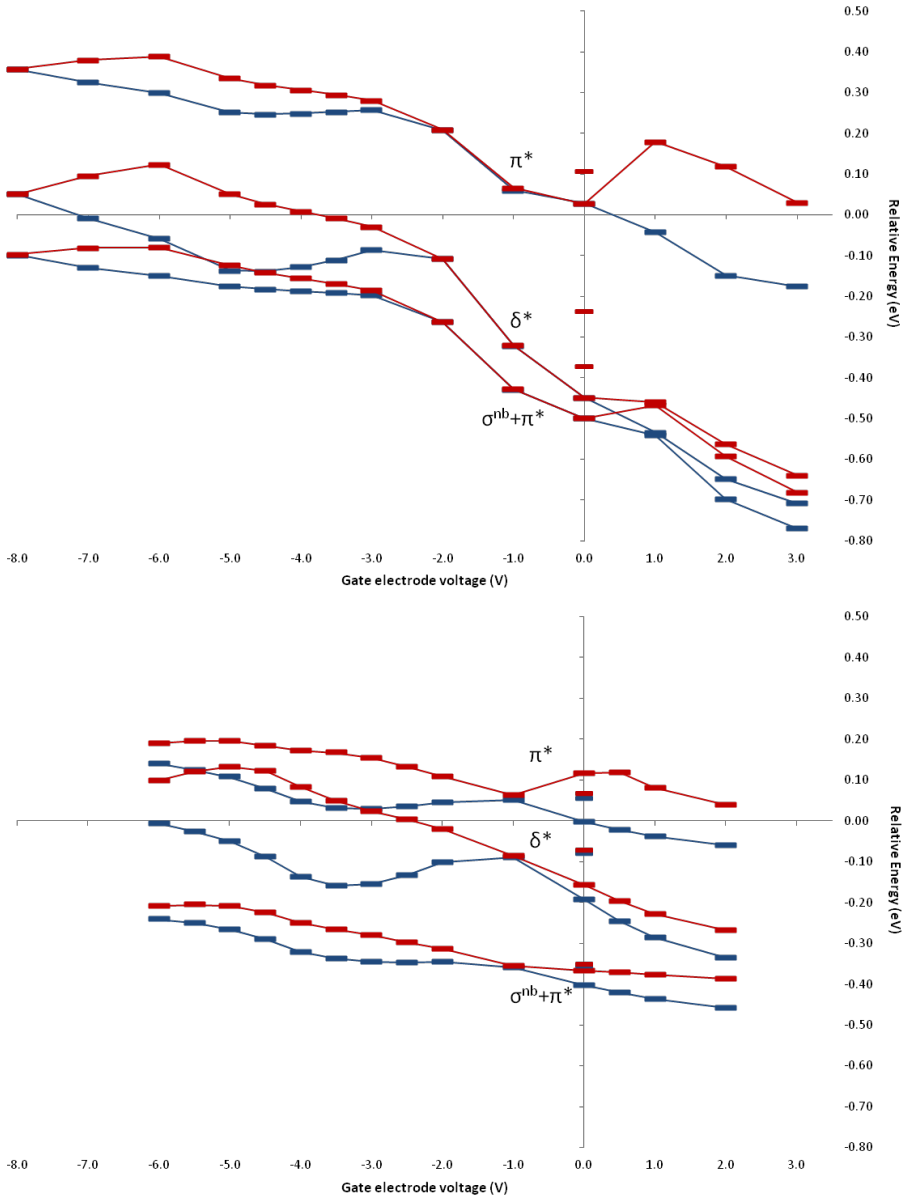

Figure 7.7. Eigenvalues of the molecular projected self-consistent Hamiltonian (MSPH) for **1** (top) and **2** (bottom) as a function of the gate electrode voltage (V). For every energy level spin-α (blue) and spin-β (red) are presented.

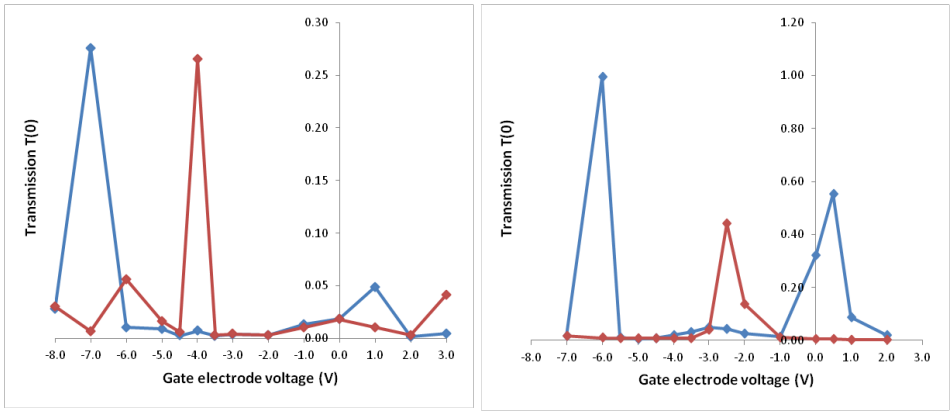

Figure 7.8. Transmission values at the Fermi level, T(0), for **1** (left) and **2** (right) as a function of the gate electrode voltage (V). Spin-α (blue) and spin-β (red) contributions are presented. Different vertical scales are used.

7.4 The counterion strategy

The solid-state gate used in the previous section clearly achieves the overall goal of destabilizing the molecular region, but does not accurately reflect the physical reality of the electrochemical gate, where the molecule is bathed in an electrolyte solution whose potential is controlled by the counter electrode. An alternative strategy to probe the transport properties of different redox states is to introduce an additional atom into the unit cell that will either extract or donate an electron from/to the molecule, forming either an cation or anion, respectively, in the process. We modeled these two situations for system **2** by introducing either a Na or a Cl atom into the unit cell, placed at a distance of 4 Å from the central Ru atom. The resulting transmission spectra for the two cases are shown in Figure 7.10, where they are compared to the corresponding traces for the solid state gate at +1.0 V and -4.0 V, respectively. The matching between the transmission spectra computed using the two different protocols is remarkable, with an almost one-to-one correspondence between the transport channels. We note, however, that if the counterion is moved further away from the molecule (6 or 8 Å), the gain in Coulomb attraction between the cation and anion is insufficient to drive the oxidation/reduction of the molecule, which remains neutral and diamagnetic. Thus the position of the counter ions in these calculations is critical.

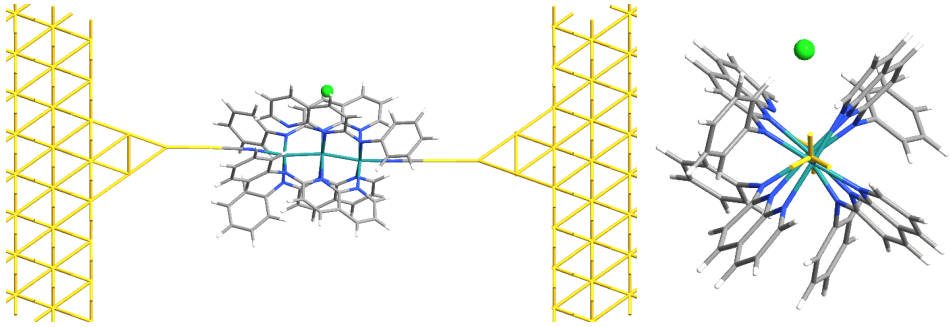

Figure 7.9. Device configuration with **2** and the heteroatom (X = Na, Cl) with views in front (left) and along the chain (right).

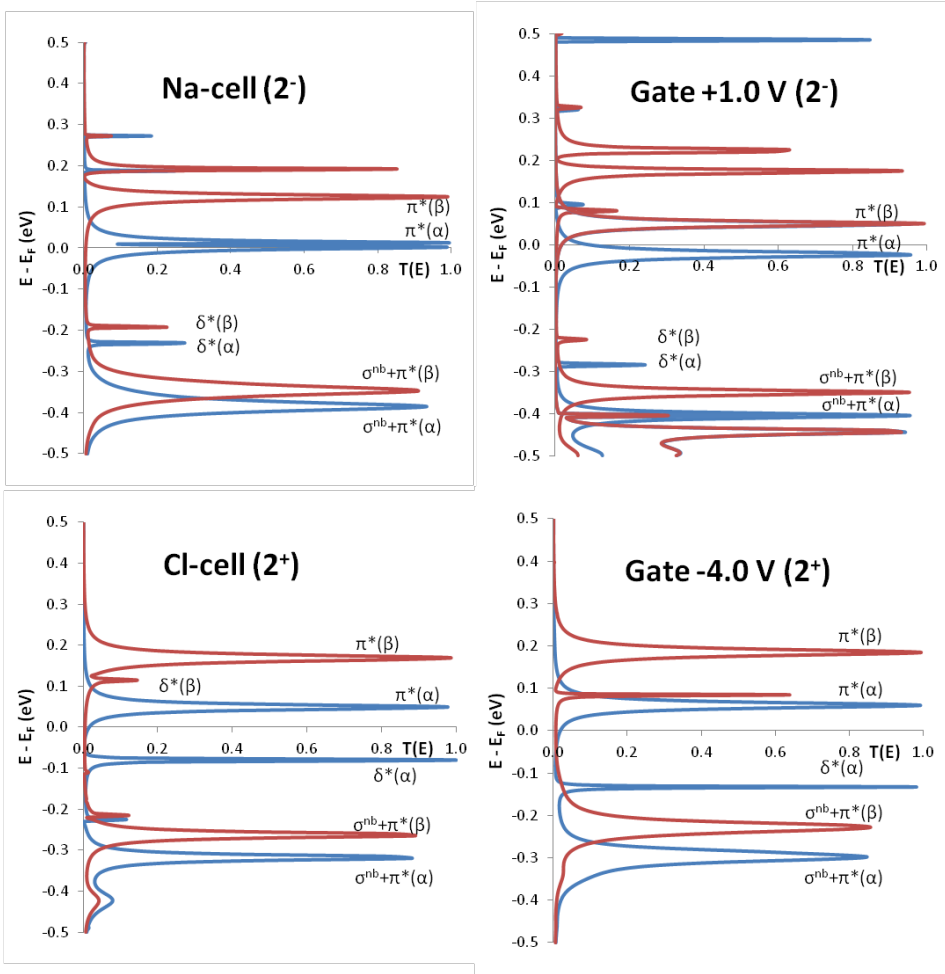

Figure 7.10. Comparison of the transmission spectra for system **2**. On top representing the $\mathbf{2}^{-}$ species, the Sodium–added cell (left) and the gate electrode +1.0 V (right). On bottom the $\mathbf{2}^{+}$ species, the Chlorine-added cell (left) and the gate electrode -4.0 V (right). Spin-α (blue) and spin-β (red) contributions are presented.

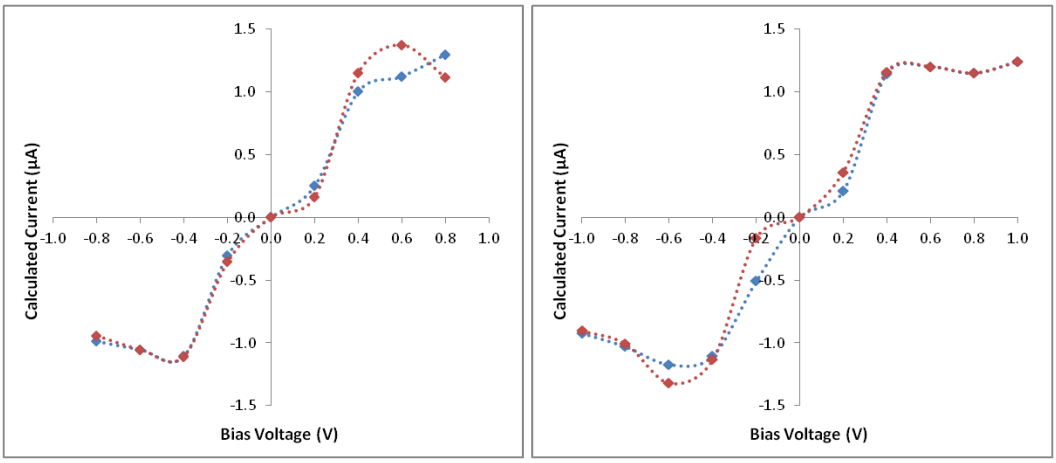

Figure 7.11. Calculated current (μA) as a function of applied bias voltage (V) for **2** (left) and **2*** (right). Spin-α (blue) and spin-β (red) contributions are presented.

7.5 About the npa asymmetry

In this section we investigate whether the asymmetry of the npa ligand affects the conductance properties of the ruthenium chain by comparing system **2** with a hypothetical isomer (**2***). This isomer differs in the orientation of the npa ligands in the molecule, which was imposed to be *symmetric* (2:2), instead of the original orientation of **2** (3:1).

We calculated the electric current through the neutral species at different source-drain bias voltage (Figure 7.11). The results for the two isomers are very similar, suggesting that the asymmetry of the npa ligand does not play a role on the electron transport properties. Moreover, we can see that both compounds present equal currents between positive and negative potential, which indicates no rectifying character.

7.6 Concluding remarks

In this chapter we presented two distinct strategies to model the effect of an electrochemical gate potential on the transport properties of EMACs. In the first one, a solid-state gate is included in the device region, while in the second one an additional atom capable of reducing or oxidizing the molecule is placed in the vicinity of the molecule. The results are broadly similar, with the gate potential driving the molecule through a series of oxidation states that are alternately diamagnetic and paramagnetic. The oxidation waves in both $Ru_3(dpa)_4(NCS)_2$ (**1**) and its naphthyridyl analogue, $Ru_3(npa)_4(NCS)_2$ (**2**) correspond to depopulation of the δ^* orbital while the reduction corresponds to population of the π^* channel. The results are in agreement with the redox properties of the compounds, that is, compound **2** is more easily oxidized than **1** as can be deduced from the lower gate potential required. Finally, we present results on the electron transport effects of the npa asymmetry, that indicate no rectifying character imposed to the molecule.

Chapter 8

Conclusions

The work of this thesis has focused on understanding the various properties of Extended Metal Atom Chains, with the goal of providing insight of the technological applicability of these systems in the field of electronics. For each property of interest, a different computational strategy was required and the advantages and difficulties of each method were discussed. The motivation to learn and apply several different methods (MCSCF/PT2, DFT, AIMD, NEGF) comes from the fact that no single available method can provide an accurate description for every scenario. This emphasizes the importance of the work of the computational scientist, to not accept any results as truth and to know the approximations each theory assumes and judge them accordingly. This is perhaps the most obvious conclusion of the work, one of the most important conclusions nonetheless.

Regarding the structural flexibility of chromium EMACs, we show that the metal chain can be easily affected by the axial ligand (X), in part due to the extremely flat Potential Energy Surface (PES). The multiconfigurational character of the electronic structure was confirmed and studied with a highly accurate methodology (CASSCF/CASPT2). The simulation of the PES show the difficulties DFT has to describe compounds with multiple unpaired electrons. The agreement of CASSCF/CASPT2 minima with the experimental characterization of CN and NO_3 structures serves to validate the method as it covers the whole range of symmetrical

to asymmetrical metal chains. The NCS case, the most promising from a technological point of view, appears in between the two previous cases, suggesting that a variety of structures could be observed when used in the device configuration and the real temperature conditions.

Despite the previous difficulties associated with DFT, we continued the study of the flexibility of the chromium EMACs by performing ab initio molecular dynamics on both the isolated molecule (gas) and the crystalline phase. DFT was able to differentiate between the axial ligands, in particular achieving the asymmetric structures in the NO_3 case. When analyzing the gas phase results, we showed the importance of the thermal energy in the distribution of the NCS and CN structures. In the crystalline phase, the packing effects and neighboring interactions appeared to be relevant in the NCS and CN cases. We discussed this interaction in terms of the bending of the axial ligand with respect to the chromium chain axis. However, these effects might not be present in the case of a device configuration, which resembles the gas phase and might force the axial ligand orientation with respect to the electrode surface. To sum up, the thermal effects must be taken into account when considering these flexible materials for applications in the field of electronics.

Metal-metal bonding is intrinsically related with the structural flexibility, and we extended the analysis to other Cr_2M systems in the EMACs family. We used the concept of Effective Bond Order (EBO) and the multiconfigurational wave function from CASSCF to quantify the bond multiplicity and the contributions from the different orbital symmetries (σ, δ and π). We showed that the EBO present a linear dependency on to the metal-metal distance, varying from 2.00 to 1.00, with the σ and π manifolds having the largest contributions. We have shown that even for medium distances (2.3 - 2.4 Å) the π bond contribution cannot be neglected, which questions the idea of the σ 3-center bond. In the case of $Cr_3(dpa)_4(X)_2$ structures, CN^- and NCS^- ligands favor delocalized molecular orbitals where the EBO reflects the global bonding of the Cr-Cr-Cr chain. We used localization techniques to quantify the contributions from each Cr-Cr pair in an attempt to prove that this methodology can be used to study larger systems containing 5 to 7 metals.

In chapter 6, we studied the magnetism of nickel compounds. Two different approaches for the calculation of the magnetic coupling constants (J) were described.

The first part discussed the problems of MC-PT2 with a minimal active space, and proposed a strategy to obtain DDCI-like molecular orbitals that improve the calculation of J-values. In the second part, we presented an efficient alternative to the conventional MC-PT2 methods, which can be used with large active spaces without substantial added computational cost. Multiconfigurational pair-density functional theory has shown good results in bond energies but had not been used for magnetism. In this work we showed MCPDFT can be applied to obtain CASPT2-like results with a fraction of the cost, and can be extended to systems with sizes that CASPT2 cannot handle.

Finally, we had the opportunity to perform electron transport calculations in ruthenium EMACs. We proposed two distinct strategies to model the effect of an electrochemical gate potential and showed the agreement between the two. Whereas the addition of a heteroatom generates an ionic contact species, the use of a solid gate electrode allows driving the molecule through a series of oxidation states that are alternately diamagnetic and paramagnetic. We identify the channels responsible for the conduction of both $Ru_3(dpa)_4(NCS)_2$ (**1**) and its naphthyridyl analogue, $Ru_3(npa)_4(NCS)_2$ (**2**) and the results are in agreement with the redox properties of the compounds.

Chapter 9

Publications

Improving the calculation of magnetic coupling constants in MRPT methods, M. Spivak, C. Angeli, C. J. Calzado and C. de Graaf, Journal of Computational Chemistry, **35**, 1665-1671 (2014).

Structure and bonding in trimetallic arrays containing a Cr-Cr quadruple bond: A challenge to density functional theory, V. Arcisauskaite, M. Spivak and J. E. McGrady, Inorganica Chimica Acta, **424**, 293-299 (2015).

Biradical character in the ground state of $[Mn@Si_{12}]^+$: a DFT and CASPT2 study, V. Arcisauskaite, D. Fijan, M. Spivak, C. de Graaf and J. E. McGrady, Physical Chemistry Chemical Physics, **18**, 24006-24014 (2016).

Quantum chemical characterization of single molecule magnets based on uranium, M. Spivak, K. Vogiatzis, C. Cramer, C. de Graaf and L. Gagliardi, The Journal of Physical Chemistry A (Submitted 31/10/2016).

A Multiconfigurational Approach to the Electronic Structure of Trichromium Extended Metal Atom Chains, M. Spivak, V. Arcisauskaite, X. López, J. E. McGrady and C. de Graaf, in preparation.

Ab initio Molecular Dynamics on the backbone flexibility of chromium Extended Metal Atom Chains, M. Spivak, V. Arcisauskaite, X. López, J. E. McGrady and C. de Graaf, in preparation.

Metal-Metal bonding in Cr_2M Extended Metal Atom Chains, M. Spivak, V. Arcisauskaite, X. López, J. E. McGrady and C. de Graaf, in preparation.

Magnetism on Extended Metal Chains: Multiconfigurational pair-density functional theory., M. Spivak, C. de Graaf and L. Gagliardi, in preparation.

Gating the Conductance of Extended Metal Atom Chains: a computational analysis, M. Spivak, V. Arcisauskaite, C. de Graaf, J. E. McGrady, in preparation.

Chapter 10

References

[1] R. Chau, B. Doyle, S. Datta, J. Kavalieros, and K. Zhang, Nat. Mater. **6**, 810 (2007).

[2] W. Y. Kim and K. S. Kim, Accounts of Chemical Research **43**, 111 (2010).

[3] J. Camarero and E. Coronado, J. Mater. Chem. **19**, 1678 (2009).

[4] K.-N. Shih, M.-J. Huang, H.-C. Lu, M.-D. Fu, C.-K. Kuo, G.-C. Huang, G.-H. Lee, C.-h. Chen, and S.-M. Peng, Chem. Commun. **46**, 1338 (2010).

[5] V. P. Georgiev, P. Mohan, D. DeBrincat, and J. E. McGrady, Coordination Chemistry Reviews **257**, 290 (2013).

[6] V. P. Georgiev and J. E. McGrady, Journal of the American Chemical Society **133**, 12590 (2011).

[7] R. Clérac, F. A. Cotton, L. M. Daniels, K. R. Dunbar, K. Kirschbaum, C. A. Murillo, A. A. Pinkerton, A. J. Schultz, and X. Wang, Journal of the American Chemical Society **122**, 6226 (2000).

[8] D. A. Pantazis and J. E. McGrady, Journal of the American Chemical Society **128**, 4128 (2006).

[9] M.-M. Rohmer, A. Strich, M. Bénard, and J.-P. Malrieu, Journal of the American Chemical Society **123**, 9126 (2001).

[10] F. A. Cotton, L. M. Daniels, C. A. Murillo, and I. Pascual, Journal of the American Chemical Society **119**, 10223 (1997).

[11] B. O. Roos, P. R. Taylor, and P. E. M. Siegbahn, Chemical Physics **48**, 157 (1980).

[12] P. A. Malmqvist, A. Rendell, and B. O. Roos, The Journal of Physical Chemistry **94**, 5477 (1990).

[13] T. Fleig, J. Olsen, and L. Visscher, The Journal of Chemical Physics **119**, 2963 (2003).

[14] D. Ma, G. Li Manni, and L. Gagliardi, The Journal of Chemical Physics **135**, 044128 (2011).

[15] D. K. W. Mok, R. Neumann, and N. C. Handy, The Journal of Physical Chemistry **100**, 6225 (1996).

[16] J. W. Hollett and P. M. W. Gill, The Journal of Chemical Physics **134**, 114111 (2011).

[17] N. C. Handy and A. J. Cohen, Molecular Physics **99**, 403 (2001).

[18] K. Andersson, P. A. Malmqvist, B. O. Roos, A. J. Sadlej, and K. Wolinski, The Journal of Physical Chemistry **94**, 5483 (1990).

[19] K. Andersson, P. A. Malmqvist, and B. O. Roos, The Journal of Chemical Physics **96**, 1218 (1992).

[20] P. A. Malmqvist, K. Pierloot, A. R. M. Shahi, C. J. Cramer, and L. Gagliardi, The Journal of Chemical Physics **128**, 204109 (2008).

[21] D. Ma, G. Li Manni, J. Olsen, and L. Gagliardi, Journal of Chemical Theory and Computation **12**, 3208 (2016).

[22] P. A. M. Dirac, Mathematical Proceedings of the Cambridge Philosophical Society **26**, 376385 (1930).

[23] S. H. Vosko, L. Wilk, and M. Nusair, Canadian Journal of Physics **58**, 1200 (1980).

[24] A. D. Becke, Phys. Rev. A **38**, 3098 (1988).

[25] J. P. Perdew, K. Burke, and M. Ernzerhof, Phys. Rev. Lett. **77**, 3865 (1996).

[26] C. Lee, W. Yang, and R. G. Parr, Phys. Rev. B **37**, 785 (1988).

[27] J. P. Perdew, Phys. Rev. B **33**, 8822 (1986).

[28] Y. Zhao and D. G. Truhlar, The Journal of Chemical Physics **125**, 194101 (2006).

[29] A. D. Becke, The Journal of Chemical Physics **98**, 5648 (1993).

[30] M. Brandbyge, J.-L. Mozos, P. Ordejón, J. Taylor, and K. Stokbro, Phys. Rev. B **65**, 165401 (2002).

[31] M. J. Frisch, G. W. Trucks, H. B. Schlegel, G. E. Scuseria, M. A. Robb, J. R. Cheeseman, G. Scalmani, V. Barone, B. Mennucci, G. A. Petersson, et al., Gaussian 09 Revision D.01, Gaussian Inc., Wallingford CT (2013).

[32] A. D. Becke, The Journal of Chemical Physics **104**, 1040 (1996).

[33] F. Weigend and R. Ahlrichs, Phys. Chem. Chem. Phys. **7**, 3297 (2005).

[34] J. P. Malrieu, R. Caballol, C. J. Calzado, C. de Graaf, and N. Guihry, Chemical Reviews **114**, 429 (2014).

[35] F. Aquilante, L. De Vico, N. Ferré, G. Ghigo, P.-Å. Malmqvist, P. Neograd y, T. B. Pedersen, M. Pitoňák, M. Reiher, B. O. Roos, et al., J. Comput. Chem. **31**, 224 (2010).

[36] O. B. Roos, V. Veryazov, and P.-O. Widmark, Theoretical Chemistry Accounts **111**, 345 (2003).

[37] F. Aquilante, P.-k. Malmqvist, T. B. Pedersen, A. Ghosh, and B. O. Roos, Journal of Chemical Theory and Computation **4**, 694 (2008).

[38] Golden Software, LLC. 809 14th Street Golden, Colorado 80401 www.goldensoftware.com.

[39] J. F. Berry, F. A. Cotton, T. Lu, C. A. Murillo, B. K. Roberts, and X. Wang, Journal of the American Chemical Society **126**, 7082 (2004).

[40] C. Bloch, Nuclear Physics **6**, 329 (1958).

[41] J. des Cloizeaux, Nuclear Physics **20**, 321 (1960).

[42] CPMD, http://www.cpmd.org/, Copyright IBM Corp 1990-2008, Copyright MPI für Festkörperforschung Stuttgart 1997-2001.

[43] G. Kresse and J. Hafner, Phys. Rev. B **47**, 558 (1993).

[44] G. Kresse and J. Hafner, Phys. Rev. B **49**, 14251 (1994).

[45] G. Kresse and J. Furthmüller, Phys. Rev. B **54**, 11169 (1996).

[46] G. Kresse and J. Furthmller, Computational Materials Science **6**, 15 (1996).

[47] G. Kresse and J. Hafner, Journal of Physics: Condensed Matter **6**, 8245 (1994).

[48] G. Kresse and D. Joubert, Phys. Rev. B **59**, 1758 (1999).

[49] G. Li Manni, D. Ma, F. Aquilante, J. Olsen, and L. Gagliardi, Journal of Chemical Theory and Computation **9**, 3375 (2013).

[50] L. Veis, A. Antalík, J. Brabec, F. Neese, O. Legeza, and J. Pittner, The Journal of Physical Chemistry Letters **7**, 4072 (2016).

[51] S. Vancoillie, P. A. Malmqvist, and V. Veryazov, Journal of Chemical Theory and Computation **12**, 1647 (2016).

[52] D. Ma, G. Li Manni, J. Olsen, and L. Gagliardi, Journal of Chemical Theory and Computation **12**, 3208 (2016).

[53] F. A. Cotton, S. A. Koch, and M. Millar, Inorganic Chemistry **17**, 2084 (1978).

[54] C. M. F.A. Cotton and R. Walton, Muliple bonds between metal atoms (Springer, New York, 2005).

[55] M. Brynda, L. Gagliardi, P.-O. Widmark, P. P. Power, and B. O. Roos, Angewandte Chemie **118**, 3888 (2006).

[56] M. Brynda, L. Gagliardi, and B. O. Roos, Chemical Physics Letters **471**, 1 (2009).

[57] D. W. Brogden, Y. Turov, M. Nippe, G. Li Manni, E. A. Hillard, R. Clérac, L. Gagliardi, and J. F. Berry, Inorganic Chemistry **53**, 4777 (2014).

[58] R. A. Kok and M. B. Hall, Journal of the American Chemical Society **105**, 676 (1983).

[59] R. A. Kok and M. B. Hall, Inorganic Chemistry **24**, 1542 (1985).

[60] R. D. Davy and M. B. Hall, Journal of the American Chemical Society **111**, 1268 (1989).

[61] S. Ndambuki and T. Ziegler, Inorganic Chemistry **52**, 3860 (2013).

[62] F. A. Cotton, L. M. Daniels, C. A. Murillo, I. Pascual, and H.-C. Zhou, Journal of the American Chemical Society **121**, 6856 (1999).

[63] M. Nippe, J. Wang, E. Bill, H. Hope, N. S. Dalal, and J. F. Berry, Journal of the American Chemical Society **132**, 14261 (2010).

[64] M. Nippe and J. F. Berry, Journal of the American Chemical Society **129**, 12684 (2007).

[65] M. Nippe, E. Bill, and J. F. Berry, Inorganic Chemistry **50**, 7650 (2011).

[66] F. Aquilante, J. Autschbach, R. K. Carlson, L. F. Chibotaru, M. G. Delcey, L. De Vico, I. Fdez. Galvn, N. Ferr, L. M. Frutos, L. Gagliardi, et al., Journal of Computational Chemistry **37**, 506 (2016).

[67] E.J. Baerends, T. Ziegler, J. Autschbach, D. Bashford, A. Bérces, F.M. Bickelhaupt, C. Bo, P.M. Boerrigter, L. Cavallo, D.P. Chong, L. Deng, R.M. Dickson, D.E. Ellis, M. van Faassen, L. Fan, T.H. Fischer, C. Fonseca Guerra, M. Franchini, A. Ghysels, A. Giammona, S.J.A. van Gisbergen, A.W. Götz, J.A. Groeneveld, O.V. Gritsenko, M. Grüning, S. Gusarov, F.E. Harris, P. van den Hoek, C.R. Jacob, H. Jacobsen, L. Jensen, J.W. Kaminski, G. van Kessel, F. Kootstra, A. Kovalenko, M.V. Krykunov, E. van Lenthe, D.A. McCormack, A. Michalak, M. Mitoraj, S.M. Morton, J. Neugebauer, V.P. Nicu, L. Noodleman, V.P. Osinga, S. Patchkovskii, M. Pavanello, P.H.T. Philipsen, D. Post, C.C. Pye, W. Ravenek, J.I. Rodrguez, P. Ros, P.R.T. Schipper, H. van Schoot, G. Schreckenbach, J.S. Seldenthuis, M. Seth, J.G. Snijders, M. Solá, M. Swart, D. Swerhone, G. te Velde, P. Vernooijs, L. Versluis, L. Visscher, O. Visser, F. Wang, T.A. Wesolowski, E.M. van Wezenbeek, G. Wiesenekker, S.K. Wolff, T.K. Woo, A.L. Yakovlev, ADF2014, SCM, Theoretical Chemistry, Vrije Universiteit, Amsterdam, The Netherlands, http://www.scm.com.

[68] G. te Velde, F. M. Bickelhaupt, E. J. Baerends, C. Fonseca Guerra, S. J. A. van Gisbergen, J. G. Snijders, and T. Ziegler, Journal of Computational Chemistry **22**, 931 (2001).

[69] C. Fonseca Guerra, J. G. Snijders, G. te Velde, and E. J. Baerends, Theoretical Chemistry Accounts **99**, 391 (1998).

[70] J. Miralles, J.-P. Daudey, and R. Caballol, Chem. Phys. Lett. **198**, 555 (1992).

[71] J. Miralles, O. Castell, R. Caballol, and J.-P. Malrieu, Chem. Phys. **172**, 33 (1993).

[72] C. J. Calzado, Chem. Eur. J. **19**, 1254 (2012).

[73] C. J. Calzado, J. Cabrero, J.-P. Malrieu, and R. Caballol, J. Chem. Phys. **116**, 2728 (2002).

[74] C. J. Calzado, C. Angeli, D. Taratiel, R. Caballol, and J.-P. Malrieu, J. Chem. Phys. **131**, 044327 (2009).

[75] J.-P. Malrieu, R. Caballol, C. J. Calzado, C. de Graaf, and N. Guihéry, Chem. Rev. **114**, 429 (2014).

[76] C. J. Calzado, J.-P. Malrieu, J. Cabrero, and R. Caballol, J. Phys. Chem. A **104**, 11636 (2000).

[77] F. Neese, J. Chem. Phys. **119**, 9428 (2003).

[78] C. J. Calzado, S. Evangelisti, and D. Maynau, J. Phys. Chem. A **107**, 7581 (2003).

[79] E. Bordas, R. Caballol, C. de Graaf, and J.-P. Malrieu, Chem. Phys. **309**, 259 (2005).

[80] B. Bories, D. Maynau, and M.-L. Bonnet, J. Comput. Chem. **28**, 632 (2007).

[81] V. Barone, I. Cacelli, A. Ferretti, S. Monti, and G. Prampolini, J. Chem. Theory Comput. **7**, 699 (2011).

[82] C. de Graaf, C. Sousa, I. de P. R. Moreira, and F. Illas, J. Phys. Chem. A **105**, 11371 (2001).

[83] N. Queralt, D. Taratiel, C. de Graaf, R. Caballol, R. Cimiraglia, and C. Angeli, J. Comput. Chem. **29**, 994 (2008).

[84] C. Angeli and C. J. Calzado, J. Chem. Phys. **137**, 034104 (2012).

[85] J. Cabrero, C. J. Calzado, D. Maynau, R. Caballol, and J.-P. Malrieu, J. Phys. Chem. A **106**, 8146 (2002).

[86] N. Suaud, R. Ruamps, N. Guihéry, and J.-P. Malrieu, Journal of Chemical Theory and Computation **8**, 4127 (2012).

[87] Z. Tabookht, X. López, and C. de Graaf, The Journal of Physical Chemistry A **114**, 2028 (2010).

[88] R. Boča, Theoretical Foundations of Molecular Magnetism (Elsevier, Amsterdam, 1999).

[89] R. Bastardis, N. Guihéry, and C. de Graaf, Phys. Rev. B **76**, 132412 (2007).

[90] A. Bencini and F. Totti, Inorg. Chim. Acta **361**, 4153 (2008).

[91] CASDI package developed at the Laboratoire de Physique Quantique, Université Paul Sabatier, Toulouse, France.

[92] N. Ben Amor and D. Maynau, Chem. Phys. Lett. **286**, 211 (1998).

[93] R. Cimiraglia, C. Angeli, NEVPT2 package, Dipartimento di Chimica, Università di Ferrara, Ferrara, Italy, 2002-2012.

[94] G. Li Manni, R. K. Carlson, S. Luo, D. Ma, J. Olsen, D. G. Truhlar, and L. Gagliardi, Journal of Chemical Theory and Computation **10**, 3669 (2014).

[95] R. K. Carlson, G. L. Manni, A. L. Sonnenberger, D. G. Truhlar, and L. Gagliardi, Journal of Chemical Theory and Computation **11**, 82 (2015).

[96] J. Miralles, R. Caballol, and J.-P. Malrieu, Chem. Phys. **153**, 25 (1991).

[97] The dedicated orbitals where obtained by diagonalizing the density matrix obtained by subtracting the CAS+S density matrices of the triplet and quintet states. All virtual orbital with participation number smaller than $2.50\text{x}10^{-3}$ were eliminated from the MO space used to construct the DDCI space.

[98] V. M. García, O. Castell, R. Caballol, and J.-P. Malrieu, Chem. Phys. Lett. **238**, 222 (1995).

[99] K. Andersson, P.-Å. Malmqvist, and B. O. Roos, J. Chem. Phys. **96**, 1218 (1992).

[100] G. Ghigo, B. O. Roos, and P.-Å. Malmqvist, Chem. Phys. Lett. **396**, 142 (2004).

[101] C. Angeli, R. Cimiraglia, S. Evangelisti, T. Leininger, and J.-P. Malrieu, J. Chem. Phys. **114**, 10252 (2001).

[102] C. Angeli, R. Cimiraglia, and J.-P. Malrieu, Chem. Phys. Lett. **350**, 297 (2001).

[103] C. Angeli, R. Cimiraglia, and J.-P. Malrieu, J. Chem. Phys. **117**, 9138 (2002).

[104] C. Angeli, M. Pastore, and R. Cimiraglia, Theor. Chem. Acc. **117**, 743 (2007).

[105] K. G. Dyall, J. Chem. Phys. **102**, 4909 (1995).

[106] D. Taratiel, J. Cabrero, C. de Graaf, and R. Caballol, Polyhedron **22**, 2409 (2003).

[107] E. Bordas, R. Caballol, and C. de Graaf, J. Mol. Struct. (TheoChem) **727**, 173 (2005).

[108] A. Escuer, R. Vicente, M. S. El Falah, X. Solans, and M. Font-Bardia, Inorg. Chim. Acta **43**, 43 (1998).

[109] J. Ribas, M. Monfort, C. Diaz, C. Bastos, and X. Solans, Inorg. Chem. **32**, 3557 (1993).

[110] R. Bastardis, N. Guihéry, and C. de Graaf, J. Chem. Phys. **129**, 104102 (2008).

[111] P. Romn, C. Guzmn-Miralles, A. Luque, J. I. Beitia, J. Cano, F. Lloret, M. Julve, and S. Alvarez, Inorg. Chem. **35**, 3741 (1996).

[112] T. Wen, L. K. Thompson, F. L. Lee, and E. J. Gabe, Inorg. Chem. **27**, 4190 (1988).

[113] L. Rosemberg, T. L. K., E. J. Gabe, and F. L. Lee, J. Chem. Soc. Dalton Trans. **3**, 625 (1986).

[114] P. Mukherjee, M. G. B. Drew, C. J. Gomez-Garcia, and A. Ghosh, Inorg. Chem. **48**, 5848 (2009).

[115] I. de P. R. Moreira, N. Suaud, N. Guihéry, J.-P. Malrieu, R. Caballol, J. M. Bofill, and F. Illas, Phys. Rev. B **66**, 134430 (2002).

[116] I. Negodaev, C. de Graaf, and R. Caballol, Chem. Phys. Lett. **458**, 290 (2008).

[117] B. Wang and Z. Chen, Chem. Phys. Lett. **387**, 395 (2004).

[118] S.-Y. Lin, I.-W. P. Chen, C.-h. Chen, M.-H. Hsieh, C.-Y. Yeh, T.-W. Lin, Y.-H. Chen, and S.-M. Peng, The Journal of Physical Chemistry B **108**, 959 (2004).

[119] S.-M. Peng, C.-C. Wang, Y.-L. Jang, Y.-H. Chen, F.-Y. Li, C.-Y. Mou, and M.-K. Leung, Journal of Magnetism and Magnetic Materials **209**, 80 (2000).

[120] V. N. Staroverov and E. R. Davidson, International Journal of Quantum Chemistry **77**, 651 (2000).

[121] F. Moscardó and E. San-Fabián, Phys. Rev. A **44**, 1549 (1991).

[122] B. B. MIEHLICH, H. STOLL, and A. SAVIN, Molecular Physics **91**, 527 (1997).

[123] J. J. W. McDOUALL, Molecular Physics **101**, 361 (2003).

[124] Z. Tabookht, X. López, M. Bénard, and C. de Graaf, The Journal of Physical Chemistry A **114**, 12291 (2010).

[125] R. Clérac, F. A. Cotton, K. R. Dunbar, C. A. Murillo, I. Pascual, and X. Wang, Inorganic Chemistry **38**, 2655 (1999).

[126] T.-W. Tsai, Q.-R. Huang, S.-M. Peng, and B.-Y. Jin, The Journal of Physical Chemistry C **114**, 3641 (2010).

[127] C.-S. Tsai, I. P.-C. Liu, F.-W. Tien, G.-H. Lee, C.-Y. Yeh, C. hsien Chen, and S.-M. Peng, Inorganic Chemistry Communications **38**, 152 (2013).

[128] P. J. Mohan, V. P. Georgiev, and J. E. McGrady, Chem. Sci. **3**, 1319 (2012).

[129] J. P. Perdew, K. Burke, and M. Ernzerhof, Physical Review Letters **77**, 3865 (1996).

[130] E. van Lenthe, A. Ehlers, and E.-J. Baerends, The Journal of Chemical Physics **110** (1999).

[131] http://www.quantumwise.com.

[132] J. Taylor, H. Guo, and J. Wang, Phys. Rev. B **63**, 245407 (2001).

[133] J. M. Soler, E. Artacho, J. D. Gale, A. Garca, J. Junquera, P. Ordejn, and D. Snchez-Portal, Journal of Physics: Condensed Matter **14**, 2745 (2002).

[134] H. H. B. Sørensen, P. C. Hansen, D. E. Petersen, S. Skelboe, and K. Stokbro, Phys. Rev. B **77**, 155301 (2008).

[135] S. Datta, Electron Transport in Mesoscopic Systems (Cambridge University Press, Cambridge, UK, 1997).

[136] S. Datta, Quantum Transport: Atom to Transistor (Cambridge University Press, Cambridge, UK, 2005).

[137] A. N. J. Jortner and M. A. Ratner, Introducing Molecular Electronics (Springer, New York, 2005).

[138] S. Lindsay, Faraday Discuss. **131**, 403 (2006).

[139] J. P. Perdew and A. Zunger, Phys. Rev. B **23**, 5048 (1981).

[140] N. Troullier and J. L. Martins, Phys. Rev. B **43**, 1993 (1991).

[141] H. J. Monkhorst and J. D. Pack, Phys. Rev. B **13**, 5188 (1976).